ENGINEERING DRUIEG DELIVERY PLATFORMS FOR CANCER AND INFECTIOUS DISEASES

A Dissertation

by

SHREEDEVI ARUN KUMAR

Submitted to the Graduate and Professional School of
Texas A&M University
in partial fulfillment of the requirements for the degree of

DOCTOR OF PHILOSOPHY

Chair of Committee,	Akhilesh K. Gaharwar
Committee Members,	Daniel L. Alge
	Abhishek Jain
	Srinath Palakurthi
Head of Department,	Michael J. McShane

August 2021

Major Subject: Biomedical Engineering

ABSTRACT

Vaccines and chemotherapeutic agents have been developed to treat infectious diseases and cancer, respectively. However, efficacy of the therapeutic agents used to treat these diseases can be significantly improved through the use of drug delivery platforms. Although, polymer-based drug delivery platforms have been developed, owing to technical challenges, these platforms often do not get clinically translated. In this dissertation, three polymer-based platforms were engineered: 1) injectable polyester-based platform for on-demand therapeutic delivery, 2) molybdenum disulfide (MoS_2)-incorporated polyacrylonitrile (PAN) nanofibers with improved cytocompatibility, and 3) doxorubicin (DOX)/ polyvinyl alcohol (PVA)-loaded shape memory polymer (SMP) foams for increased drug loading.

Firstly, single injection vaccines (SIV) platforms provide exciting opportunities for efficient vaccine delivery. However, current platforms do not cater cargo versatility or delayed burst release kinetics that is crucial for optimal immune response. Thus, an injectable polyester-based platform called “polybubbles” was developed to maintain functionality of therapeutic agents housed within while enabling delayed burst release of cargo. This platform also enables on-demand delivery capabilities upon extracorporeal activation through the incorporation of near-infrared (NIR)-sensitive gold nanorods (AuNRs).

Secondly, PAN nanofibers can be used as bioscaffolds to enable effective chemotherapy release. However, cytocompatibility of the PAN nanofibers would have to be improved for clinical translation. Thus, defect-rich MoS_2 nanoassemblies were incorporated into PAN nanofibers through electrospinning. Ideal defect morphology was identified and was successfully used to improve mechanical properties and hydrophilicity of PAN nanofibers. Increased cell adhesion and viability was observed with the incorporation of defect-rich MoS_2 indicating improved cytocompatibility. These hybrid nanofiber scaffolds thus show potential for downstream biomedical applications including drug delivery.

Lastly, SMP foams can be used as a small molecule carrier, specifically for anti-cancer applications. DOX-loaded SMP foams can thus potentially be used as an adjuvant to breast cancer tumor resection while precise sealing of the post-surgical void. DOX loading onto the SMP foams was improved successfully using viscosity modulating agent called PVA. This modified drug formulation did not have significant impact on the properties of SMP or DOX functionality *in vitro*. Study of these three platforms thus establish the clinical potential of polymer-based materials in improving therapeutic efficacy.

DEDICATION

This dissertation is dedicated to my undergraduate advisor for seeding my interest in academic research, my graduate advisors for encouraging me to work towards my passion, and my parents for their unconditional love and support.

ACKNOWLEDGEMENTS

I sincerely would like to thank everyone who provided me with professional and personal guidance since Fall 2016. Without the continuous support from my peers, mentors, friends, and family, I would not have been able to complete this dissertation.

I would like to first sincerely thank my committee chair, Dr. Akhilesh Gaharwar. His thoughtful guidance, constant encouragement, and mentorship steered me towards successfully accomplishing my research goals. He genuinely helped me transition into his lab during a time of uncertainty and ensured a smooth transition. I am very grateful for the opportunities he provided me with in the last two years. I would also like to thank my earlier committee chair, Dr. Corey Bishop, for his excellent mentorship. My interest in drug deliver was deepened after starting my Ph.D. in his lab. I am grateful for his guidance and thoughtfulness in integrating my research interests into the overall lab goals. I am glad to have worked with such a passionate researcher who truly cares about the mission of each project he undertakes.

I would like to specially thank Dr. Daniel Alge for being a caring mentor throughout my Ph.D. and being an inspiration for my teaching interests. He goes out of his way to help students like me and provides invaluable guidance during difficult times. I would also like to acknowledge Dr. Duncan Maitland for his care and help with continuing our collaboration even after my transition to a new lab. I would also like to thank other committee members Dr. Abhishek Jain and Dr. Srinath Palakurthi for their time and feedback throughout the course of this research.

I am grateful for all my co-workers in the department for guiding me through my professional and personal goals: Yong-Yu Jhan, Tanmay Mathur, Biswadeep Nayak, Kaivalya Deo, Navaneeth Krishna Pandian, Kanwar Abhay Singh, Giriraj Lokhande, Aparna Murali, Anna Brokesh, Anna Kersey, Patrick Lee, Grace Fletcher. I would also like to acknowledge help from my undergraduates: David Hendrix, Jacob Good, Whitney Souery, Daniel Prasca-Chamorro, Guillermo Zuniga, and David Mitchell Moore.

I would also like to recognize my friends, Pratima Purohit and Varsha Venkatraj who have been my support system here in College Station. Special thanks to Kinnari Modi and Bismayan Chakrabarti for providing me emotional support for the past decade. I would also like to thank my friend, Maheshwaran Umapathy, for his constant encouragement and motivation. I am unable to recognize everyone I interacted with in the last 5 years but would like to thank all of them for their friendship. My interest in research was seeded by Anderson lab during my undergraduate studies. I am forever grateful for my undergraduate research experience and would like to thank Dr. Stephen Anderson, Dr. Elliot Campbell, Daya Patel, Lynda Tuberty, and Yiwen Chang.

Finally, thanks to my mother, Jayashree Arunkumar, and father, Arunkumar Devarajan, for their constant encouragement, love, and support. They were a constant source of encouragement through my highs and lows throughout my life especially during my Ph.D. They motivated me to pursue my dreams and without them I would not have been able to complete my Ph.D. I am extremely grateful for their sacrifices and for teaching me to bounce back stronger after every challenge. I thank them for always reminding me about the big picture when I am at my lowest and for trusting my decisions. I am grateful to have such wonderful parents who are also my first mentors.

CONTRIBUTORS AND FUNDING SOURCES

Contributors

This work was supervised by a thesis committee consisting of Dr. Akhilesh K. Gaharwar (Advisor), Dr. Corey J. Bishop, Dr. Daniel L. Alge, Dr. Duncan J. Maitland, and Dr. Abhishek Jain of the Department of Biomedical Engineering, and Dr. Srinath Palakurthi of the Department of Pharmaceutical Sciences.

The data analyzed for Chapter 2 was conducted in part by Jihui Lee, as we share co-first authorship in the paper that was published in 2018. The data in Chapter 2 (2.1.2, 2.1.3, 2.2.4, 2.3.2) was provided by Dr. Bryan E. Tomlin affiliated with the elemental analysis lab within the department of chemistry at TAMU who assisted with the neutron activation analysis (NAA). Release study data in Chapter 3 was in part conducted with the help of my undergraduate students Jacob Good and David Hendrix. *In vivo* data in Chapter 3 was collected with the help of Dr. Eunsoo Yoo from Dr. Dongin Kim's lab. Data analyzed for Chapter 4 was conducted in part by Dr. Bhuvaneshwari Balasubramaniam, Kanwar Abhay Singh, and Dr. Sukanya Bhunia as we share authorship in the paper that will be submitted for publication in 2021. Data in Chapter 5 (5.2.2) was provided by Grace Fletcher, graduate student in Dr. Duncan J. Maitland's lab within the department of biomedical engineering at TAMU. All other work conducted for the dissertation was completed by the student independently under the guidance of Dr. Akhilesh K. Gaharwar, Dr. Corey J. Bishop, and Dr. Duncan J. Maitland.

Funding Sources

Graduate study was supported by graduate assistantship from the Department of Biomedical Engineering at Texas A&M University, U.S. Senator Phil Gramm Doctoral Fellowship and a Dissertation Fellowship from Office of Graduate and Professional Studies. This work was also made possible in part by Department of Biomedical Engineering at Texas A&M University under Start Up Laboratory funding. Its contents are solely the responsibility of the authors and do not necessarily represent the official views of the Department of Biomedical Engineering.

NOMENCLATURE

AAC	Amino-acid based Cargo
Acri	Acriflavine
AuNR	Gold nanoparticles
AuNR	Gold nanorods
BET	Brunauer-Emmett-Teller
BJH	Barrett-Joyner-Halenda
BSA	Bovine Serum Albumin
CMC	Carboxymethyl Cellulose
CTAB	Cetrimonium bromide
CV	Cyclic voltammetry
DALYs	Disability-adjusted Life Year
DMEM HG	Dulbecco’s Modified Eagle Medium High Glucose
DMSO	Dimethyl Sulfoxide
DOX	Doxorubicin
DRIE	Deep-reactive ion etching
DS	Dermatan sulfate
DSC	Differential Scanning Calorimetry
DXM	Dexamethasone
EIS	Electrochemical impedance spectroscopy
ELISA	Enzyme-linked Immunosorbent Assay
FDA	Food and drug administration
FDM	Fused deposition modeling
HA	Hyaluronic Acid
HDI	Hexamethylene diisocyanate
HEMA	Hydroxyethyl methacrylate
HIV	Human Immunodeficiency Virus
HME	Hot melt extrusion
hMSCs	Human Mesenchymal Cells
MCF-7	A cell line of human breast cancer
MoS_2	Molybdenum Disulfide
MPs	Microparticles
NIR	Near-infrared
PAN	Polyacryonitrile
PBS	Phosphate Buffer Saline
PCL	Polycaprolactone
PCLTA	Polycaprolactone riacrylate
PDMS	Polydimethylsiloxane
PEGDA	Polyethylene glycol diacrylate
PLGA	Poly (lactic-co-glycolic acid)
PLGADA	Poly (lactic-co-glycolic acid) diacrylate
PVA	Polyvinyl Alcohol
SEAL	Stamped assembly of polymer layers

SIV	Single Injection Vaccines
SKOV3	A cell line of human ovarian cancer
SMP	Shape Memory Polymer
SLA	Stereolithography
TEGDA	Triethlene glycol diacrylate
T_g	Glass Transition Temperature
T_m	Melting Temperature
TMHDI	Trimethyl Hexamethylene Diisocyanate
UV	Ultraviolet
WHO	World health organization
XPS	X-ray photoelectron spectroscopy
XRD	X-ray powder diffraction

TABLE OF CONTENTS

LIST OF FIGURES

1. INTRODUCTION*[1]

Drug delivery is crucial to maintain safety and efficacy of therapeutic agents used to treat ailments like infectious diseases and cancer. Various materials with tunable properties have been used as drug delivery vehicles with polymeric materials and metallic materials gaining more prominence due to their biocompatibility and surface properties, respectively. Engineering such delivery platforms to enable controlled release of therapeutic agents while maintaining their functionality is the need of the hour. Although previous studies have developed many polymeric and metallic drug delivery platforms, they have not been successfully translated into clinics. My work thus focuses on using these materials to enable safe and controlled release of a variety of therapeutic agents and enhance biocompatibility. The first part of this introduction will focus on polymeric delivery platforms specifically being used for therapeutic delivery. The need for efficient protein-based vaccine delivery systems as it relates to prevention of infectious diseases will specifically be highlighted. The second part of this introduction will shift the focus to metallic particles that can potentially be used for controlled release of small molecule drugs and challenges associated with biocompatibility of these materials. Last part of this introduction will introduce biomaterial-based scaffolds that can be used as drug delivery platforms because of their favorable surface properties.

---

*[1] Parts of this chapter were adapter from two articles. Reprinted with permission from “Engineering DNA vaccines against infectious diseases” by Lee, J., Arun Kumar, S., Jhan, Y. Y., & Bishop, C. J., 2018. *Acta Biomaterialia*, 80, 31-47, Copyright [2018] by Elsevier and “Controlling and quantifying the stability of amino acid-based cargo within polymeric delivery systems” by W. N., Arun Kumar, S., Prasca-Chamorro, D., Moore, D. M., Good, J., & Bishop, C. J., 2019. *Journal of Controlled Release*, 300, 102-113, Copyright [2019] by Elsevier

Specifically, this section will discuss the need for adjuvant therapeutic strategies after tumor resection to reduce recurrent rate. Overall, my research work was focused on developing novel, biomaterial-based systems which could potentially be used as drug delivery devices to effectively treat cancer and infectious diseases.

1.1. Introduction to Vaccine Delivery

1.1.1. Infectious Diseases and Vaccines

Infectious diseases are caused by a variety of microorganisms including bacteria and viruses and can often lead to a decrease in the quality of life and increased risks of mortality. In 2016, 1.6 million people died due to human immunodeficiency virus (HIV) alone. The infectious disease burden can be delineated using disability-adjusted life years (DALYs). Infectious diseases were listed by the World Health Organization (WHO) as a number of the top contributing issues to human health [1].

Various therapeutic and preventative interventions have been used to combat infectious diseases. Vaccination in particular has played a critical role in preventing, treating, and even eradicating diseases (i.e., smallpox). Poliomyelitis or polio is another deadly infectious disease, and this disease in particular mainly affects children. The inactivated polio vaccine and oral polio vaccine are two types of vaccines that helped reduce polio by 99% worldwide; and now 80% of the population worldwide live in polio-free regions [2, 3]. Unlike inactivated vaccines, subunit vaccines contain small purified pieces of the infectious agent including proteins. The origins of protein-based therapeutics can be traced to 1978, when human insulin was first produced using recombinant

DNA (rDNA) technology by David Goeddel's laboratory at Genentech [4-7].The resulting commercialization of human insulin by Genentech and Eli Lilly propelled further investigation into the use of rDNA technology for therapeutic production [4, 5]. Today, protein and peptide therapeutics not only target a breadth of conditions, ranging from genetic disorders to autoimmune diseases, but are also used as vaccines to prevent various infectious diseases [8]. With over 190 drugs and 10 recombinant protein vaccines currently approved by the U.S. FDA, protein and peptide therapeutics are arguably one of the most promising therapies available today, in part owing to their unparalleled degrees of specificity, lowered immunogenicity, and potentially shorter FDA approval times due to 510(k) approval processes [5, 8].

Protein and peptide therapeutics are commonly encapsulated within polymeric delivery systems [9-12]. The highly sensitive nature of amino acid-based cargo (AAC), which includes both proteins and peptides, and their instability when exposed to harsh conditions poses a unique challenge to the field. Amino acid-based cargo (i.e., peptides, antigens) inherently has thermostabilizing issues, as the structure is directly responsible for its function. Besides the critical nature of protecting antigens *ex vivo*, when endeavoring to control the kinetics of cargo being delivered over long durations that have auto-boost capabilities, the antigen must be protected within the context of a biological system. In the case of depots, even if there is no contact with water that could cause hydrolytic damage, pre-existing humidity within the depot could substantially reduce functionality, as well as thermo-instability of the cargo at body temperature.

In addition to the effects of moisture and temperature, pH plays a critical role in manipulating the stability and behavior of proteins [13], impacting the success of delivering protein- and peptide-based drugs [14]. Additional processes affecting protein instability include deamidation, oxidation via free radicals, covalent modifications with reducing sugars, deglycosylation, succinimidation, and non-disulfide crosslinking [15-17]. As a result of these combined factors, the effects of the overall formulation, manufacturing process, transport method, storage conditions, and patient administration must be carefully considered to ensure both efficacy and safety [15, 18-25].

Despite measures taken to counteract such destabilizing pressures, the challenge of maintaining the stability of AAC systems remains. The impacts of protein and peptide instability are particularly evident in developing nations, where the strict requirements for temperature-sensitive transport and storage are often not met [26-29], and the consequences of poorly maintained cold-chain storage of vaccines are apparent in the referenced data: [28, 30, 31]. During cold-chain storage, vaccines can be accidentally frozen. In one case, a literature review conducted by Matthias et al., in 2007 reported that between 75% and 100% of vaccine shipments were exposed to accidental freezing during shipment and storage [31]; this statistic is particularly problematic, considering that freeze-sensitive vaccines are estimated to account for over 31% of vaccine expenditures made by the United Nations Children's Fund in 2005 [26]. In other cases where there is incomplete cold-chain storage, excessive temperatures can damage the vaccine. An example of this challenge is Influenza vaccine which is a live and attenuated virus and is known to be heat sensitive in non-cold storage conditions [32] . Antigen stability is thus a formidable challenge in today's world given that transportation of existing vaccines poses a limitation in the absence of a complete cold chain en route to third world countries. This further underscores the need for further research targeting improved methods of stabilizing protein and peptide cargo.

In addition to optimal transportation and storage conditions of the vaccines, formulation and timely administration of vaccines are also crucial. Many of the approved vaccines require multiple doses at a pre-determined time and failure to follow the schedule could result in incomplete vaccination. In the developing world, timely administration of the vaccines, especially to the children, is challenging thus warranting a need for single-injection vaccines enabling timely administration of multiple booster shots over the course of months. Release kinetics of the vaccines from these systems is also important in ensuring optimal immunogenicity. Burst release of vaccines (similar to booster shots regimen) have proven to be effective with minimal side effects.

1.1.2. Current Polymer-based Technologies for Vaccine Delivery

Various platforms have been developed to regulate vaccine delivery rates while maintaining vaccine functionality. As mentioned earlier, these systems have not yet been clinically translated because of challenges related to limited cargo versatility, instability and unpredictable release kinetics. In this section, commonly used emulsion-based strategies and other non-emulsion-based delivery systems will be discussed.

1.1.2.1. Emulsion-based Delivery Systems

Emulsion-based polymeric microparticles (MPs) and nanoparticles (NPs) are commonly used as vaccine delivery platforms or as adjuvants [33, 34]. Polymers provide several advantages including biocompatibility, biodegradability, low toxicity, easy synthesis, and controllable size of scaffolds [35]. Polymeric MPs and NPs offer another advantage as they can easily be administered using non-oral or parenteral route as it is the most common delivery route. In an effort to better describe precisely how these methods are related to and potentially problematic for protein cargo, an overview of both the single- and double-emulsion processes will be presented (**Figure 1.1**).

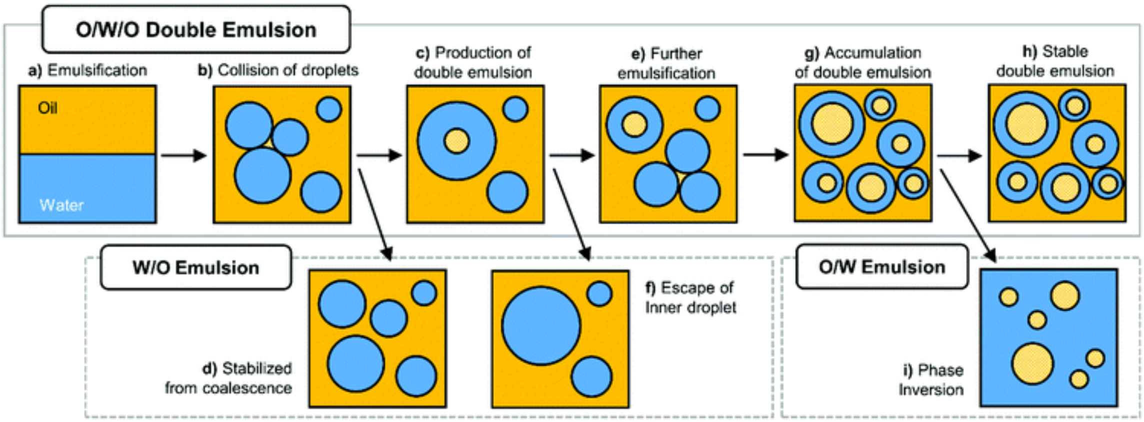

Figure 1.1 Scheme of single and double emulsion fabrication of polymeric NPs and MPs. Reprinted with permission from The Royal Society of Chemistry from Kim et al. [36]

In the single-emulsion water/oil technique, polymer in the organic phase and protein cargo in aqueous phase are emulsified, using either sonication or homogenization for NP or MP formation, respectively [37]. Similar to the single-emulsion method, the water/oil/water (w/o/w) double emulsion technique is also used to manufacture protein-encapsulated polymer-based MPs and NPs. Using this emulsion process, protein in the water phase is mixed with polymer in organic solvent, either with or without drug, to make a primary emulsion. The primary emulsion is then mixed with the second water phase. In addition to catering towards a slow and sustained release, the double-emulsion technique is used for encapsulation of multiple cargo [38].

In both of these processes, it is important to identify several of the potential risks posed towards protein cargo. Firstly, protein cargo coming into contact with either excess water or the water-polymer interface can undergo aggregation and denaturation as a result [39]. Moreover, protein denaturation can also result from the increased shear stresses experienced during the sonication or homogenization procedures. In the case of Poly (lactic-co-glycolic acid) (PLGA), protein degradation can also be caused by side reactions of the carboxyl groups of the degrading PLGA with the amine groups of the protein. In addition, as discussed previously, the degree of water content in the inner water layer for particles produced using the double emulsion process is critical. Although lyophilization and solvent evaporation can reduce the amount of water in the particles, excess residual water can alter the pH, resulting in rapid protein degradation.

1.1.2.1.1. Effects of pH on Antigen Stability

The microclimate pH (μpH) is a critical factor influencing the stability of protein and peptide cargo encapsulated in various polymeric drug delivery platforms, most specifically due to the hydrolysis mechanism responsible for their degradation [40, 41]. Hydrolytically degradable polymers such as PLGA are ideal for drug delivery applications due to their ability to release cargo in a slow and controlled manner in the presence of water and be eventually incorporated in the body [41]. PLGA's eventual degradation products are namely lactic and glycolic acid. Lactic and glycolic acid are metabolized in the tricarboxylic acid cycle and are eliminated as CO_2 and water, although glycolic acid is excreted via the kidneys as well. A significant challenge associated with these hydrolytically degradable platforms involves the prevention of cargo destabilization, as polymer degradation results in acid production, thereby altering the μpH [21, 42-44]. For example, the internal pH at the core of PLGA MPs has been shown to drop as low as 1.5 in degradation studies [45, 46]. At a pH this low, most polypeptide chains denature, exposing hydrophobic surfaces and leading to aggregation and potential chemical inactivation [47]. For instance, specific studies using BSA encapsulated in PLGA millicylinders have identified a direct correlation between decreases in μpH from 5 to 2 and quantifiable alterations to the structure of protein cargo [21]. Naturally, these structural changes compromise the therapeutic capabilities of the protein or peptide cargo, as well as limit the amount of drug released due to the formation of insoluble aggregates. In an effort to better stabilize AAC within polymeric delivery systems, thorough research has been conducted to inhibit pH changes within such platforms (Table S1). Due to the importance of maintaining an optimal μpH in AAC polymer-based drug delivery systems, researchers have developed many methods to control the pH throughout the polymer degradation process and subsequent release of the therapeutic. One of the most extensively studied techniques developed to combat drastic drops in pH within PLGA microspheres is the implementation of an internal buffer system using excipients such as ion exchanges. As a result, variety of salts have been studied for their potential buffering capacities and subsequently applied to protein stabilization studies. One study conducted by Zhu et al., involving the use of magnesium hydroxide ($Mg(OH)_2$), yielded promising results [10]. In this study, the researchers observed that release of BSA from PLGA millicylinders was limited to 20%, while approximately 80% of the encapsulated BSA had become insoluble after 28 days [10]. The researchers first simulated a PLGA microclimate and then added a 3% $Mg(OH)_2$ buffering solution to the BSA. The study results indicated that the pH dropped from 7.4 to 7 in the presence of buffer, as opposed to 7.4 to 3 without the buffer [10]. When applied to an experiment using PLGA microspheres, the co-encapsulation of $Mg(OH)_2$ with BSA, along with a few other proteins, was shown to decrease the formation of aggregates and resulted in an increase in protein release from 30% to >80%[10]. In addition to $Mg(OH)_2$, other slightly soluble antacid salt solutions, such as $MgCO_3$ and $ZnCO_3$, have also shown significant promise in terms of stabilizing protein cargo within PLGA microspheres [92].

Aside from salt buffer solutions, other protein stabilizing agents have been shown to inhibit drastic changes in μpH. In a study conducted by Park et al., dermatan sulfate (DS), a glycosaminoglycan commonly used as a biomacromolecule stabilizer and excipient, was co-encapsulated with BSA in varying ratios within PLGA microspheres [43]. As a result of its negative surface charge, DS has been shown to shield proteins at a pH of 3 due to the polysaccharide's favorable interaction with positively charged proteins below their isoelectric point (pI) [43]. As hypothesized, higher amounts of DS co-encapsulated with BSA yielded greater percentages of BSA release due to decreased formation of insoluble aggregates [43]. While the results of this study are promising, it is important to note that additional studies are needed to test the effects of DS on the release of proteins with pI values different from that of BSA [43].

1.1.2.1.2. Effects of Temperature on Antigen Stability

Of all the factors influencing the stability of proteins and peptides, temperature is arguably one of the most important [15]. However, in an in vivo context, temperature is not a variable that is controllable in terms of polymeric drug delivery systems. Protein instability is correlated with increasing temperatures. Moreover, sufficiently low temperatures have also been shown to cause protein denaturation [48], although cold denaturation is generally considered more of a reversible process [49]. The optimal temperature of a protein is influenced by both the surrounding enthalpic and entropic forces [15].

Generally, most proteins are stable within a specific temperature range and are associated with an unfolding temperature (also referred to as melting temperature, or T_m) at which 50% of the protein become unfolded. For most proteins, this value is between 40 and 80 degrees Celsius [15]. Table 2 reports the melting temperature, enthalpy of protein unfolding, and Gibbs free energy of protein unfolding for several selected proteins compiled during a literature search. Melting temperature, or the unfolding transition midpoint, can also be described by the point at which the Gibbs free energy of unfolding

(ΔG_u) is equal to zero, where ΔG_u represents the difference in free energy between the folded and unfolded states. The thermodynamic stability of proteins can also be quantified by the enthalpy of unfolding (ΔH_u), which is affected by both the degree of hydration and the change in intramolecular bonding forces during the protein unfolding process [50]. Because melting temperature plays such a critical role in determining the thermodynamic stability of a protein, much of the recent research in the field of protein stability has been centered on methods of predicting T_m computationally [51-54]. In one study conducted by Ku et al., researchers found a correlation between the T_m and dipeptide sequences present in the genome of hyperthermophilic bacteria using statistical inferencing to distinguish relative effect on T_m for 400 possible dipeptide combinations [51]. Rapid T_m prediction techniques such as this one can serve as a promising method of enhancing the stability of protein therapeutics via protein engineering, although much research is needed before robust methods of prediction can be developed. In order to understand such correlations, however, it is necessary to first understand the role that temperature plays in determining protein and peptide stability. Within AAC polymeric delivery systems, the importance of temperature becomes further magnified as an increasing number of variables come into play.

1.1.2.1.3. Release Kinetics of Antigen from Emulsion-based Delivery Systems

Polymeric MPs and NPs that are encapsulated with the antigen can cater a variety of release profiles including burst release, sustained release, delayed sustained release, and a combination of different release profiles. PLGA is one of the most common biodegradable polymers that has been approved by Food and Drug Administration (FDA) for use in many controlled drug delivery formulations. PLGA is a bulk eroding polymer as it degrades uniformly throughout the polymer causing an overall volume loss while maintaining the structural integrity until complete degradation (**Figure 1.2**). Water diffuses into the polymer during the degradation process resulting in the formation of pores. These water-filled pores increase in size overtime causing a network of pores eventually facilitating drug release. In a matrix-based delivery system, the antigen is mixed with the PLGA and is ultimately released from the matrix through diffusion. Use of this matrix system causes release rate of the antigen to be constant which is often referred to as sustained release until PLGA is completely degraded. Previous studies have shown that sustained release of antigen is not ideal as it can damage the antigen and could potentially also cause immunological tolerance. If an antigen is encapsulated in a PLGA MP or a NP, then most of the encapsulated antigen will likely be released upon complete degradation resulting in a burst release. One caveat to the encapsulation strategy is that the timing of the burst release from the MPs and NPs are less predictable and controllable. Encapsulation strategies often result in one or more antigen pockets within the MPs and NPs and the thicknesses of polymeric shell around these pockets are variable. This variability often results in early burst release of pockets that are closer to the surface further impeding clinical translatability of these polymeric particles for vaccine delivery applications.

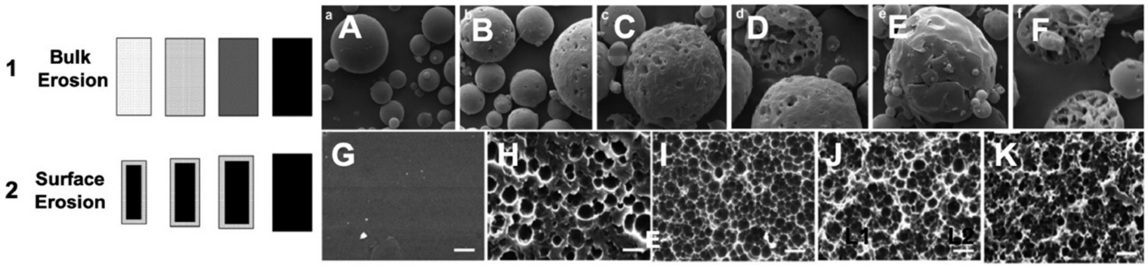

Figure 1.2 Scheme of Bulk Erosion and Surface Erosion Processes of polymeric NPs and MPs. Reprinted with permission from The Royal Society of Chemistry from Souery *et al.* [36, 55]

1.1.2.2. Non-Emulsion-Based Drug Delivery Systems

Harsh synthesis conditions, variability in pH, and non-ideal release kinetics of emulsion-based polymeric delivery systems steered the focus towards other delivery platforms with milder and controllable fabrication techniques. The goal of these techniques is to minimize alterations and instabilities of the proteins' secondary and tertiary structures, which are otherwise commonly caused by solvents interfaces in emulsion-based systems.

1.1.2.2.1. Nanoprecipitation

Nanoprecipitation is a simple and reproducible technique that is often used to fabricate polymeric nanoparticles such as nanospheres and nanocapsules [56]. Nanoprecipitation is often used to encapsulate hydrophobic drug using a two-step process (**Figure 1.3**). Polymer and drug are mixed in an organic solution (solvent phase) and are added drop wise to an aqueous solution (non-solvent phase) under magnetic stirring conditions. Interfacial deposition of the polymer caused by the escape of non-solvent phase that is partially miscible in water results in the formation of nanoparticles. These particles are then recovered through solvent evaporation to remove organic solvent and ultracentrifugation to remove aqueous solvent. Additionally, surfactants are usually added to the aqueous solution to prevent aggregation of nanoparticles. Although this fabrication process is similar to that of emulsion technique discussed previously, nanoprecipitation method does not involve intense physical agitation and is often modified to reduce the water-organic solvent interface that is increased in emulsion-based systems. These modifications include optimization of various conditions during nanoprecipitation including pH, temperature, and mechanical stirring. Instability in case of protein-based cargo could result from these changes and thus serves as a major limitation of nanoprecipitation [57]. Additionally, solvents used in nanoprecipitation could be difficult to remove and hydrophilic proteins are often difficult to incorporate with this technique [58]. These challenges with nanoprecipitation technique thus warrant the need for other non-emulsion based methods.

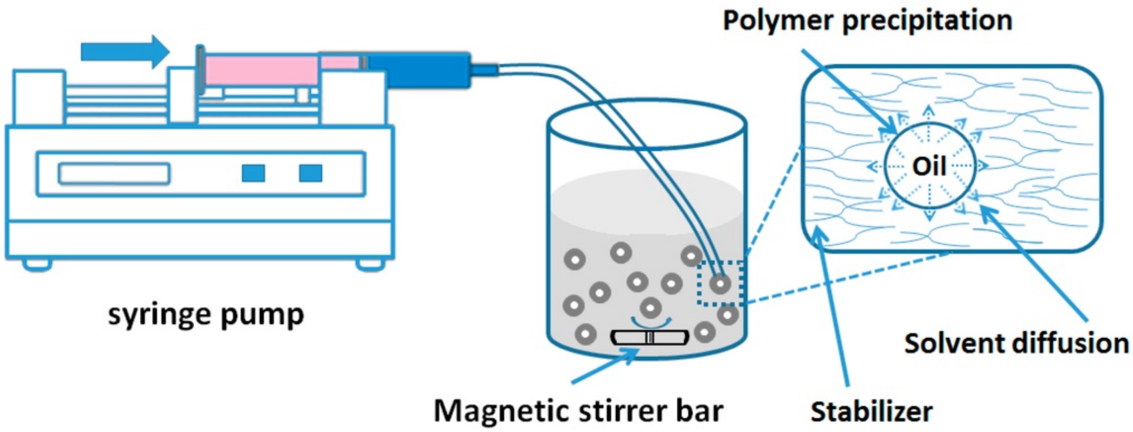

Figure 1.3 Scheme of Nanoprecipitation Method to Fabricate of polymeric NPs. Reprinted with permission from MDPI from Wang *et al.* [59]

1.1.2.2.2. Metallic nanoparticles

In contrast to polymeric NPs, metallic NPs are non-degradable and rigid thus reducing the generation of toxic byproducts and increasing structural integrity. Unlike polymeric NPs, metallic NPs have the potential to elicit high immune response through cytokine induction and can thus be used as vaccine adjuvants [60, 61]. Metallic NPs have highly tunable surface properties and are relatively simple to synthesize. These NPs tend to be highly porous and have chemical moieties that can be used to functionalize for targeted therapy. High surface area of these materials also provides an avenue to increase cargo loading onto the structures. Timing of cargo release can also be precisely controlled in many metal nanoparticles that are stimuli-responsive. For example, gold, carbon, and silica NPs are commonly studied for drug delivery applications specifically in cancer therapy. These NPs with favorable optical and surface properties provide exciting opportunities to be used as vaccine carriers [62]. Vaccine antigens of the target infectious agent can either be encapsulated within the metal NPs or be attached to the surface of the metallic NPs.

Gold NPs, in particular, are well-studied for various biomedical applications for decades and has good track record in terms of biocompatibility. Gold NPs also possess desirable tunable and optical properties that can be leveraged to optimize cargo loading, protection, and release [63]. Chiodo et al. formulated glyco-gold NPs by assembling HIV envelope glycoprotein, gp120, antennas [64]. These glyco-gold NPs enhanced the immune response by facilitating superior binding between the gp120 mannose and anti-HIV antibody. This gold NP delivery system of subunit vaccines indicates the potential use of metallic NPs as effective antigen carriers for vaccine applications to enhance immune response and vaccine functionality.

Despite the advantages of metallic NPs, there are several challenges that limit their use in clinical settings. Many metallic NPs are prone to instability especially when there are fluctuations in ionic concentration and temperature of their environment [65]. Additionally, there is an absence of long-term safety studies for many metallic NPs resulting in uncertainty of their clinical use. Accumulation of metallic NPs within the body is also a cause of concern as these NPs generally do not degrade. Lastly, because of their small size, use of metallic NPs is limited to small biological or drug molecules. Novel metallic nanoparticles with in-depth biocompatibility analysis are thus needed to address the current challenges with this group of NPs.

1.1.2.2.3. 3D Fabrication

In addition to nanoprecipitation, other fabrication techniques are used to develop 3D microstructures for efficient delivery of cargo including Fused Deposition Modelling (FDM), Stereolithography (SLA), and StampEd Assembly of polymer Layers (SEAL). FDM and SLA are traditional fabrication methods that are commonly used for drug delivery applications due to their high drug loading capacity. There is a trade-off in each of these approaches, which can especially turn out to be costly with respect to protein-based cargo delivery.

In FDM, polymers are often mixed with the cargo using hot melt extrusion (HME), a process in which polymers are melted and mixed with the drug under high temperature and pressure conditions [66]. This method is economical, has high throughput manufacturing potential, and is often studied for applications in controlled oral delivery systems. For example, Kempin et al. evaluated the use of FDM to formulate a variety of polymer-based drug eluting implants including ethyl cellulose and polycaprolactone. Model drug, quinine, was mixed with the polymers using HME and the mixture was printed as hollow cylinders using an FDM printer [67]. As previously discussed, protein-based cargo is extremely sensitive to temperature, and thus, this method could compromise protein functionality. Although this method is easy to set up and can facilitate optimal dosage forms, FDM is only suitable for drugs, like small molecules, that can withstand high temperature.

SLA is another emerging approach that can result in complex 3D polymeric structures with high resolution [68]. Polymers that are sensitive to light are used as resin, which can in turn be solidified when exposed to a laser light source. Although this is a relatively simple process, cargo localization is challenging with the use of SLA technology. Multiple cargo layers are stacked between the polymer layers and are solidified sequentially. This not only limits the type of release kinetics that can be achieved with such a system but also exposes more cargo to the polymeric layers, which could in turn cause instability with respect to protein-based cargo.

In contrast to the two traditional 3D printing approaches that was previously described, a new microstructure fabrication technique called StampEd Assembly of polymer Layers (SEAL) has recently been developed. SEAL method could potentially be used to fabricate small polymeric structures with complex geometries [69]. In this method, molds of desired geometry are fabricated using silicon-based materials (**Figure 1.4**). Polymer base is heated and poured onto the silicon patterned mold and the resulting mold structure with an empty core is delaminated as a first layer onto a surface. Model protein-based cargo is then dispensed into the core using a picoliter dispenser. The protein-based cargo core is later sealed using a second polymer "lid" layer. Sealing of the two layers is accomplished by creating a thermal bond using heat. Unlike the other two fabrication techniques discussed, SEAL technology enables precise control over release kinetics of the cargo upon successful sealing. However, one major limitation to this approach is the high failure rate of sealing of the two layers. If the microstructures are not sealed adequately, then they could result in premature release of the protein-based cargo. Timing of the cargo release is especially crucial for applications such as vaccine delivery and any uncertainty in the release kinetics could result in reduced immunogenicity of the cargo. This sealing challenge resulted in clinical translatability of this technique being limited.

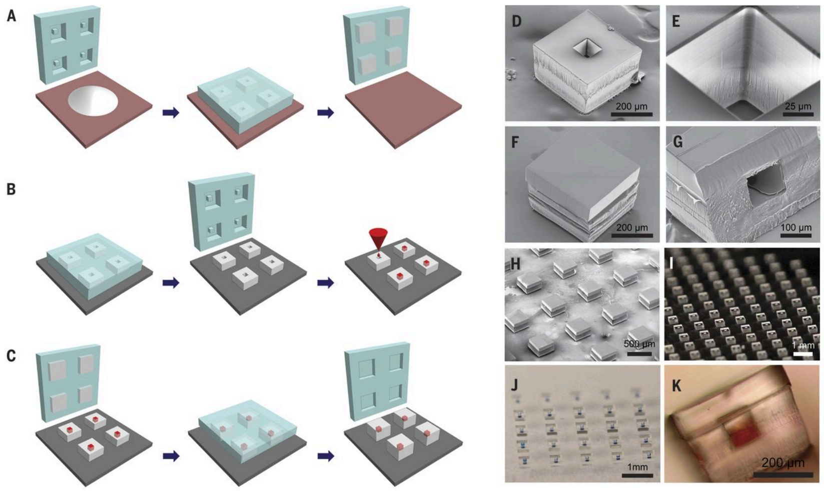

Figure 1.4 Scheme of SEAL Technique used to Fabricate PLGA Microstructures. Reprinted with permission from The American Association for the Advancement of Science from McHugh *et al.* [69]

1.1.2.2.4. Microneedle Fabrication

Microfabrication techniques like photolithography, silicon etching, and laser cutting have been used to fabricate microneedles. Diverse types of microneedles have been developed that are geared towards drug delivery applications out of which solid microneedles are commonly used for vaccine delivery (**Figure 1.5**). Variety of materials including silicon, metal, and polymers are used to fabricate solid microneedles that are often used for transdermal delivery of drug and vaccine. Silicon microneedles have shown good biocompatibility and mechanical strength resulting in desirable skin penetration. Traditionally, microneedle patterns are designed using photolithography on the backside of silicon wafers. Deep-reactive ion etching (DRIE) is then carried out to result in a deep hole on the backside of the silicon wafer. Photolithography can subsequently be used to create a pattern that was aligned right above the hole created through the back of the wafer.

Pillars can be created around this pattern using DRIE and can subsequently be sharpened into conical needles using hydrofluoric acid and nitric acid through isotropic etching. Alternatively, dissolvable microneedles are commonly fabricated using biodegradable materials through solvent casting method [70]. In this method, PDMS needle mold is created as a primary mold based on the desired microneedle structure [71]. Thicker metal sheets were laser-cut and subsequently were coated with PDMS layer to be aligned on the surface between the pyramidal holes in the primary PDMS needle mold. Molten polymer was then casted onto this mold composite resulting in a pedestal microneedle structure after cooling.

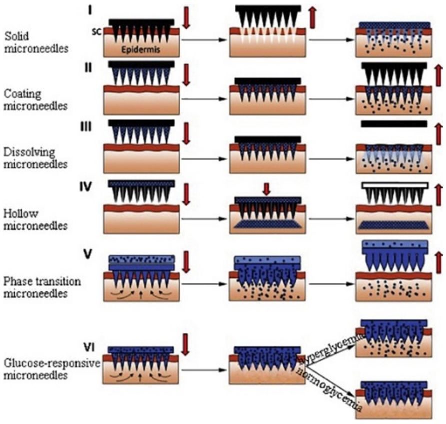

Figure 1.5 Different Types of Microneedles Used for Drug Delivery. Reprinted with permission from Elsevier from Chen *et al.* [70]

Drug can be loaded in a variety of ways onto these microneedles based on properties of drugs. Drug solution can be used to coat the microneedles or be filled within the silicon holes created after the etching process. Additionally, microneedles can also be engineered to have hollow needle structure enabling it be to a tube facilitating the introduction of drug into the skin from the patch that the microneedle is attached to. Drugs can thus be released in different patterns depending on where the drug is localized in the microneedle patch. Solid and dissolvable microneedle patches with variable drug localization have successfully been synthesized in the past for applications in vaccine delivery [72, 73].

Although microneedle fabrication is a good alternative to emulsion-based systems, there are several limitations. Firstly, timing and concentration of drug release from microneedles are not well controlled. Secondly, there is also limitation in cargo type based on the cargo size as bigger molecules are challenging to be delivered across the skin. Lastly, microneedles tend to be prone to skin irritation and contamination as there are limited sterilization techniques that can be used without compromising the needle structure. There is thus a need for alternative delivery systems that has better cargo versatility, precise control over timing of release, and is less prone to irritation in patients.

1.1.3. Overall Challenges with Current Vaccine Development Platforms and Future Perspectives

Controlled delivery of vaccines in the developing countries is essential to minimize mortality resulting from preventable infectious diseases. Many single injection vaccines (SIVs) have been developed using different fabrication techniques to improve vaccine stability and efficacy. However, there are several challenges to be addressed to enable clinical translation of SIVs, including: 1) limited cargo versatility and increased solvent exposure of cargo in polymeric emulsion-based systems, 2) inadequate thermostability leading to vaccine instability during transportation and storage, 3) limited drug release profiles to enable timely bolus administration, 4) poor biocompatibility of new delivery carriers including metallic NPs. To address these challenges, there is thus a need for novel, thermostable, and biocompatible vaccine delivery platforms to enable controlled release of functional vaccine from a single depot.

1.2. Introduction to Chemotherapeutic Delivery

Cancer is the second leading cause of mortality and is estimated to cause deaths of ~600,000 people in 2019 in the United States alone [74]. For solid tumors, one of the primary medical interventions include surgery where the tumor is resected along with a portion of the surrounding tissue to ensure that there are no cancer cells left behind. For example, glioblastoma (GBM) is an aggressive brain tumor and has a high recurrence rate. Surgery is often used as a primary intervention and is followed by adjuvant chemotherapy. It is important to note that chemotherapy is a non-targeted treatment strategy that could negatively impact the normal cells resulting in undesirable side effects. Additionally, drug resistance remains to be major challenge in this method. Even if there is an initial response to the treatment after the surgery, many cancers acquire resistance over time. There is thus an overall tradeoff between greater resistance potential and greater initial response.

Combinatorial therapy against cancer can possibly slow the development of resistance and can also improve treatment efficacy [75]. By using therapeutic agents against multiple targets, development of resistance could be delayed. Synergy between the agents can cause them to target different pathways or counter the side effects of chemotherapeutic drugs. By targeting different pathways, high dosage related toxicity can also be avoided [76]. It is also important to consider simpler system to optimize its functionality. Drug approval process is tedious and involves screening by six centers of FDA (CDER, CDRH, CDER, CTP, CVM, CFSAN). Because of the complex screening parameters regulated by FDA, effective systems that are simpler are more likely to be considered for approval.

Although combinatorial approach is effective, salvaging normal tissue is critical in vital organs like the brain, and there is currently no accurate detection method to predict the boundary of cancer cells. This results in retention of cancer cells that will later be responsible for cancer recurrence. It is also interesting to know that only 65 to 75% of GBM patients are eligible for surgical resection because of the challenges with accessibility of the tumor. In addition, previous literature have also linked the possibility of increased occurrence of metastasis through a) the tissue void that exists after resection through which the cancer cells can escape, or b) post-operative stress [77, 78]. There are several approaches that can be used to facilitate controlled delivery of chemotherapeutic agents which are discussed below.

1.2.1. Polymeric nanoparticles

As described earlier, high cytotoxicity and high chance of resistance are challenges with the delivery of free chemotherapeutic drugs. To overcome these limitations with chemotherapy, controlled release of drugs is essential, which can be accomplished using carriers. Polymeric NPs are commonly used to encapsulate chemotherapeutic drugs and to enable sustained release of the drugs at the target site. These drug-encapsulated NPs are often injected intravenously and can undergo passive or active targeting [79, 80]. Tumor cells are often characterized by leaky vasculature and defective lymphatic drainage system. This tumor microenvironment is utilized by the NPs where the particles can enter the tumor through the leaky vasculature and are not easily drained out of the system because of defective lymphatic drainage. This type of passive targeting is known as the enhanced permeability and retention effect. In active targeting, NPs are conjugated with a moiety specific to the receptors present in the surface of the tumors. This type of targeting results in highly selective accumulation of therapeutic agents in the target cells. Active targeting is thus successful in improving therapeutic efficacy and reducing side effects.

Concept of targeted chemotherapy using drug-encapsulated NPs is advantageous over administration of free drug in terms of small molecule-based monotherapy. However, recent studies have highlighted the importance of using different types of therapeutic agents against multiple targets in delaying the development of resistance. Synergy between the agents can cause them to target different pathways or counter the side effects of the chemotherapy drugs. By targeting different pathways, high dosage related toxicity can also be avoided [76]. Additionally, it was also observed that the required drug dosages were reduced drastically while maintaining the therapeutic potential by controlling the release pattern of these synergistic drugs. As discussed earlier, emulsion-based polymeric NPs have limited cargo versatility as the fabrication conditions often increases the risk of instability with respect to sensitive cargo [81]. Polymeric NPs are also biased towards hydrophobic agents as they are readily soluble in organic solvents that are used in the synthesis process. Precise control over release timing of multiple agents using polymeric NPs cannot be achieved thus posing a challenge to catering combinatorial chemotherapy regimen.

1.2.2. Metallic nanoparticles

Similar to polymeric NPs, metallic NPs can also be used to deliver chemotherapeutic drugs through passive or active targeting. In addition to improved therapeutic efficacy and reduced cytotoxicity, metallic NPs can also serve as contrast or hyperthermic agents. These theranostic NPs are also observed to improve cell uptake because of their size and surface properties. These NPs have superior optical and chemical properties enabling them to provide better tumor targeting, detection, and treatment compared to polymeric NPs [82]. For example, AuNPs have been widely studied as a carrier for chemotherapeutic drugs like paclitaxel and DOX because of their non-toxic and tunable properties. Specifically, AuNPs have been extensively used to improve treatment efficacy in melanoma (**Figure 1.6**). In another example, Nima et al. fabricated DOX-conjugated gold nanorods (AuNRs) with targeting antibody to improve selective DOX delivery in breast cancer cells called MCF-7 [83]. AuNR-mediated delivery of DOX resulted in significant reduction of cancer cell viability in MCF-7 cells. AuNRs are also known to absorb light at near-infrared (NIR) wavelength and convert the optical energy to heat energy. This property is crucial for two reasons: 1) NIR light can penetrate skin enabling on-demand activation of drug-conjugated AuNRs, 2) AuNRs can be used for thermal therapy based on its ability to generate heat upon activation. Lee et al. studied this photothermal property of AuNRs as it relates cancer treatment [84]. AuNRs were conjugated with TiO_2 NPs and then were incubated with cancer cells for 24 hours. Cells along with the NPs were exposed to NIR irradiation for 5 minutes and cell viability was subsequently measured. Cancer cell viability significantly reduced by ~40% with NIR activation validating the potential use of AuNRs in photothermal therapy of cancer.

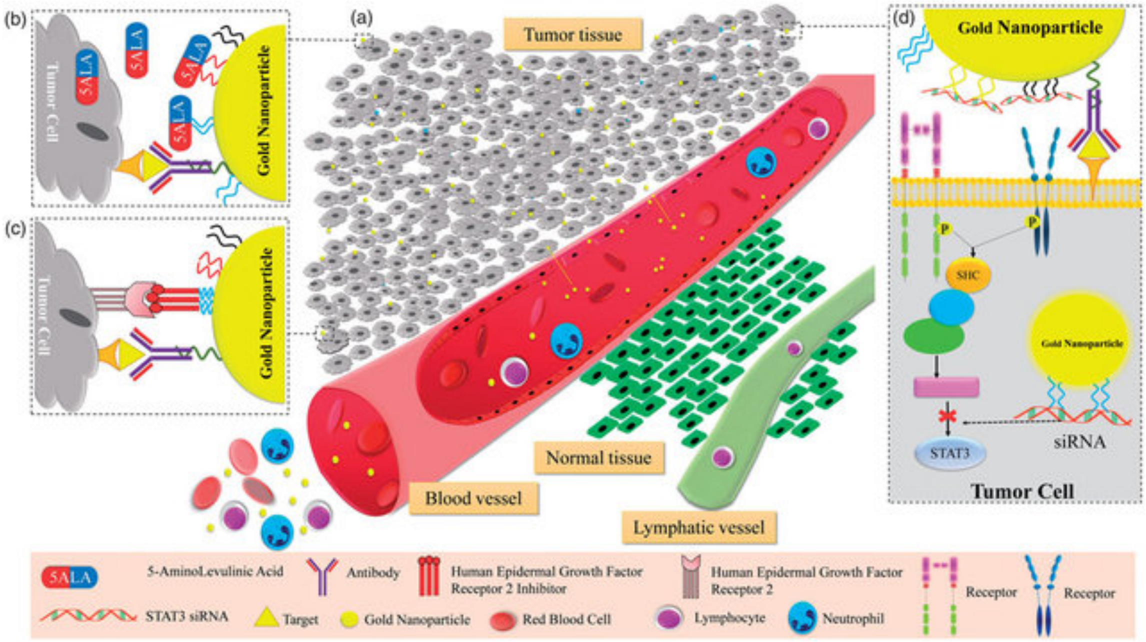

Figure 1.6 Different Types of Microneedles Used for Drug Delivery. Reprinted with permission from Taylor & Francis from Bagheri et al. [85]

Although metallic NPs hold promise as chemotherapeutic theranostic carriers, there are several limitations that would have to be addressed to enable clinical translation of this technology. Long-term cytotoxicity and biodistribution of metallic NPs like AuNRs are not fully studied resulting in reluctance with respect to clinical use. Because metallic

NPs are non-degradable, their accumulation in human body and the related inflammation effects on organs should be thoroughly understood [86]. Although short-term animal studies (6-month span) show promising biocompatibility of some metallic NPs like AuNPs, long-term clearance and safety concerns of many metallic NPs still need to be addressed. Emerging metal-based novel nanomaterials with favorable surface properties should thus be modified to ensure good biocompatibility and successful clinical translation for anti-cancer applications.

1.2.3. Drug-loaded sutures

Biodegradable sutures have been widely used to close the wound after surgery, and there have also been efforts to use these sutures as a drug delivery system [87]. However, only few drug-eluting sutures have been clinically translatable due to a number of challenges including non-optimal mechanical strength of the sutures and inability to achieve sustained release. Poor control over the drug released from the sutures further results in compromised therapeutic efficacy. Sutures are often dipped in the drug solution resulting in immediate uncontrolled release of the drug. Drug residence time in the body is thus less to achieve the desired therapeutic effect. Another major concern relating to absorbable sutures is the increased inflammation. In the context of tumor resection, sutures often do not cater precise sealing of the wounds. As a result, area around the wound that is not in contact with the suture might pave way for the residual cancer cells to escape. This major challenge requires development of newer materials to enable efficient chemotherapy delivery and sealing of the surgical void.

1.2.4. Injectable drug-loaded hydrogels

An alternative to sutures is post-operative biodegradable implants, specifically hydrogels. Hydrogels have been extensively characterized for their ability to enable drug release. Chemotherapeutic drugs are can be injected into or mixed with the hydrogels prior to crosslinking [88]. Drug-loaded hydrogels can then be placed near the surgical resection site for localized delivery of therapeutics. Hydrogels can be engineered to be responsive to various stimuli including temperature and pH further releasing cargo. For example, tumor microenvironments tend to have lower pH compared to the physiological pH. Chemical engineering of hydrogels to improve their sensitivity in low pH environment can lead to preferential delivery of the cargo in the tumor microenvironment. Although this is a theoretically effective alternative to drug-eluting sutures for controlled drug delivery, hydrogels do not possess adequate tensile strength to enable precise control over the timing of drug release or sealing of the wound [89, 90]. Increased water content in the hydrogels yields a non-rigid and liquid-like structure making hydrogels an ineffective solution to precisely plug the tissue voids. This mechanical property also causes premature dissolution of the device resulting in non-controlled release of the cargo load. Mechanically strong materials with optimal surface properties have thus been sought after to ensure predictable release and effective sealing of tissue void.

1.2.5. Implantable Biomaterial-based Scaffolds

Polymeric scaffolds are mechanically rigid compared to hydrogels and have favorable surface properties that can be leveraged for use in controlled delivery.

Previous studies have explored use of *in situ* biomaterial-based nanofiber scaffolds for improving release kinetics of chemotherapeutic drugs [91]. Additionally, scaffolds can be tuned to mimic local tissue microenvironment thus promoting improved cellular adhesion. Nanofiber-based scaffolds possess high porosity and surface area enabling high drug loading and sustained release through diffusion [92]. Implantable scaffolds are thus commonly used for improving therapeutic efficacy of chemotherapeutic drugs. Implantable scaffold can be segmented based on the implant localization as described in **Figure 1.7**. Drug-loaded nanofibrous scaffolds have been explored for potential application in post-operative adjuvant therapy. For example, Palama *et al.* developed polycaprolactone (PCL) scaffolds that were loaded with a small molecule drug called dexamethasone (DXM) [93]. Electrospun PCL scaffolds used in this study enabled sustained release of DXM *in vitro* and improved cell adhesion of osteoblast-like cells. These promising results highlight the potential application of this scaffold in filling the post-operative osteosarcoma defect. Despite the mechanical and surface advantages provided by nanofibrous scaffolds, there are some limitations associated with the scaffolds. Many fibrous scaffolds are mechanically rigid resulting in decreased flexibility that could potentially lead to imprecise filling of post-operative tissue voids. Additionally, preventing burst release of drugs that is often observed with implantable scaffolds is challenging. This burst release in case of chemotherapeutic agents could lead to dose dumping and undesirable side-effects. Biocompatibility is also a cause of concern for newly developed implantable scaffolds thus delaying the possibility of clinical translation. These limitations have resulted in search for new degradable and biocompatible platforms that can enable sustained release of chemotherapeutics while ensuring that the post-surgical void is effectively sealed.

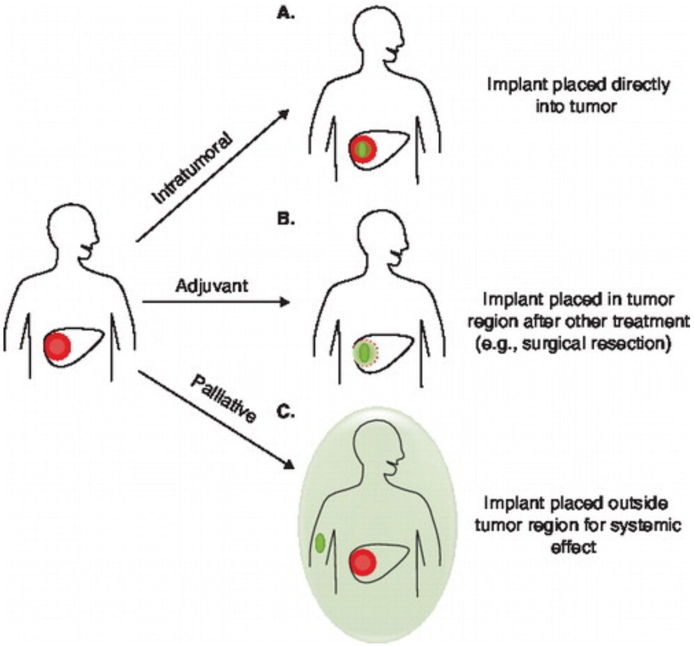

Figure 1.7 Three Main Types of Polymer Implants Used for Chemotherapeutic Delivery. Reprinted with permission from Taylor & Francis from Exner et al. [94]

1.2.6. Overall Challenges with Chemotherapeutic Delivery Platforms and Future Perspectives

Chemotherapy is the primary clinical intervention opted to treat many types of cancers. In the case of solid tumors like breast cancer, primary treatment often includes tumor resection where the tumor and small part of the surrounding boundary region is surgically removed. Although this is an effective strategy, cancer recurrences have been observed post-surgery in many patients. To reduce the chance of recurrence, chemotherapy is often administered in the free drug form as an adjuvant therapy after surgery. This approach tends to increase cytotoxicity as it can also affect the normal cells. There have been recent efforts to circumvent these challenges using nanoparticle-based formulations and other scaffolds that were discussed earlier. These technologies provide targeted therapy but have failed to gain traction in terms of clinical translatability for a variety of reasons. These include: 1) insufficient long-term biocompatibility and distribution evaluation with respect to new materials, 2) limited control over timely drug release from biomaterial-derived particles and scaffolds, 3) limited drug loading within the carriers, 4) lack of effective post-operative technologies to reduce recurrence rate with respect to solid tumors. There is thus a need for novel, biocompatible delivery platforms capable of high chemotherapeutic loading and precise control over release of chemotherapeutics.

1.3. Research Aims

Polymer-derived delivery platforms have been gaining popularity in recent years with respect to controlled vaccine and chemotherapeutic delivery. In developing countries, infectious diseases like malaria, HIV, and tuberculosis are the common causes of increased mortality. However, 1.5 million deaths are caused by vaccine preventable diseases due to limited vaccine coverage. There are many challenges limiting vaccine coverage including high cost associated with transportation and storage of temperature sensitive vaccines. Despite the promising results of polymer-based carriers developed for vaccine delivery, there are challenges associated with maintaining cargo stability and precisely controlling cargo that need to be addressed. To overcome these challenges, we propose to engineer a biodegradable, thermostable, and kinetically-controlled polyester-based delivery platform. Additionally, we propose to facilitate on-demand cargo release within this platform to enable timely bolus administration, which is especially crucial for complete vaccination.

With respect to solid tumor treatments, recent studies have shown that with surgical tumor removal, which is the primary clinical intervention, possibility of escape of residual cancer cells through the post-surgical cavity is higher. Conventional efforts for closing the surgical void and to avoid escape of cells include drug-eluting sutures and administration of free chemotherapy drugs. However, there are several challenges with these approaches including mechanical instability leading to premature drug release, increased risk of cytotoxicity, and high possibility of drug resistance. We propose two platforms that can potentially be used to circumvent these limitations: 1) novel, mechanically strong, and cytocompatible carbon nanofiber-based platform that will be used for biomedical applications including chemotherapeutic delivery in the future, 2) drug-eluting shape memory foams to reduce breast cancer recurrence rate.

The aims of this research involve engineering thermostable vaccine delivery platforms (Aim 1 & Aim 2), engineering cytocompatible nanofiber scaffolds for potential use in biomedical applications including drug delivery (Aim 3), and engineering drug-eluting shape memory foam to reduce breast cancer recurrence (Aim 4). Following specific aims were pursued to engineer and optimize biocompatible drug delivery platforms for effective vaccine delivery and cancer therapy:

Aim 1: Engineer and characterize polyester-based vaccine depot (Polybubbles)

a. Fabricate, physically characterize polybubbles and quantify solvent content

b. To enable antigen release from the polybubbles and asses antigen stability

Aim 2: Engineer NIR-activatable Polybubbles for on-demand vaccine delivery

a. To enable cargo centering within the polybubbles and delayed burst release of cargo

b. Incorporate and characterize gold nanorods within the polybubbles

c. To evaluate on-demand laser activation of polybubbles *in vitro*, *ex vivo*, and *in vivo*

Aim 3: Fabricate cytocompatible defect-rich MoS_2 incorporated carbon nanofibers

a. To synthesize polyacrylonitrile (PAN) nanofibers incorporated with defect-rich MoS_2 nanoparticles through electrospinning

b. To characterize morphological, mechanical, and electrical properties of the PAN/MoS_2 nanofibers

c. To evaluate cytocompatibility of the PAN/MoS_2 nanofibers for potential use in biomedical applications

Aim 4: Engineer polyurethane-based drug-eluting shape memory foam

a. To improve drug loading onto shape memory foam using viscosity modulating agents

b. To characterize crimping and expansion properties of the foam after drug loading

c. To quantify chemotherapeutic loading, release, and functionality of released chemotherapy drug in cancer cells

2. POLYMER-BASED SINGLE INJECTION DEPOT FOR DELAYED BURST RELEASE OF VACCINES*[2]

2.1. Introduction

Since the first vaccine against smallpox was developed by Edward Jenner in the eighteenth century, scientists have developed vaccines against numerous infectious diseases, including polio, measles, hepatitis B, rubella, and mumps, to name a few [95, 96]. Despite the success of vaccinations in preventing infectious disease, infectious diseases remain one of the main causes of death globally. For instance, lower respiratory infections were the third largest killer in 2015, despite the fact that vaccines are available for preventing pneumococcal disease and influenza, two of the disease's most common contributors [97-99]. Moreover, in 2017, hepatitis B was estimated to affect 257 million people around the globe and killed an estimated 887,000 people in 2015 due to complications from conditions such as cirrhosis and hepatocellular carcinoma [100]. In 2016, the World Health Organization (WHO) reported that the global coverage of hepatitis B was only 39% [98]. Moreover, the WHO also estimated that as many as 19.4 million infants in 2016 did not receive life-saving vaccinations, such as the diphtheria-tetanus-pertussis containing vaccines [101]. Statistics such as these underscore the lapses in providing access to immunizations worldwide.

---

*[2] Reprinted with permission from "An ultraviolet-curable, core-shell vaccine formed via phase separation" by Lee, J., Arun Kumar, S., Souery, W. N., Hinsdale, T., Maitland, K. C., & Bishop, C. J., 2019, *Journal of Biomedical Materials Research: Part A*, 107, 2160-2173, Copyright [2019] by Wiley

Poor immunization coverage in the developing world is often a result of the difficulties associated with maintaining vaccine functionality during transport and storage [32, 102-105]. More specifically, hydrolysis can greatly diminish the efficacy of amino acid- and protein-based vaccines [55]. In addition, proteins exposed to harsh temperatures during transportation and storage conditions can become denatured as a result [32, 106]. Because transportation systems in the developing world generally offer incomplete cold chains, antigen instability is often a common outcome of transport.

One reasonable approach to tackling the challenge of vaccine accessibility and coverage is the single-injection vaccine (SIV). SIVs are vaccines that do not require subsequent boosting (i.e., another injection) after the first dosage is received. For readers who are interested in a deeper study of SIVs, we would recommend referring to: [69, 107-111].

In this way, SIVs can significantly reduce the cost burden associated with immunization by requiring fewer vaccination visits and reducing the number of required medical personnel involved [112]. However, the main challenges of developing SIVs are: (1) engineering the release kinetics; (2) maintaining antigen stability, which is the most challenging [113]; and (3) accounting for potential sealing complications that can compromise the control over release [69]. Therefore, a strategy that combines the principles of SIVs while also addressing the aforementioned challenges would allow for expanded immunization coverage.

In this work, we report on the development of a poly(ε-caprolactone) (PCL)-based polymeric bubble ("polybubble") as a novel vaccine delivery carrier platform. Although we use the word "polybubble" to describe our system, the end product is not a bubble but rather a UV-cured shell containing cargo within, functioning as a vaccine depot. We refer to it as a polybubble because of the way in which the vaccine depot is formed.

Our polybubble system differs from traditional microparticles by the following: 1) traditional core-shell microparticles cannot be made using an aqueous core similar to our polybubble technology to the extent of our knowledge, as traditional microparticles generally use phase separations of multiple polymers and organic solvents to form a core and shell (i.e., [22]); 2) while traditional double-emulsion microparticles may contain aqueous droplets within them, similar to our polybubble technology, this method does not generally result in a burst (however, some cases of modest secondary boluses have been observed [114]). Generally, double-emulsion results in broader or continual release profiles. There have been reports published in regards to aqueous phases separated from other aqueous phases in a core-shell fashion; however, the outer shell would likely dissolve rapidly within the body as it is aqueous, and not highly useful for vaccine applications [115]. In cases of aqueous cores reported within organic solvent-based shells of polymer (i.e., via microfluidics), the solvent-exposed surface area differences for a similar dose are far favoring our type of technology in terms of denaturation, which could potentially significantly affect the cost of a commercialized vaccine [116] (Figure S1). Our technology also differs from other polymer depot systems in that no increase in temperature is required to seal the cargo within, which could potentially result in issues with early release and cargo denaturation.

Sustained release is generally undesirable for delivering a bolus, as the continual delivery of an antigen is likely to result in T cell anergy, which elicits little to no immune response and can also directly cause lymphocyte tolerance [117-119]. For instance, tolerogenic therapy is one common approach that harnesses T cell anergy in order to induce sustained tolerance to a particular antigen [120, 121]. For these reasons, it is undesirable to have a vaccine delivery system utilizing a sustained release mechanism. In order to avoid T cell anergy, many vaccines are delivered in bolus form at multiple time points because the first exposure is insufficient in triggering an antibody-generating immune response [122]. By harnessing a polymeric delivery system as a synthetic adjuvant, in combination with bolus delivery, the recipient of the vaccine would not need to receive multiple vaccine boosts, therefore avoiding the need for multiple trips to a medical clinic. The polybubbles described herein offer an alternative vaccination method that helps address some of the limitations of microparticle-based delivery; namely, temperature sealing issues to entrap an inner cargo, which could potentially cause early release or antigen denaturation upon failure [69]. By incorporating a 2-bolus release system and minimizing surface area contact with organic solvent to preserve cargo functionality (i.e. prevent antigen denaturation), these modifications may potentially alleviate the primary challenges associated with global immunization coverage.

2.2. Materials and Methods

2.2.1. Formation of PCL/PCLTA (14 kDa) polybubbles

14 kDa PCL was dissolved in chloroform at a concentration of 800 mg/mL. The PCL solution was then mixed with PCLTA and 0.005 g/mL of photoinitiator in a volume ratio of 1:3:2 (PCL: PCLTA: 2-Hydroxy-2-methylpropiophenone (photoinitiator)). This polymer solution was loaded and injected into the glass vial in the same way as the PCL polybubble formation procedure in the supplementary section (refer to: Formation of PCL polybubbles (80 kDa)). The resulting polybubble was cured under UV light for 10 minutes. After it was confirmed that the polybubble had cured, the polybubble was frozen in liquid nitrogen for 20 minutes and lyophilized overnight. The surface of the PCL/PCLTA polybubbles was analyzed by SEM.

2.2.2. Quantifying mass of chlorine released from the polybubbles

Polybubbles were incubated in 400µL of PBS at 37°C and the supernatants were collected at three time points: week 1, week 2, and week 3. The supernatants were then analyzed using comparator instrumental neutron activation analysis (NAA) to determine the mass of chlorine released. The amount of chlorine obtained from NAA were corrected to exclude the chlorine amount present in the PBS solution.

2.2.3. Quantifying of chloroform content in polybubbles and supernatants from release studies

Polybubbles were lyophilized at 2 hours, 4 hours, 6 hours, 20 hours, and 24 hours (n = 3). Mass fractions of Cl were determined by NAA [32]. Aliquots of 5-9 mg of each polymer sample were weighed and transferred by pouring the beads into pre-cleaned

LDPE irradiation vials. No utensils were brought into contact with the polymer beads. Chlorine calibrators were prepared from a certified, NIST-traceable calibrator solution (Inorganic Ventures), constituting ICCL1 in 0.050 mL aliquot of 1000 □ 3 □g/mL. Standard solution aliquots were dispensed accurately by volume into LDPE irradiation vials and were dried under a heat lamp. Neutron irradiations were performed using the Texas Engineering and Experiment Station 1-MW TRIGA reactor at a nominal thermal neutron fluence rate of $9.1*10^{12}$ cm^{-2} $seconds^{-1}$. Each sample or standard was irradiated for 600 seconds. The polymer samples were transferred after irradiation into clean, unirradiated vials, in order to provide blank-free determinations of Cl. Following 360 seconds decay intervals, gamma-ray spectra were acquired for 500 seconds using an HPGe detector. The data reduction was performed using the NAA software package from Canberra Industries. Nuclide ^{38}Cl with 0.6207 hours half-life and indicator peak at 2167.68 keV was used in the analysis.

2.2.4. Maintaining polybubble location and sphericity during formation

In order to both (1) maintain the polybubble location during the cargo injection phase and (2) preserve the sphericity of the polybubble during the curing phase, it was necessary to test the polybubble injection and curing process under several different reservoir conditions (**Figure 2.1:** blue), namely: (1) hydrogels composed of hydroxyethyl methacrylate (HEMA), tetra(ethylene glycol) diacrylate (TEGDA), and poly(ethylene glycol) methacrylate (PEGMA), (2) HEMA/carboxymethylcellulose (CMC), (3) trehalose, (4) CMC, and (5) PEGDA. If two different polybubbles are spherical and aspherical, as long as the minimal shell thickness is the same, the release time would likely be the same. The reason we are endeavoring to make our system spherical is to maximize the cargo capacity, while having the smallest diameter. By doing so, we can use the highest gauge possible with the greatest cargo capacity for subcutaneous or intramuscular injection. Furthermore, to help prevent the internal cargo bubble (**Figure 2.1:** yellow) from rising quickly through the polybubble's shell post-injection and rupturing into the main reservoir (**Figure 2.1:** blue), CMC at various concentrations was used to increase the viscosity of the cargo solution.

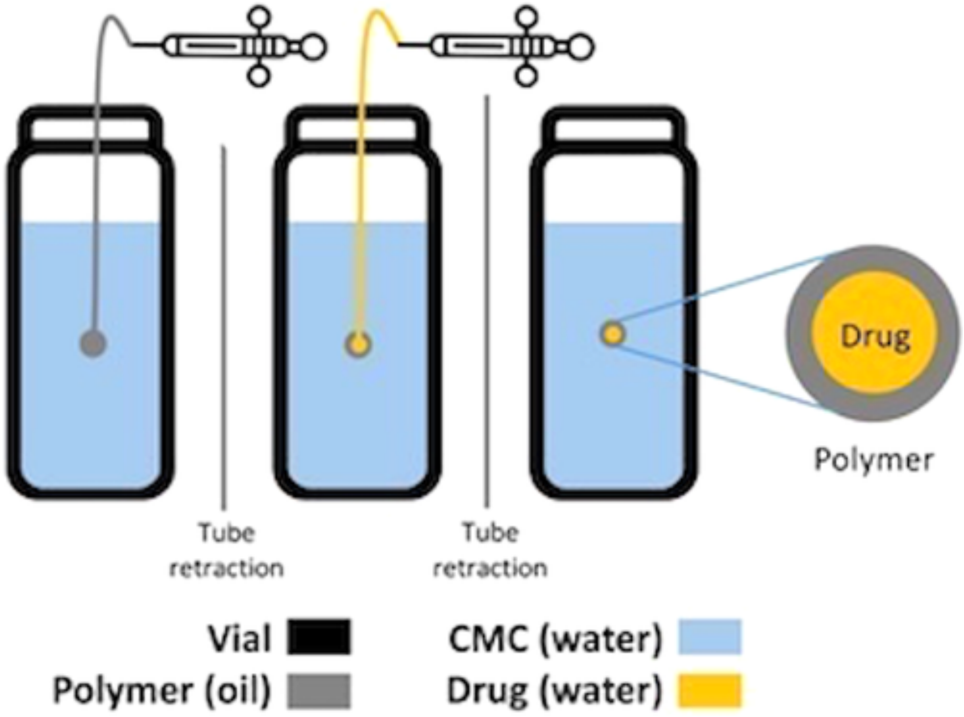

Figure 2.1 Polybubble Fabrication System: First, polymer (gray) is injected into the main CMC (10%) reservoir (blue) using a tube controlled by a micromotor. Following tube retraction, drug (yellow) is injected into the polymer during the second phase using a tube controlled by another micromotor to form the polybubble. The polybubble's location is supported by the main CMC reservoir, as its presence helps prevent the drug

from rupturing out of the polybubble and into the CMC. The main CMC reservoir also prevents leakage of drug following its injection. After each injection, the injection tubes are retracted. Reprinted with permission from John Wiley and Sons from Lee *et al.* [123]

2.2.5. Use of materials for maintaining polybubble localization

Please refer to the following sections for methods to maintain the polybubble location within the *Supplementary Materials:* PEG hydrogels for polybubble localization; HEMA/TEGDA hydrogels for polybubble localization; Use of HEMA hydrogel + 1.5% CMC solution for polybubble localization; Use of trehalose solution for polybubble localization; Use of 5% and 10% CMC solutions for polybubble localization.

2.2.6. Assessing cargo injection in the presence and absence of CMC

As mentioned previously, in order to prevent the internal cargo bubble (**Figure 2.1:** yellow) from moving upward post-injection and rupturing into the external CMC reservoir (**Figure 2.1:** blue media), CMC was mixed with the cargo solution to prevent its migration.

To test cargo migration in the absence of CMC, sample depots of acriflavine, doxorubicin, and BSA-CF680 conjugates were prepared. A 1% (w/v) acriflavine solution was prepared by dissolving 5 mg of acriflavine in 0.5 mL of phosphate-buffered saline (PBS). A 1% (w/v) doxorubicin solution was also prepared in the same way. The BSA-CF680 conjugates, 1% (w/v) acriflavine, and 1% (w/v) doxorubicin were then loaded into separate 1 mL syringes for injection. The glass vial was filled with 10% (w/v) CMC solution, and the PCL/PCLTA polybubbles were formed using 14 kDa PCL (1000 mg/mL). The syringe pump rate was held at 0.5 µL/sec for 10 seconds, and three different cargos were injected into three corresponding polybubbles using 34 G blunt tip needles. To test cargo migration in the presence of CMC, six different cargo solutions containing CMC were prepared using acriflavine, doxorubicin, and BSA-CF680 conjugates. To prepare acriflavine cargo with 3% and 5% (w/v) CMC, both 9 mg and 15 mg of CMC were weighed in separate microtubes and then added to two separate solutions containing 0.3 mL of 1% (w/v) acriflavine. 1% (w/v) doxorubicin solutions containing 3% and 5% (w/v) CMC were prepared using the same method previously described. In addition, 3% and 5% (w/v) CMC stocks of BSA-CF680 were also prepared. Polybubbles were formed in a 10% (w/v) CMC vial using the same syringe pump rate as before. The CMC-containing cargo solutions were loaded into separate 1 mL syringes and injected into corresponding different polybubbles using 34 G blunt tip needles.

Cargo retention in the middle of the polybubble compared to the shell was calculated based on ImageJ analysis. The fluorescence intensity of the cargo in the middle and in the shell was quantified using ImageJ analysis. A calibration curve was made based on the ImageJ intensity values as it corresponds to the cargo concentration. Mass percent was then calculated based on the intensity obtained from ImageJ and concentration from the calibration curve.

2.2.7. Polybubble diameter as a function of syringe pump rate, lyophilization and cargo presence

To prepare the polymer mixture, 14 kDa PCL was dissolved in chloroform at a concentration of 800 mg/mL. This PCL mixture was combined with PCLTA in a 1:3 volume ratio. 1 µL of the photoinitiator stock was added. The resulting polymer mixture was loaded into a 250 µL glass barrel, which was then connected to a syringe pump and driven into a glass vial containing 10% (w/v) CMC using a micromotor. The polymer mixture was dispensed near the bottom of the vial, but care was taken so that the polybubble would not come into contact with the bottom of the glass vial.

Using LabVIEW® software, the forward and backward motion of the micromotor was maintained at the speed set by the manufacturer. At the same time as the micromotor was used to drive the polymer-dispensing tubes, the syringe pump extruded polymer simultaneously. The syringe pump rate was varied from 0.0005 to 1 µL/sec.

To quantify polybubble diameters, a photo was taken of the vial, and the polybubble size was quantified via ImageJ using an electronic micrometer for calibration. Confocal microscopy was also used in order to assess the polybubble formation and cargo distribution (**Figure 2.4**) [33].

In regards to the polybubble diameter pre- and post-lyophilization and pre- and post-injection, please refer to the *Supplementary Material.*

2.2.8. Quantifying the effect of moisture content on thermal behavior of the polybubbles

To determine the moisture content within the polybubble, three PCL/PCLTA (1:3 v/v) groups were analyzed using DSC: 1) cured polybubbles that were lyophilized overnight, 2) cured polybubbles that were not lyophilized, 3) PCL/PCLTA mixtures in a non-polybubble form. Samples between 5-10 mg were placed in a T0 aluminum pan. Each DSC run ranged from 10°C to 60°C (Tm of PCL is ~55°C) with a ramp of 2°C per minute.

2.2.9. Quantifying the effect of emulsion-based particles on cargo release time

To determine the effect of microparticles and nanoparticles on cargo release time, 0.5 mg/mL of MPs/NPs were incubated in 1 mL of PBS at 37°C for 17 days. The solution was centrifuged at desired time points for 5 minutes (at 17000 RCF for NPs and 4000 RCF for MPs) and 950μL of supernatants were collected. The particles were then mixed with 950 μL of fresh PBS. The collected supernatants were then flash frozen, and lyophilized overnight. The lyophilized powders were then mixed with 200 μL of 1:4 (v/v) acetone:DMSO solution and were briefly centrifuged (quickspin) to pellet the undissolved salts. 100 μL of the solution was then used to measure the fluorescence intensity. Calibration curve of acriflavine in acetone:DMSO and PCL mixture was then used to quantify the mass and subsequently the release amount (%) of acriflavine.

2.2.10. Quantifying the effect of PCL molecular weight on cargo release time

To determine the effect of PCL molecular weight on the release time of cargo, PCL solutions of varying molecular weight (14 kDa and 45 kDa) were used to prepare polybubbles, and the release time was quantified using BSA-CF488 fluorescent dye as cargo. Both 14 kDa and 45 kDa of PCL were dissolved in separate solutions of chloroform at a concentration of 800 mg/mL. Both PCL solutions were then mixed with PCLTA in a 1:3 (v/v) (PCL/PCLTA). 1 μL of photoinitiator was added (0.05% final concentration) to each batch of PCL/PCLTA. Subsequently, each polymer mixture was loaded into separate 250 μL glass barrels and dispensed using the syringe pump at a rate of 0.5 μL/sec for 10 seconds.

To prepare the polybubble cargo, 250 μL of PBS were added to a stock of BSA-CF488 for a final concentration of 4 mg/mL. 12.5 mg of CMC was added to this cargo solution, so that a 5% (w/v) CMC BSA-CF488 cargo solution was prepared. This cargo solution was injected into each polybubble using a 34 G needle, and the polybubble was cured under UV light for 10 minutes. The polybubbles were frozen in liquid nitrogen for 2 minutes and lyophilized overnight. After lyophilizing, the polybubbles were washed and soaked in 500 μL of PBS. The PBS solution was collected and the fluorescence intensity was analyzed every 2 days.

2.2.11. Quantifying the effect of polybubble shell thickness on cargo release time

To determine the effect of polybubble shell thickness on the cargo release time, PCL/PCLTA polymer mixture was first prepared by dissolving 45 kDa PCL in chloroform at a concentration of 800 mg/mL. This PCL solution was mixed with PCLTA in a 1:3 PCL/PCLTA (v/v) ratio to enable curing. 1 μL (0.05% final concentration) of the photoinitiator was added to the polymer mixture. The polymer mixture was then loaded into a 250 μL glass barrel and dispensed using the syringe pump at a rate of 0.5 μL/sec for 10 seconds.

To vary the shell thickness, different volumes of cargo were injected into the PCL/PCLTA polybubbles as described above. Polybubble cargo was prepared by first adding 250 µL of PBS to BSA-CF488 stock for a concentration of 4 mg/mL. 12.5 mg of CMC was added to this cargo solution, so that a 5% (w/v) CMC BSA-CF488 cargo solution was obtained.

Next, before injecting cargo, the polybubbles were first divided into two groups based on the volume of the cargo to be injected. Injecting a smaller cargo volume yields a thicker polybubble shell, while injecting a larger cargo volume yields a thinner polybubble shell. The smaller cargo volume was injected using the syringe pump at a rate of 0.5 µL/sec for 2 seconds, yielding a total cargo volume of 1 µL. The larger cargo volume was injected using the syringe pump at the same rate for 5 seconds, yielding a total cargo volume of 2.5 µL. All polybubbles were then cured under UV light for 10 minutes. After confirming the polybubbles had cured using the same method described previously, the polybubbles were frozen in liquid nitrogen for 2 minutes and lyophilized overnight. After lyophilization, the polybubbles were washed and soaked in 500 µL of PBS. The PBS solution was collected and the fluorescence intensity was analyzed every 2 days.

2.2.12. Enzyme-linked immunosorbent assay protocols

HIV1 gp120/41 antigen was diluted in a coating buffer at 1.25 µg/mL and loaded onto a 96-well plate. Serial dilution of half concentration was performed so that each well contained 50 µL of antigen solution. The plate was incubated for 2 hours at room temperature on a plate shaker at 400 RPM. After incubation, the plate was washed three times using 300 µL PBS for 5 minutes on a plate shaker at 400 RPM. 300 µL of 5% (w/v) nonfat dry milk solution was loaded and incubated overnight at 4 °C to prevent non-specific antibody binding. The blocking solution was washed twice with the same methods as antigen washing. The anti-HIV1 gp120/41 antibody-horseradish peroxidase (HRP) conjugates were diluted at 1:800 and loaded at a volume of 100 µL. After 2 hours of incubation at room temperature, the plate was washed three times with the same methods as antigen washing. 100 µL of tetramethylbenzidine solution was loaded and incubated for 15 minutes at room temperature, and the plate was covered with foil. 100 µL of stop solution was added, and the absorbance was read 10 minutes later at 450 nm.

2.2.13. Quantifying antigen stability

In order to quantify the more optimal concentrations of trehalose, 0.5 M of trehalose solution was prepared by adding 0.1797 g of trehalose to 1050 µL of coating buffer. Six different concentrations of trehalose solutions were prepared from $5x10^{-1}$ M to $5x10^{-6}$ M solution using 10x serial dilutions. 10 µg/mL of HIV-1 gp120/41 antigen solutions were prepared by diluting the antigen stock using various trehalose solutions. Antigen solutions were placed at 37 °C oven after aliquoting. The functionality of HIV-1 gp120/41 antigen was analyzed on day 4 using ELISA.

The HIV1 gp120/41 antigen was diluted in coating buffer at 80 µg/mL. The antigen solution was aliquoted into nine microtubes of equal volume. Microtubes were placed in the following temperature conditions: 4 °C, room temperature, and 37 °C. Antigen samples were collected and frozen on days 4, 7, 14. After collecting samples until day 21, the functionality of every antigen sample was analyzed by an enzyme-linked immunosorbent assay (ELISA).

80 μg/mL of 625 μL of antigen solution was prepared by diluting antigen stock using coating buffer. 17.11 g of trehalose was added to the antigen solutions for creating a 0.5 mM trehalose solution. The antigen within the trehalose solution was aliquoted to 36 microtubes and lyophilized overnight. Microtubes were placed at 4 °C, room temperature, and at 37 °C. Antigen samples were collected and frozen on days 4, 7, 14 and 21. After collecting day 21 samples, the functionality remaining of the antigens with varying conditions were analyzed by ELISA.

2.2.14. Quantifying antigen stability within the polybubbles

First, 400 μL of 45 kDa PCL (500 mg/mL) were combined with 1.2 mL of PCLTA. The mixture was rotated in the 60 °C oven. The antigen was diluted to 100 mg/mL in coating buffer. HIV1 gp120/41 (0.1% (w/v)) and trehalose (0.5 mM) were added to the antigen. The mixture was rotated after 0.05 g CMC was added.

The polybubbles were formed in a 10% CMC reservoir using the syringe pump, and antigen was injected. The polybubbles were cured for 10 minutes under UV light and lyophilized overnight. Lyophilized polybubbles were incubated in a 37 °C oven and opened on day 3, 7, and 11. The antigen was dissolved in the coating buffer; both fluorescence and functionality were quantified.

2.2.15. Statistics

In order to quantify the statistical significances for Figures 5b and 5c we used a standard Student's t-test, with an α set at 0.05; a p-value <0.05, 0.01, and 0.001 are denoted as *, **, and ***, respectively. The error bars for Figure 8 indicate the 95% confidence interval. The solid and dotted lines that appear in Figure 8 are 95% confidence intervals.

2.3. Results

2.3.1. Physical assessment of 80 kDa PCL polybubbles

The concentration of the PCL polybubbles was varied from 100 mg/mL to 1000 mg/mL. Polybubbles with PCL concentrations ranging from 100 mg/mL to 400 mg/mL were hollow. Consequently, these polybubbles easily collapsed under the pressure of forceps after removal from the solution. In contrast, polybubbles with PCL concentrations ranging from 600 mg/mL to 1000 mg/mL were rigid enough to withstand forceps' pressure (**Figure 2.2c**). However, most of these polybubbles easily cracked during the lyophilization process (**Figure 2.2d**).

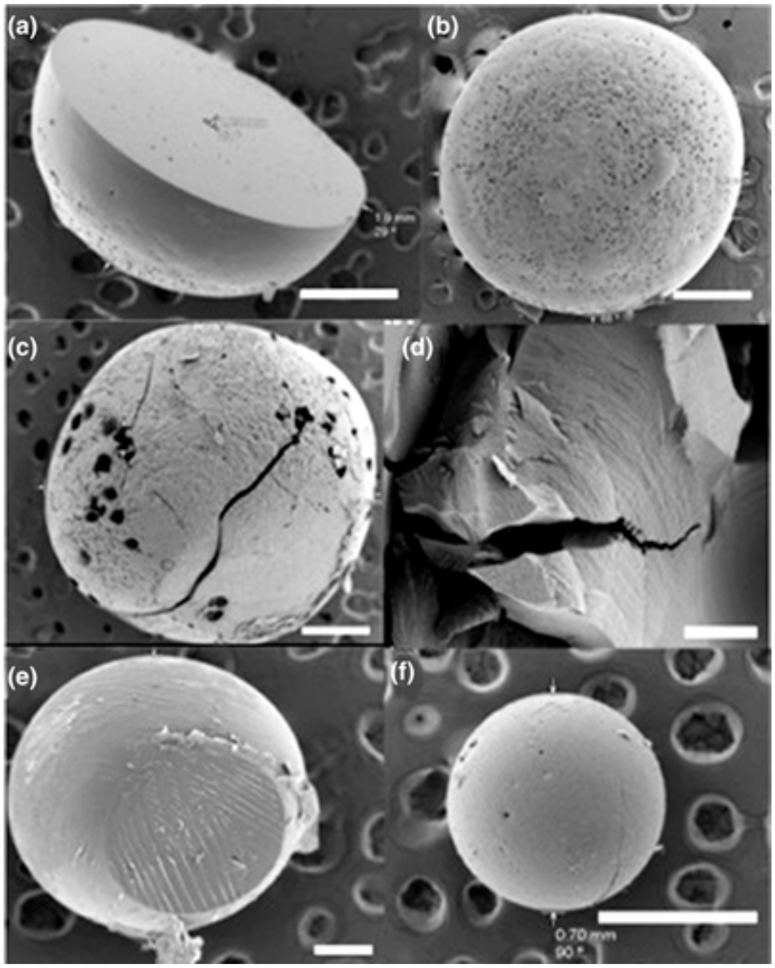

Figure 2.2 Polybubble Characterization: SEM images of (a) 14 kDa PCL/300 Da PCLTA polybubble that was in contact with the bottom of the glass vial; (b) flattened 14 kDa PCL/300 Da PCLTA polybubble from the top; (c) surface of 1000 mg/mL of 80 kDa PCL polybubble; (d) inside of 1000 mg/mL of 80 kDa PCL polybubble;
(e) PCL/PCLTA polybubbles that reached the bottom of the glass vial when injected into a 5% CMC solution, causing the formation of hemisphere-like shape at the point of contact with the vial; (f) polybubble that did not reach the bottom of the glass vial when injected into a 10% CMC solution, allowing for the spherical shape to be maintained. All of the scale bars indicated are 500 µm except for (d), which is 200 µm. Reprinted with permission from John Wiley and Sons from Lee *et al.* [123]

2.3.2. Shape comparison of PCL and PCL/PCLTA polybubbles

The main difference between the PCL polybubbles and blended PCL/PCLTA polybubbles was the shape they formed following polymer injection. While the PCL polybubbles remained spherical in shape even after sinking to the bottom of the vial, the PCL/PCLTA polybubbles formed a hemisphere-like shape after coming into contact with the bottom of the glass vial. As a result of this shape change, as shown in **Figures 2.2a** and **e**, the diameter of the PCL/PCLTA polybubbles increased from 0.70 mm (**Figure 2.2f**) to 1.90 mm (**Figure 2.2a and 2.2b**), as quantified using ImageJ.

Furthermore, SEM images of the polybubbles were taken to assess surface morphology. Despite the changes in diameter noted above, SEM indicated that the surface did not contain noticeable defects (**Figure 2.2f**).

2.3.3. Optimization of PCL/PCLTA polybubble UV curing time

A 0:1 PCL/PCLTA ratio could not be punctured using pipette tips. In contrast, polybubbles with a 1:0 PCL/PCLTA ratio were not cured at all, and the soft surface of the polybubbles could easily be deformed with a pipette tip.

To determine how long the PCL/PLCTA polybubbles should be cured, the qualitative rigidity test was applied again. After polybubbles were cured for 5 minutes, the qualitative rigidity assessment indicated that only the surface of the polymer was cured, and the polybubbles were easily broken as a result. After the polybubbles were cured for 10 minutes, the qualitative rigidity assessment indicated that all of the polymer had cured, and it was difficult to puncture the surface using pipette tips. Therefore, a UV curing process was used for 10 minutes on every polybubble to standardize polybubble rigidity.

2.3.4. Quantification of Chlorine Content in the Polybubbles

The chlorine content in the polybubble was found to increase over time and reached an asymptote value near 6 hours of 1.92 ± 0.03% (95% confidence interval) (**Figure 2.3a**). The chlorine content in the supernatants from the release studies was found to be ~ 0.5% (wt%) (**Figure 2.3b**).

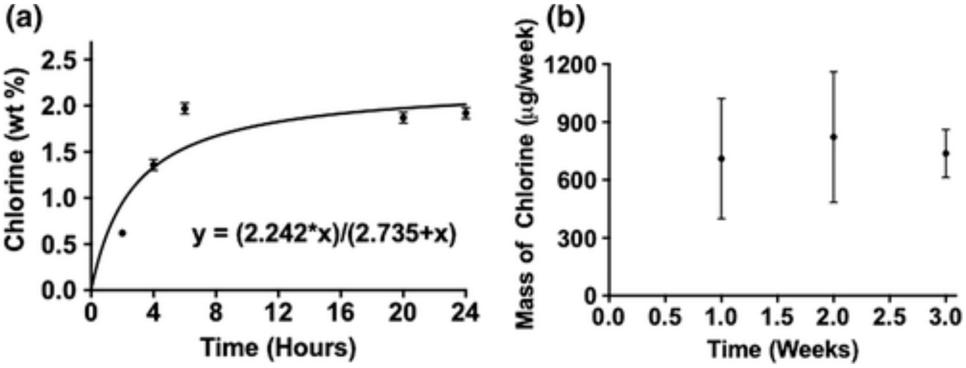

Figure 2.3 Quantification of Chlorine Content within the Polybubble. a) Mass fraction of chlorine was measured using NAA with varying lyophilization time of the polybubbles (2 hours, 4 hours, 6 hours, 20 hours (approximately the time lyophilized for our samples), and 24 hours). The R^2 value of the fitted curve is 0.7633. b) Mass of chlorine in supernatants from release studies were analyzed using NAA (the contribution of chlorine from PBS was subtracted). Reprinted with permission from John Wiley and Sons from Lee *et al.* [123]

2.3.5. Localization of polybubbles using PEGDA hydrogels, HEMA /TEGDA /PEGMA hydrogels, HEMA/CMC hydrogels, trehalose, and agarose gel

In order to keep the polybubbles in a fixed position during both the polymer and drug injection process, polyethylene glycol diacrylate (PEGDA) hydrogels, HEMA/TEGDA hydrogels, HEMA/CMC hydrogels, trehalose, agarose, and CMC were tested as potential solution reservoirs.

When PEGDA hydrogels were used as solution reservoirs, polybubbles could not be formed successfully (**Figure S5a-b)**. Moreover, the injected polybubble could not be visualized within the HEMA/TEGDA hydrogel matrix when 100 μL and 200 μL of water were used because the matrix was too rigid to inject into (**Figure S5b**). Additionally, when the HEMA/TEGDA hydrogel contained more than 400 μL of water, the solution became cloudier, making it even more difficult to visualize the polybubble.

HEMA hydrogels were also tested independently as potential solution reservoirs following UV curing. The HEMA hydrogels cured from the bottom of the glass vial to the top, making it possible to inject the polymer into the UV-cured, a lower portion of the HEMA hydrogel solution before the entire volume of gel in the vial had fully cured. Even after UV curing the HEMA hydrogel, however, the polybubble surface became flat after coming into contact with the HEMA, similar to the shape change that occurred when the polybubble came into contact with the glass vial (**Figure S5c**). To increase the viscosity of the HEMA hydrogels, 5% (w/v) CMC was also mixed prior to UV curing. However, the solution became cloudy following UV curing (and became increasingly so with the addition of water), making it difficult to visualize the polybubbles post-injection (**Figure S5d**).

Trehalose was also studied as a potential solution reservoir. While the literature indicates that trehalose has a higher viscosity than water, the polybubbles still sank to the bottom of the vial when a 60% (w/v) trehalose solution was used, just as the polybubbles injected into DI water did. As a result, the polybubbles injected into the trehalose solution became hemispherical in shape (**Figure S5e**).

In addition to trehalose, agarose gel was also tested as a potential solution reservoir. Polybubbles injected into the agarose gel solution appeared closer in shape to a sphere than other solutions, such as HEMA, PEG, and trehalose; however, the surface of polybubbles coming into contact with the agarose gel was more flat than other parts of the surface (**Figure S5f**).

2.3.6. Localization of polybubbles using CMC

Among the various solvents tested, the CMC solutions had the highest viscosity (qualitative assessment; however, based on literature [34, 35] the 0, 5% and 10% CMC viscosity values were approximately 0.89 mPa, 11.5 kPa, and 4.87 MPa, respectively). In a 5% (w/v) CMC solution, the polybubbles sank slowly. After UV curing, the polybubbles eventually reached the bottom of the glass vial, resulting in a slightly flattened hemisphere-like shape (**Figure 2.2e**). However, in a 10% (w/v) CMC solution, the polybubbles were completely suspended. Even after UV curing, the polybubbles remained suspended in the CMC solution, in addition to maintaining their spherical shape (**Figures S5g, 2.2f**).

Figure S7 shows polybubbles that have been identified within lyophilized 10% CMC and extracted. **Figure S8** shows SEM images of polybubbles that have CMC on their external surface (top; 5% CMC) and also with the CMC absent (bottom; 10% CMC). The CMC readily falls off of the UV cured polybubbles.

2.3.7. Cargo injection in the presence and absence of CMC

When the cargo was prepared without CMC, the cargo escaped immediately following injection, as shown in **Figure S6**. Confocal microscopy confirmed the migration of cargo in the absence of CMC by indicating the presence of fluorescent dye on the polybubble's surface, rather than within the polybubble itself (**Figure 2.4a**). The approximate amount of drug that is in the core versus the shell is 71 ± 7%.

When the cargo was mixed with 5% (w/v) CMC, the inner cargo bubbles migrated comparatively slower than the cargo bubbles prepared without CMC (**Figure 2.4c-e**). Time-lapse photography taken of the cargo bubbles following injection demonstrated that the cargo prepared with 5% (w/v) CMC migrated upwards with an average velocity of 92.3 μm/sec, as quantified via ImageJ (**Figure S10**). Immediate UV curing was shown to halt the migration of cargo prepared using 5% (w/v) CMC.

In contrast, cargo prepared without CMC escaped from the bubble immediately following injection. It is important to note, however, that even in the case of cargo prepared using 5% (w/v) CMC, cargo still escaped following injection (refer to **Figure 2.5**). Furthermore, the distance between the cargo and the polybubble surface was estimated to be 10 μm given that the two concentric rings in the center (**Figure 2.4e;** refer to the available movie – please note that the z-stack (420 μm) is limited to a portion of the polybubble given that confocal microscopy cannot scan through the entire width of the polybubbles of interest) belong to the cargo space.

Similar to the cargo prepared with 5% (w/v) CMC, polybubbles injected with cargo mixed with 3% (w/v) CMC also slowed the migration of cargo bubbles; however, this 3% (w/v) CMC cargo continued to rise to the top of the polybubbles and eventually migrated through the polybubbles' shell, even after immediate UV curing **(Figures 2.4b, S9)**

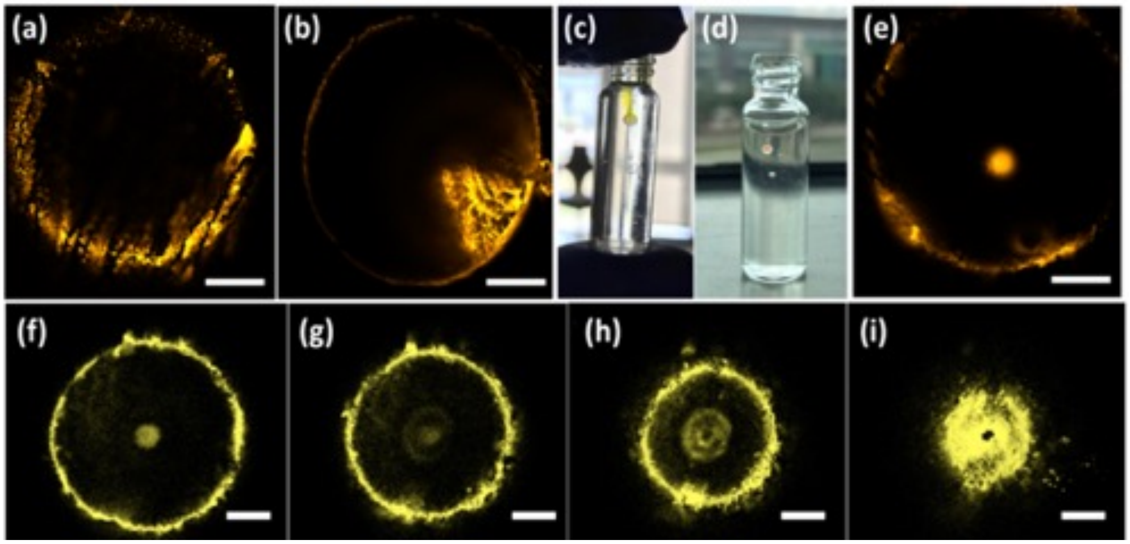

Figure 2.4 Cargo Localization within the Polybubble: Confocal images taken after UV curing and lyophilization using (a) 1% (w/v) acriflavine without CMC, (b) 1% (w/v) acriflavine with 3% (w/v) CMC, and (e) 1% (w/v) acriflavine with 5% (w/v) CMC. Images were also taken of the cargo prepared with 5% (w/v) CMC using (c) 1% (w/v) acriflavine and (d) 1% (w/v) doxorubicin. Confocal images of BSA-CF488 prepared with 5% (w/v) CMC were taken in the polybubble from the middle to the bottom of the polybubble, as shown in (f) to (i). The distance between each slice is 10 μm. Note that there is drug around the periphery, which is due to the escape of the drug through the temporary conduit made as the tube used for the cargo injection is removed from the liquid shell of the polybubble. Scale bar: 500 μm. Reprinted with permission from John Wiley and Sons from Lee *et al.* [123]

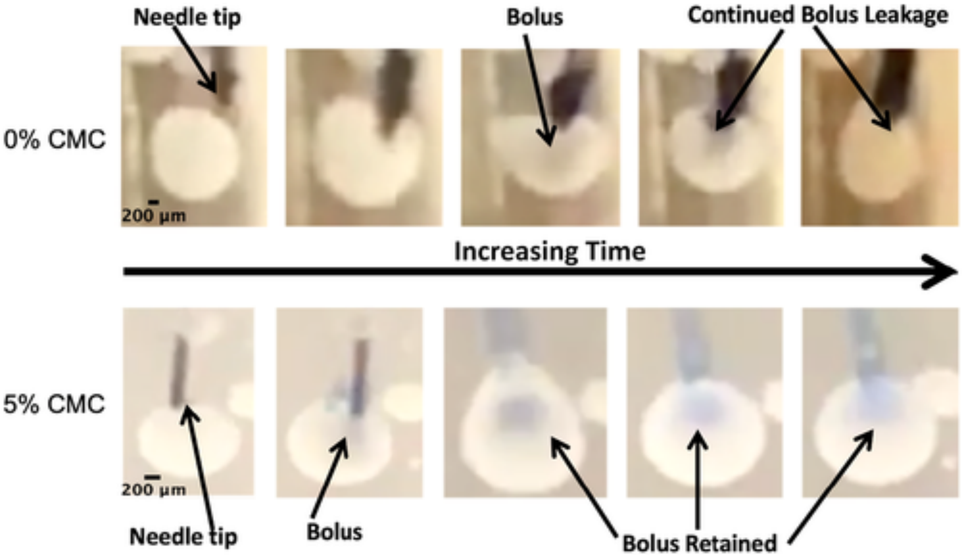

Figure 2.5 Time-lapse images taken before and after injection of both 0% and 5% CMC-containing cargo. As shown in the bottom row of images, the majority of cargo (dye partially obscured by polybubbles shell) prepared with 5% CMC is retained within the polybubbles after removal of the needle tip. However, as shown in the top row of images, cargo prepared without CMC leaks out of the polybubbles following needle removal. Note also that these polybubbles are more opaque due to the polymer at the interface with water; initially, the polybubbles is more transparent. Reprinted with permission from John Wiley and Sons from Lee *et al.* [123]

2.3.8. Polybubble diameter as a function of syringe pump rate, lyophilization and cargo presence

In regards to the syringe pump rate, as can be seen from **Figure 2.5a**, the polybubble size increased from 325 ± 20 µm to 799 ± 71 µm when the syringe pump rate increased from 0.005 µL/sec to 1 µL/sec while the micromotor was driven backwards at the constant rate set by the manufacturer. Moreover, between 0.005 µL/sec and 0.01 µL/sec, the polybubble diameter increased from 325 ± 20 µm to 547 ± 23 µm. It is important to note that, when the polybubbles were formed at a rate of 0.1 µL/sec for 5 seconds, the volume should be 0.5 μL. However, the actual volume was less than that, and was quantified to be ~6% less.

Regardless of whether the polybubbles contained cargo, the polybubbles were shown to decrease in diameter post-lyophilization. The diameter decreased by 25 ± 3% and 31 ± 3% for polybubbles without cargo and with cargo, respectively (**Figure 2.6b**).

The diameter of the polybubbles was analyzed pre- and post-lyophilization using a Student's t-test. The quantified p-values were 0.0014 and 0.0009 for polybubbles without and with cargo, respectively. Both values were less than 0.05, indicating statistically significant differences in diameter pre- and post-lyophilization.

When the diameters of the polybubbles before cargo injection were normalized to 1.000 ± 0.064, the post-injection diameter was calculated to be 1.084 ± 0.069 (**Figure 2.6c**). Although the polybubble volume increased by 8.4%, the size difference is not significant since the p-value was calculated to be 0.199.

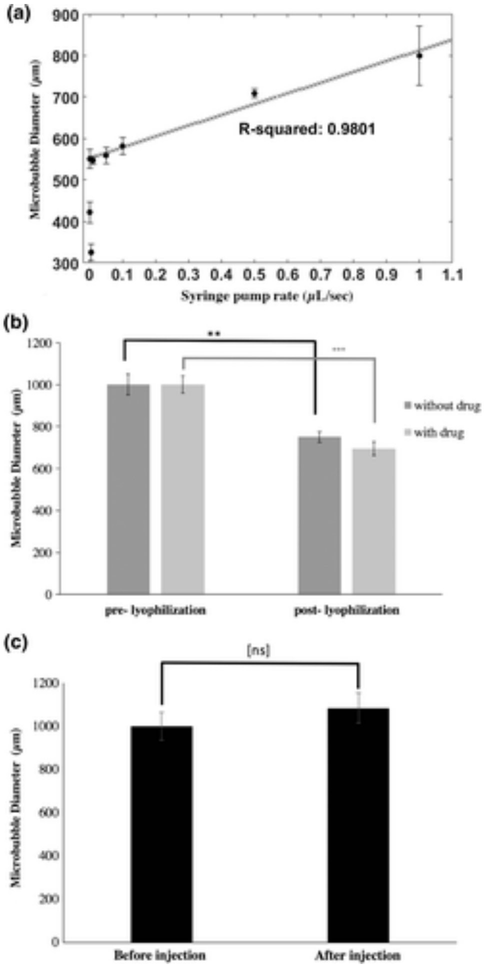

Figure 2.6 Polybubble Size Quantification: (a) The effect of syringe pump rate on polybubble diameter as the micromotors were driven backwards in space. The backwards motion of the micromotor causes polybubbles to separate. (b) Comparison of polybubble size before and after lyophilization, both with and without cargo. (c) Comparison of polybubble diameter before and after cargo injection. Reprinted with permission from John Wiley and Sons from Lee *et al.* [123]

2.3.9. Quantifying the effect of moisture content on the thermal behavior of the polybubbles

DSC curves of the cured PCL/PCLTA polybbubles with and without lyophilization had a broader T_m peak compared to that of the cured and lyophilized

PCL/PCLTA (**Figure 2.7a-c**). The T_m of the DSC curves of each group is indicated by a vertical line.

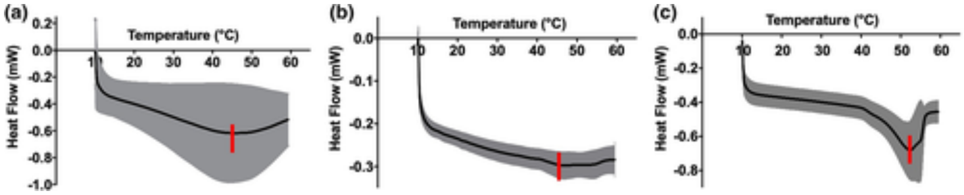

Figure 2.7 Effect of moisture on Tm: DSC curves of a) cured and lyophilized PCL/PCLTA polybubbles injected with drug mixed with 5% CMC, b) cured and non-lyophilized PCL/PCLTA polybubbles injected with drug mixed with 5% CMC, c) cured and lyophilized PCL/PCLTA polymer in a non-polybubble form. Tm peaks are indicated as dark vertical lines. Reprinted with permission from John Wiley and Sons from Lee *et al.* [123]

2.3.10. Effect of emulsion-based MPs and NPs on cargo release

Release profiles of MPs and NPs indicate that there is an initial burst release on day 1 and sustained release after day 1. The delayed burst that is observed with polybubbles is thus novel compared to that of emulsion-based MPs and NPs.

2.3.11. Effect of PCL molecular weight on cargo release time

14 kDa PCL/PCLTA polybubbles resulted in two separate bolus releases occurring immediately and during days 10-14 (**Figure 2.8a**). The cargo released in the initial bolus was present in the outer 10% CMC solution and was also partially absorbed into the shell of the polybubble, according to confocal microscopy (**Figure 2.4e**). The secondary bolus released during days 10-14 resulted from the release of the internal cargo.

Similar to the 14 kDa PCL/PCLTA polybubbles, the 45 kDa PCL/PCLTA polybubbles also demonstrated an immediate bolus release for the same aforementioned reasons

(**Figure 2.8a**). The second bolus release from the 45 kDa PCL/PCLTA polybubbles occurred on days 16-20, which was later than the second bolus release quantified for the 14 kDa PCL/PCLTA polybubbles (**Figure 2.7a**)

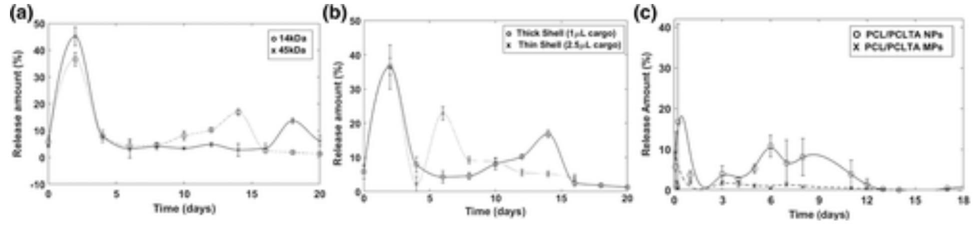

Figure 2.8 Release Profiles from the Antigen in the Polybubble: (a) Release Profile from 14 kDa and 45 kDa PCL/PCLTA. (b) Release Profile from PCL/PCLTA polybubbles with varying shell thicknesses. (c) Release Profile from PCL/PCLTA MPs and NPs. Reprinted with permission from John Wiley and Sons from Lee et al. [123]

2.3.12. Antigen functionality and stability

To prevent non-specific binding, the following blocking buffers were tested: BSA solutions of 1%, 3%, and 5%, nonfat dry milk solutions of 1%, 3%, and 5%, and casein. Ultimately, the ELISA protocol was finalized using 5% nonfat dry milk as the blocking buffer.

When casein, BSA, and low concentrations (1% and 3%) of nonfat dry milk solutions were used as the blocking buffer, the blank wells containing PBS indicated high background, regardless of the blocking buffer incubation time. Moreover, there was no significant difference in the reduction of the background when 5% (w/v) nonfat dry milk solution was used to block for two hours at room temperature and overnight at 4°C.
Within the range of HIV1 gp120/41 antibody dilutions from 1:200 to 1:1000, dilutions of 1:800 were sufficient to decrease the excessively high background, allowing for a

calibration curve to be generated. Absorbance demonstrated a linear trend between 2 and 10 µg/mL of antigen concentrations (**Figure S12**).

2.3.13. Antigen stability within the polybubbles

HIV1 gp120/41 antigen samples without trehalose were collected and analyzed for 14 days using ELISA. The results demonstrate that HIV1 gp120/41 underwent a loss of functionality as time progressed (**Figure 2.9**). After 2 weeks, the functionality of HIV1 gp120/41 was reduced by approximately 55% at 37°C. There was no difference in the drop of percent functionality with and without trehalose in time based on the 95% confidence intervals.

Polybubbles containing antigen with trehalose were opened on days 3, 7, and 11, and the antigen within the polybubble was checked for fluorescence. Similar to the quantified antigen stability without trehalose, the functionality of antigen with 0.5 mM trehalose within the polybubble was reduced by approximately 45% at 37°C after 2 weeks (**Figure 2.9**).

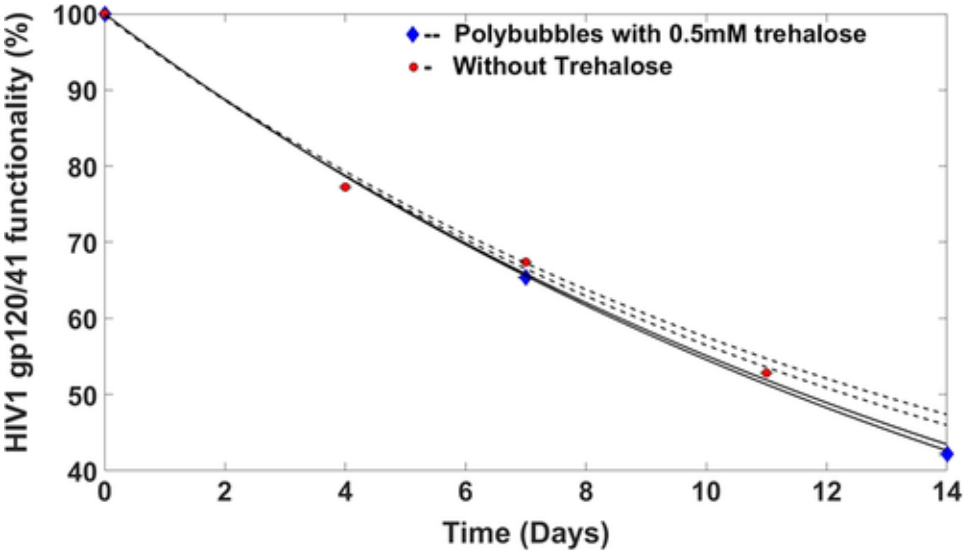

Figure 2.9 Antigen Functionality: Functionality of HIV1 gp120/41 antigen within the polybubble at 37°C, measured without trehalose and with 0.5 mM trehalose. The dotted and solid lines are the 95% confidence intervals. Reprinted with permission from John Wiley and Sons from Lee *et al.* [123]

2.4. Discussion

2.4.1. Polybubble Formation

One of the major limitations in developing polymeric micro- and nanoparticle systems for amino acid-based cargo delivery results from the formation process. Emulsion-based techniques, which are commonly used for fabricating micro- and nanoparticle, expose cargo to both organic and aqueous solvents [36, 37]. In the case of amino acid-based cargo, solvent exposure can lead to protein aggregation and denaturation, resulting in reduced therapeutic efficacy [13, 38]. To address the need for reduced solvent exposure, alternative fabrication methods, such as the StampEd Assembly of polymer Layers (SEAL) technique, have been developed [39]. The SEAL technique injects the drug into fillable polymer bases, which are then aligned and sealed with polymer caps under heat [39]. However, the SEAL process is associated with a high failure rate during the cap-alignment process, as well as the junction between the cap and the base. Our polybubble formation method overcomes the limitations with emulsion-based systems and multi-polymer phase particles by minimizing the surface area of the cargo in contact with an organic solvent while also removing the need for a cap entirely.

Polybubbles were formed using PCL and PCLTA in a 1:3 (v/v). PCLTA was used to allow for UV curing of the polybubbles. Additionally, the PCL/PCLTA mixture was used in order to demonstrate that the release kinetics of the system can be varied, despite the potential issues of phase separation. Polybubbles were formed by injecting the organic-phase PCL/PCLTA mixture into an aqueous phase. In order to prevent the polybubbles from sinking to the bottom of the glass vial during the injection process, the polybubbles were injected into a range of potential reservoirs, including PEGDA hydrogels, HEMA/TEGDA hydrogels, HEMA/CMC hydrogels, trehalose, agarose gel, and CMC. Ultimately, 10% (w/v) CMC was chosen as the reservoir solution, as it enabled the polybubbles to be suspended in the solution, thereby preserving the sphericity of the polybubbless both before and after the curing process.

In order to optimize polybubble cargo positioning, potential cargo formulations were investigated. First, cargo in the aqueous phase without CMC was injected in the middle of the polybubble. However, confocal microscopy indicated that the cargo preferentially partitioned into the organic phase, as opposed to the aqueous phase, as shown in **Figure 2.4b**.

Consequently, a significant gap between the time of cargo injection and UV curing could cause the migration of cargo into the organic phase, thereby escaping from the polybubble. In contrast, when 5% (w/v) CMC was mixed with the cargo, the increased viscosity of the inner cargo bubble reduced the rate of cargo migration during both the UV curing and lyophilization processes, as demonstrated in **Figure 2.4e**. However, by the end of the curing process, the cargo was still not successfully centered. Cargo most likely migrated upwards during the curing process and localized closer to the surface of the polybubble.

The observed reduction in polybubble diameter following lyophilization is likely due to the evaporation of water from cargo and chloroform from the polymer phase. However, we suspect that there is water still being retained along with the cargo in the middle, as the cargo space is not vented to the vacuum and water is not able to transport through the organic solvent phase or the dry polymer shell.

2.4.2. Residual Chlorine

Residual chlorine was found to be present at 1.92 ± 0.03% (**Figure 2.3a**). The chlorine wt % seems to increase with increasing lyophilization time. At earlier time points, the chlorine content is likely lower than it is at 6 hours and beyond owing to the increased mass of the polybubble compared to after lyophilization. Although chloroform and water are considered immiscible, chloroform solubility according to literature ranges from 0.089% to 0.81% (chloroform in water versus water in chloroform) near room temperature. The slight solubility is the basis of emulsion-based techniques to form polymer nano- and microcapsules. This solubility as a cause of concern was eliminated after the diameters of uncured polybubbles were tracked in time in the presence of excess 10% (w/v) CMC. There was no statistical significance in the change in diameter (**Figure S3**).

NAA was also carried out on supernatants from the release studies. The chlorine wt % in the supernatants of ~0.5% (**Figure 2.3b**) would result in approximately 776 µg per week or 110 µg per day (1.5 µg/kg/day (for a 70 kg patient)). This is well within the acceptable range of below 85-310 µg/kg/day (oral dose of 100-360 µg/kg/day with a bioavailability reported to be approximately 85%). However, local concentrations of chlorine and the resulting cytotoxicity need to be determined *in vivo* in future studies [40, 41].

2.4.3. Moisture Content in the polybubbles

T_m peaks varied between three groups (cured PCL/PCLTA polybubbles that were lyophilized, cured PCL/PCLTA polybubbles that were not lyophilized, and cured and lyophilized PCL/PCLTA in a non-polybubble form) (**Figure 2.6a-c**). This difference is likely due to incomplete lyophilization within the polybubbles. Moisture is likely trapped in the core of the polybubble due to lack of venting passage. As the solvent is removed, the polybubble is likely hardened thus trapping the moisture in the center. Increased moisture content likely caused the T_m peaks of the lyophilized and non-lyophilized polybubbles to be different from that of the distinct T_m peak of the lyophilized polymer in the non-polybubble form. Based on this trend, emulsion-based particles are more likely to have moisture trapped within the particles. However, polybubbles are likely to have less moisture content because the surface area of cargo exposed to solvent is considerably less in the polybubble system when compared to other emulsion-based techniques.

2.4.4. Release Studies

Both the 14 kDa and 45 kDa PCL/PCLTA polybubbles exhibited an immediate bolus release, suggesting that delivery of the first bolus is independent of polybubble molecular weight (**Figure 2.7a**). This first bolus release is likely due to the presence of the drug on the outer surface of the polybubble, resulting from the cargo's propensity to partition into the organic phase, rather than the aqueous phase, during the injection process. This portioning likely occurs while the tube used for the injection process is retracted out of the polymer shell. Of note, the release of the drug occurring at an earlier-than-expected timepoint highlights issues associated with centering the cargo in the middle of the polybubble. The shell itself is not uniform around the cargo space.

Moreover, both the 14 kDa and 45 kDa PCL/PCLTA polybubbles were shown to exhibit secondary boluses (**Figure 2.7a**). The 45 kDa PCL/PCLTA polybubbles demonstrated a later secondary release compared to the 14 kDa polybubbles; this is likely because higher molecular weight polymers have longer chains, and thus can entrap the cargo for longer time periods, compared to lower molecular weight polymers with less chain entanglement.

Regardless of the shell thickness level, PCL/PCLTA polybubbles exhibited an immediate bolus release, which occurred for the same reason as the initial bolus release from the polybubbles with differing molecular weights (**Figure 2.7b**). In addition to the initial bolus release, both the thin-shell and the thick-shell polybubbles demonstrated secondary releases on day 14 and day 16, respectively (**Figure 2.7b**). Because the thick-shell polybubbles require more time for the shell to degrade, they can entrap the cargo longer than thin-shell polybubbles, thus causing the second bolus to be delivered at a later time point.

Release profiles of MPs and NPs indicate that there is an initial burst release on day 1 followed by sustained release (**Figure 2.7c**). Cargo encapsulation in emulsion-based MPs and NPs results in multiple cargo pockets resulting in a sustained release. In contrast, cargo is localized to one pocket in the polybubble system resulting in a distinct delayed burst release.

2.4.5. Antigen Functionality within the Polybubble

Antigen functionality was tested in both the presence and absence of trehalose. Sugars such as trehalose are known to minimize protein denaturation and promote stability [42]. In the absence of trehalose, the antigen functionality dropped to ~42% after 14 days. Based on **Figure S13,** we concluded that 0.5 mM trehalose would be optimal to use within the polybubble, as only a few functionality percentages would likely be lost after 4 days. However, we observed that the polybubbles' internal antigen functionality with 0.5 mM trehalose was not statistically different than that of the antigen without trehalose. It is not surprising that there was not a difference with and without trehalose because this was unoptimized within the polybubble and no other excipients were used. Instead, this study demonstrates the feasibility for future use of a cryoprotectant during polybubble formation.

2.4.6. Manual vs Automation

The polybubble diameter was shown to be unreliable when the syringe pump rate was programmed below 0.005 μL/sec. The inaccuracy at this stage is likely due to the lower limit of the syringe pump, which is 0.0003 μL/sec. The polybubble diameter increased from 325 ± 20 μm to 551 ± 23 μm when the syringe pump rate decreased from 0.005 μL/sec to 0.001 μL/sec in two separate experiments (**Figure 2.5a, S4**). Moreover, because the syringe pump operation was performed manually, there was 5.4% error between the theoretical and actual volumes.

2.5. Conclusions

In this study, a novel PCL-based polybubble platform was shown to provide bolus delivery of cargo. In an effort to minimize exposure to organic solvent and ensure cargo stability, the cargo was manually injected into the polybubble. Although cargo could not be centered within the polybubble, cargo mixed with 5% (w/v) CMC was shown to successfully slow down the rate of the internal cargo migration. We will quantify the velocity of the internal cargo migration in a more methodical manner in the future.

Cargo centering is critical to ensuring a uniform delayed-burst release profile. For this reason, future studies will include modifying the viscosity of the cargo to investigate cargo centering and to ensure the thickness of the polymer shell is uniform around the cargo bubble. Moreover, further studies will also focus on minimizing polybubble diameter as a way of (1) optimizing treatment delivery and (2) reducing patient pain experienced during administration. In addition, the effects of trehalose on the functionality of HIV1 gp120/41 antigen will also be methodically and thoroughly examined in future studies with rigorous statistics. We hypothesize that there was an affinity for the trehalose with either the syringe pump, the tubing of the syringe pump, or the metal tubing used to inject the polybubble's cargo, causing trehalose to be extracted from the solution. With that in mind, we believe that our polybubble did not cause a significant decrease in antigen functionality over the nearly two-week time period in which functionality was quantified, which is encouraging. Thorough optimization of antigen protection within the polybubble is forthcoming.

Both the release profile and functionality of the antigen cargo over time demonstrate proof-of-concept. As we continue to develop our technology, we will address the following goals: (1) design a system to vent the polybubble's cargo during lyophilization as a way to better control the water content within the polybubble; (2) integrate an automated lyophilization system with the polybubble injection process, allowing for a seamless transition between the injection and lyophilization states (**Figure S14**); and (3) incorporate imaging agents within the polybubbles and methods to modulate the release kinetics extracorporeally.

While microfluidics approaches have been used for successfully fabrication of two-phase systems [24, 25], we opted to not use a microfluidic approach initially for the proof-of-concept because: (1) generally the size of phase-separated particles used within such systems range from 0.01-200 μm [43-46], which would likely require many dozens of the same particles to be delivered, potentially leading to self-aggregation and undesirable and unpredictable kinetics; (2) the amount of drug in contact with an organic solvent is far higher (**Figure S1**), which would increase the cost of the system due to cargo denaturation issues; and (3) the diameter of microfluidic-formed approaches generally result in more of a continuous release fashion, which may result in T-cell anergy. In the future, we plan to investigate (macro)fluidic approaches, as opposed to microfluidics. The goal of using a macrofluidic approach is to reach vaccination-relevant time points and decrease the total surface area of organic solvent a vaccine dose would come into contact with, as compared against an injection array platform based on this work.

3. NANOENGINEERED LIGHT-ACTIVATABLE POLYBUBBLES FOR ON-DEMAND THERAPEUTIC DELIVERY*[3]

3.1. Introduction

Infectious diseases results in approximately 1.5 million child mortality each year globally due to inadequate vaccine coverage[87]. Limited vaccine coverage is attributed to multiple challenges in administration and storage of vaccines especially in the context of developing countries. Firstly, limited access to medical facilities leads to incomplete schedule of booster shots[114]. Secondly, timing of the booster shots is often not closely followed leading to reduced efficacy of vaccines. Lastly, breaks in the cold-chain transport result in limited stability and functionality of the vaccines. There is thus an urgent need for single injection vaccines (SIV) that can preserve vaccine functionality and deliver multiple boluses at pre-defined time[69, 108, 124]. This strategy reduces the need for multiple injections, thus improving vaccine coverage, while also potentially improving therapeutic efficacy. However, SIVs have not yet been commercialized due to challenges including antigen instability and inconsistent release kinetics.

Controlled cargo release has been achieved in the past using various organic and inorganic micro- and nanoparticles. However, these techniques often facilitate release profiles that are limited to sustained and immediate burst release. For example, inorganic carriers including silica-based particles have multiple cargo pockets that results in

---

[3] Reprinted with permission from “Nanoengineered Light-Activatable Polybubbles for On-Demand Therapeutic Delivery” by Arun Kumar, S., Good, J., Hendrix, D., Yoo, E., Kim, D., Deo, K. A., . . . Bishop, C. J., 2020, *Advanced Functional Materials*, 30, 2003579, Copyright [2020] by Wiley

sustained short-term release of the cargo (hours to days) [125-127]. These particles can thus not cater to the timing desired for vaccine delivery that is in the order of months to years. In the context of organic carriers, emulsion-based systems are often used where cargo is exposed to organic and aqueous solvents which result in limited cargo versatility[69, 128-132]. Protein-based cargo, in particular, are exposed to damaging conditions during emulsification process leading to protein denaturation and instability[47, 133]. Other approaches have reduced solvent exposure through various modifications, but lack consistency in release kinetics[129]. For example, polyester-based microparticles were fabricated using StampED Assembly of polymer Layers (SEAL). Although this SIV technology enabled delayed pulsatile release, there are several limitations including ineffective sealing causing premature release of the cargo and non-ideal shape of the microparticles posing challenges in injecting the microparticles using a syringe.

To overcome these limitations, we introduce a polybubble technology as a SIV platform by limiting solvent exposure, while accurately achieving pre-defined as well as on-demand release kinetics. Our polyester-based polybubble is an injectable platform with UV-cured polymer shell covering the centered cargo. Unlike other core-shell particles that are fabricated using emulsion-based methods, cargo within our polybubbles are exposed to significantly less organic solvent and thus can potentially preserve cargo stability. This polybubble platform can also enable delayed burst release profile that are particularly useful for vaccine applications while emulsion-based particles often enable continuous sustained release. On-demand delivery of cargo can also be achieved using our polybubble platform by incorporating light-responsive gold nanorods (AuNR) within the polybubble. These light-responsive polybubble can be actuated upon near-infrared (NIR) exposure, which can penetrate few centimeters through the skin[134, 135]. In addition, photoacoustic imaging can be used to enable tracking of these nanoengineed polybubbles after injection[136, 137]. In this paper, cargo versatility of the polybubbles and delayed release of cargo from non-light activatable polybubbles are characterized. *In vitro*, *ex vivo* and *in vivo* ability of these polybubbles to be light activated and *in vitro* and *ex vivo* studies for on-demand delivery of loaded cargo from the polybubbles are also evaluated. It is expected that the polybubble technology can be used for on-demand delivery of various therapeutics including small molecules drugs, antigens, proteins, peptides, and nucleic acids.

3.2. Results & Discussion

3.2.1. Formation and Characterization of Polybubbles

Polybubbles were fabricated using a phase-separation approach, where cargo dissolved in aqueous phase was injected into the polymer “bubbles” in organic phase (**Figure 3.1a**). Subsequently the polybubble is cured to obtain a solid polybubble (see methods section for details). We used two different types of polymers - polycaprolactone (PCL) and poly (lactic-co-glycolic acid) (PLGA) to form polybubbles. PLGA diacrylate (PLGADA) was commercially purchased to form PLGA polybubbles whereas PCL triacrylate (PCLTA) was synthesized in house to form PCL polybubbles. Endcapping of PCL with the triacrylate groups was confirmed using nuclear magnetic resonance (**Figure 3.1b**). PCL and PLGA were selected due to their similar mechanical stability, biocompatibility and tunable degradation profile. Size of the cured polybubbles were measured using the scanning electron microscope (SEM) images and were found to be 900 μm in diameter (**Figure 3.1c**). This size could potentially be optimized further using an automated platform to enable systemic injection. Polybubbles were manually cut in half using a razor to confirm the non-hollow interior of the cured polybubbles. The cytocompatibility of the PLGA polybubbles was studied by determining metabolic activity of human ovarian carcinoma cells (SKOV3) over multiple time points (day 5, 10, 15, and 25) (**Figure 3.1d**). No significant difference (t-test, $*p<0.05$) was observed between the groups (polybubble and control) indicating that there is no cytotoxicity associated with the polybubbles and the fabrication approach.

Upon ensuring the cytocompatibility of the polybubbles, aqueous cargo was injected into the polybubbles and subsequently subjected to UV curing. Polybubbles with centered cargo limits the exposure to organic solvent that is typically observed in core shell particles formed using emulsion-based methods. By direct injection of cargo in center of polybubbles, issues related to sealing can also be avoided[69]. It is also crucial to have spherical polybubbles to ensure consistent laser activation and release of cargo from the polybubbles. However, cargo centering and maintaining the sphericity of polybubbles proved to be challenging. Cargo had the propensity to move upwards towards the surface of the polybubble while the polybubble sunk to the bottom of vial when formed in water (**Figure 3.1e**). To maintain the sphericity of the polybubbles, viscosity of the aqueous solution, into which polymer is typically injected, was optimized using 10% (wt/vol) carboxymethyl cellulose (CMC). Viscosities of the cargo and the polymer were modified to enable cargo centering within the polybubbles. Specifically, the viscosity of the cargo was increased by mixing the cargo in 5% (wt/vol) CMC and the viscosity of PCL was modulated using potassium carbonate (K_2CO_3) that was isolated after PCLTA synthesis. Rheology study indicated that increasing K_2CO_3 concentration increased the dynamic viscosity of PCL which in turn enabled cargo centering in PCL polybubbles (**Figure 3.1f**). PCL polybubble mixed with 60 mg/mL of K_2CO_3 had dynamic viscosity of 0.7 Pa.s. When the cargo was injected into this polybubble, cargo had the propensity to stay in the middle. Cargo centering was further confirmed by cutting the polybubble in half using a razor blade and visualizing using SEM (**Figure 3.1g**). Increase in viscosities is likely due to the generation of ionic species upon dissolution of CMC in water and reaction of K_2CO_3 with PCL as a proton scavenger during the endcapping reaction of PCLTA[138, 139]. To ensure that the reacted K_2CO_3 that was mixed with PCL does not negatively interfere with the therapeutic efficacy of the cargo, cytotoxicity studies were conducted in SKOV3 cells using a chemotherapy drug, doxorubicin (DOX), as a cargo. DOX mixed with reacted and unreacted 60 mg/mL K_2CO_3 were administered to SKOV3 cells and these groups were compared to control group that was treated with only DOX. When 1000 nM DOX was used to treat SKOV3 cells, DOX mixed with reacted K_2CO_3 showed reduced SKOV3 viability of 25.7 ± 3%, similar to that of the control group (no statistical difference between the groups). In contrast, DOX with unreacted K_2CO_3 showed increased SKOV3 viability of 68.7 ± 8%. These results validated that the use of reacted K_2CO_3 maintained the therapeutic efficacy of DOX while also increasing the viscosity of PCL. Unlike PCL polybubbles, cargo centering in PLGA polybubbles did not require modulation of PLGA viscosity using K_2CO_3. Similar to PCL polybubbles, PLGA polybubbles were formed in 10% (wt/vol) CMC solution and cargo mixed with 5% (wt/vol) CMC was injected in the middle. Similar to PCL polybubbles, centering of the cargo within PLGA polybubbles were confirmed using SEM images of cut polybubbles.

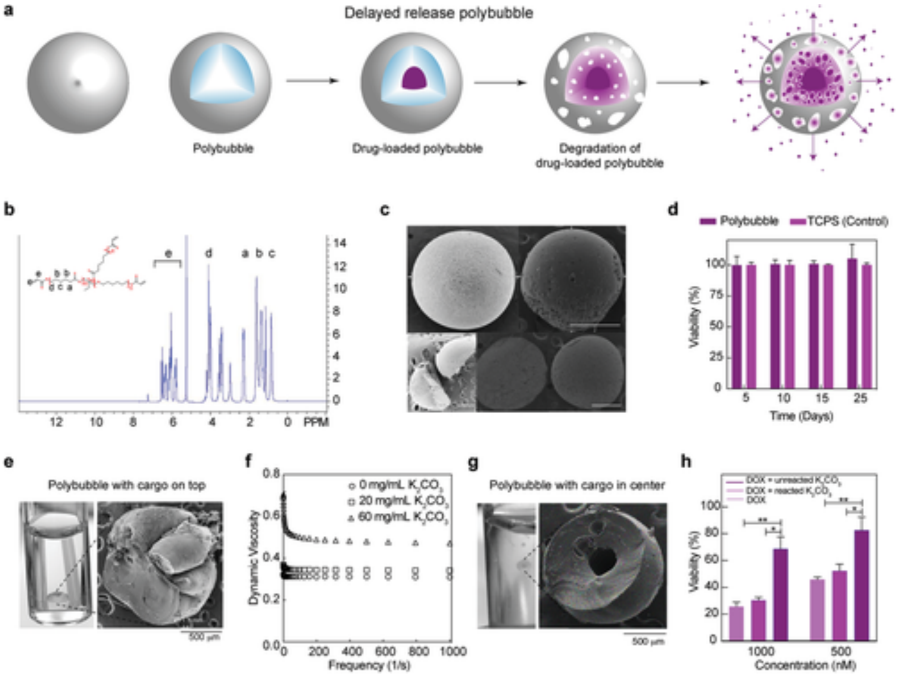

Figure 3.1 Formation and characterization of delayed-burst enabling polybubbles. **a)** Cured polyester-based polybubbles with centered cargo undergoing bulk erosion causing burst release of the cargo. **b)** NMR characterization of PCL that was endcapped with triacrylate groups (peaks labeled as **e**). **c)** SEM images of whole and cut PCL and PLGA polybubbles. Scale bars = 500 µm. **d)** *In vitro* study of SKOV3 cells incubated with PLGA polybubbles for 5, 10, 15, and 25 days shows that no cytotoxicity is caused by PLGA polybubbles. Centering of cargo within the PCL polybubbles were optimized by **e)** modulating the viscosity of the polymer using K_2CO_3 that was isolated after PCLTA endcapping reaction and **g)** modulating viscosity of the cargo using CMC. **f)** Cargo without CMC was injected into the polybubble causing the cargo to move towards to the surface of the polybubble. **g)** Cargo with 5% CMC was injected into the polybubble causing the cargo to be retained within the polybubble. **h)** *In vitro* study of SKOV3 cells treated with 1000 nM and 500 nM DOX and unreacted K_2CO_3, DOX with reacted K_2CO_3, and DOX shows that unreacted K_2CO_3 significantly reduced the therapeutic efficacy of DOX compared to reacted K_2CO_3. $^{**}p<0.01$, $^{*}p<0.05$, one-way ANOVA. Reprinted with permission from John Wiley and Sons from Arun Kumar *et al.* [140]

3.2.2. Delayed burst release from PCL and PLGA polybubbles

After successful cargo centering within the PCL polybubbles, release studies were conducted. PCL polybubbles were loaded with a small molecule, acriflavine, and subjected to accelerated release conditions (50 °C and 70 °C) to assess the release kinetics. Delayed burst releasees peaked on day 170 from polybubbles incubated at 50 °C and on day 58 from polybubbles incubated at 70 °C (**Figure 3.2a & 3.2b**). Although accelerated release studies showed delayed burst release of cargo in PCL polybubbles, burst release at physiological temperature would likely be delayed further (1-2 years)[141]. For vaccine applications that require booster shots to be administered periodically, polymers like PCL with slow degradation rate would be highly desirable. However, vaccines that require shorter intervals between doeses and various other biomedical applications including delivery of synergistic chemotherapeutic agents could benefit from polymers that have high degradation rate. PLGA is one such polymer that is known to have faster degradation rate compared to PCL[142]. As expected, delayed burst release of the cargo from PLGA polybubbles was observed much earlier when compared to that of PCL polybubbles. Delayed burst release peaked on day 16 from PLGA polybubbles that were incubated at 37 °C and day 4 from PLGA polybubbles incubated at accelerated release condition (50 °C).

Cargo versatility of the polybubbles was also tested by assessing the release profiles of protein. Release studies were conducted with fluorescently-labeled protein, BSA-488, as the centered cargo. In PCL polybubbles, release studies were conducted at

37 °C and at 50 °C and not at 70 °C because the cargo type is antigen which is highly sensitive to temperature. Delayed burst release peaked on days 58 and 90 from PCL polybubbles that were incubated at 37 °C. For PCL polybubbles that were incubated at 50 °C, release was continuous and did not indicate delayed release trend (**Figure 3.2a & 3.2b)**. This difference is likely due to the effect of higher temperature on the antigen. Denaturation and breaking down of the antigen could potentially have caused the fluorophore detachment from the antigen and escape through the pores at higher temperatures. Release studies of PLGA polybubbles with BSA-488 as the centered cargo were also conducted at 37 °C and at 50 °C. Delayed burst releases peaked on day 21 and day 7 for release studies conducted using polybubbles that were incubated at 37 °C and 50 °C, respectively. Although delayed burst releases were observed in PCL and PLGA polybubbles with different cargo types in the center, timing of cargo release is observed to be different. This difference in release profiles in the two cargo types is likely due to the size of the cargo and its mobility through the pores. Small molecules like acriflavine tend to diffuse through smaller pores resulting in an initial burst release effect seen in PCL polybubbles while large molecules like BSA-488 requires large interconnected pores to diffuse through the polymer shell. It is thus crucial to study the diffusion kinetics of different cargo types to accurately predict the release profile from the polybubbles.

3.2.3. Diffusion of different cargo types and porosity of polybubbles

Polyester-based polybubbles (PCL or PLGA) are expected to show similar diffusivity trend as all the polyesters typically go through bulk erosion. PCL polybubbles with acriflavine or BSA-488 as centered cargo were incubated for pre-defined time points

(1-15 weeks) (**Figure S1**). At each time point, polybubbles were cut in half and the drug distribution was quantified by measuring the fluorescence in the polybubbles (**Figure 3.2c**). Diffusion through the polymer shell was assessed by dividing the shell into five parts (1st – center and 5th periphery). Small molecules uniformly diffused through the polymer wall resulting in uniform release of cargo over time. In contrast, relatively larger cargo, BSA-488, exhibited non-uniform diffusion resulting in pockets of antigen being distributed throughout the polymer wall. As hypothesized earlier, this difference in diffusion pattern is likely to have resulted from both the cargo size and pore size within the polymer shell. Small molecules, like acriflavine, are more likely to diffuse through the smaller pores relatively easily compared to that of larger molecules, such as BSA-488. Diffusion trend is a crucial factor in predicting release of cargo and these results highlight the importance of understanding the diffusivity of various cargo types within the delivery platform.

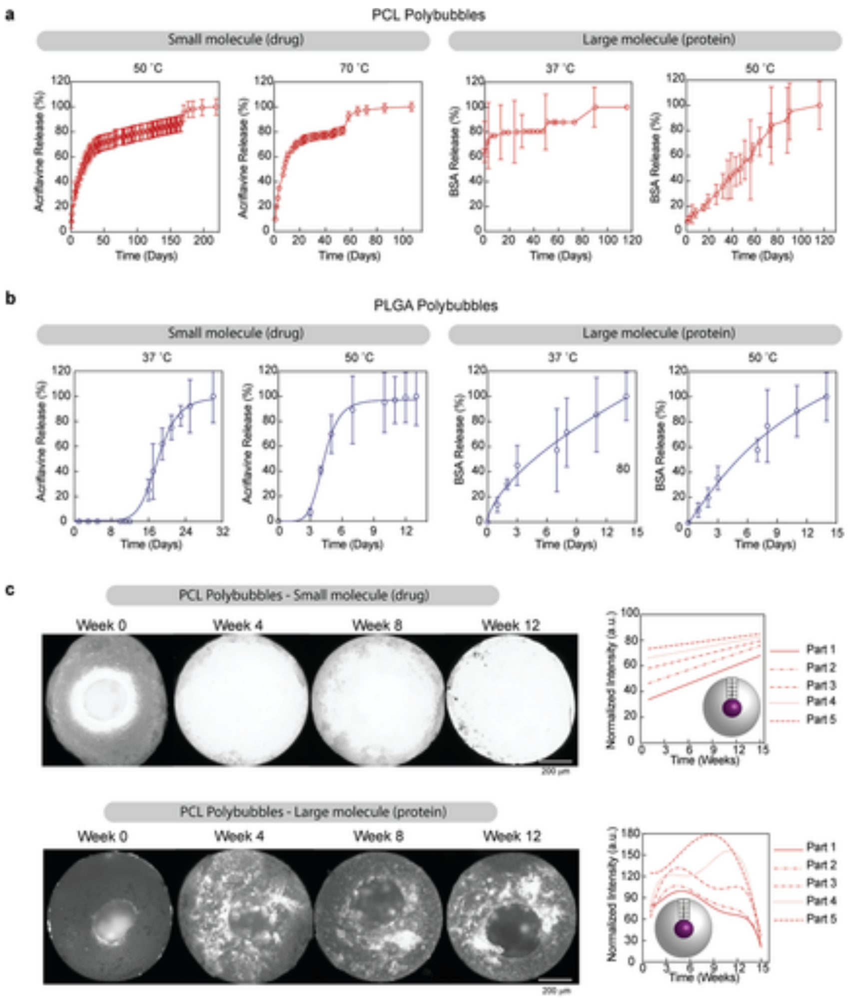

Figure 3.2 Delayed-burst release from polybubbles. a) Delayed burst release of acriflavine at 37 °C (day 16) and 50 °C (day 4) and release of BSA-488 from PLGA polybubbles at 37 °C (day 21) and 50 °C (day 7). b) Delayed burst release of acriflavine from PCL polybubbles at accelerated degradation conditions 50 °C (day 170) and 70 °C (day 58) and release of BSA-488 from PCL polybubbles at 37 °C (days 58 and 90) and 50 °C. Release of acriflavine was not observed at 37 °C owing to the long degradation rate of PCL polybubbles. c) Quantification of diffusion of acriflavine and BSA 488 through the wall of PCL polybubbles. Difference in diffusion pattern of acriflavine and BSA-488 potentially causes the difference in the release profiles of acriflavine and BSA-488 that are observed in 2a and 2b. Scale bars = 200 µm. Reprinted with permission from John Wiley and Sons from Arun Kumar *et al.* [140]

Diffusion patterns, irrespective of the cargo type, are also heavily dependent on the polymer porosity. Polyesters like PCL and PLGA typically undergo bulk erosion that are characterized by volume loss caused by increasing number of pores within the particles. Unlike surface erosion, overall size of the particle remains constant until complete degradation. Thus, porosity of the polybubbles were analyzed to better understand the degradation profile of the polybubbles. Both PCL and PLGA polybubbles were used for this study because of the difference in the degradation time of the two polyesters. Polybubbles that were cut in half for the diffusion study performed using confocal microscopy (**Figure S2, S3**) and SEM images. Number of pores on the outer surface and inner surface of the polybubble halves were quantified. In both PCL and PLGA polybubbles, the number of pores on the outer surface increased over time (**Figure 3.3a, 3.3b**). However, there was variability in the timeline during which the number of pores increased in the PCL and PLGA polybubbles owing to different degradation profiles. PCL is a slow degrading polymer causing the pore numbers to increase at a slower rate compared to that of a fast degrading polymer like PLGA. Additionally, the number of pores on the inner side of the cut polybubble does not increase over time. In PCL polybubbles, the number of pores on the inner side stayed constant throughout the 15 weeks of study as the degradation rate of PCL was much slower (**Figure 3.3a**). In PLGA polybubbles, no pores were observed until the end stages of degradation on day 15. By this point most pores are connected throughout the shell enabling the cargo to be released. The presence of lesser number of pores on the inner side could be the result of the high-water content that the outer surface of the polybubble is exposed to compared to that of the polybubble core. Because the polybubbles are lyophilized after cargo injection, less humidity is expected to be trapped within the core. However, incubating the polybubbles in PBS exposes the outer surface of the polymer to water resulting in increased number of pores on the outer side of the polybubbles. It is also important to note that pore size increases with degradation as observed in the SEM morphology images of outer and inner surfaces of PLGA polybubbles (**Figure S4**). This phenomenon of increasing pore size as it relates to degradation in bulk eroding materials has been extensively studied in the previous studies[143, 144]. Water absorption by the polymer shell, induced by degradation, increases overtime resulting in larger pockets or voids being formed in the shell. Eventually the pores are connected causing the release of the cargo.

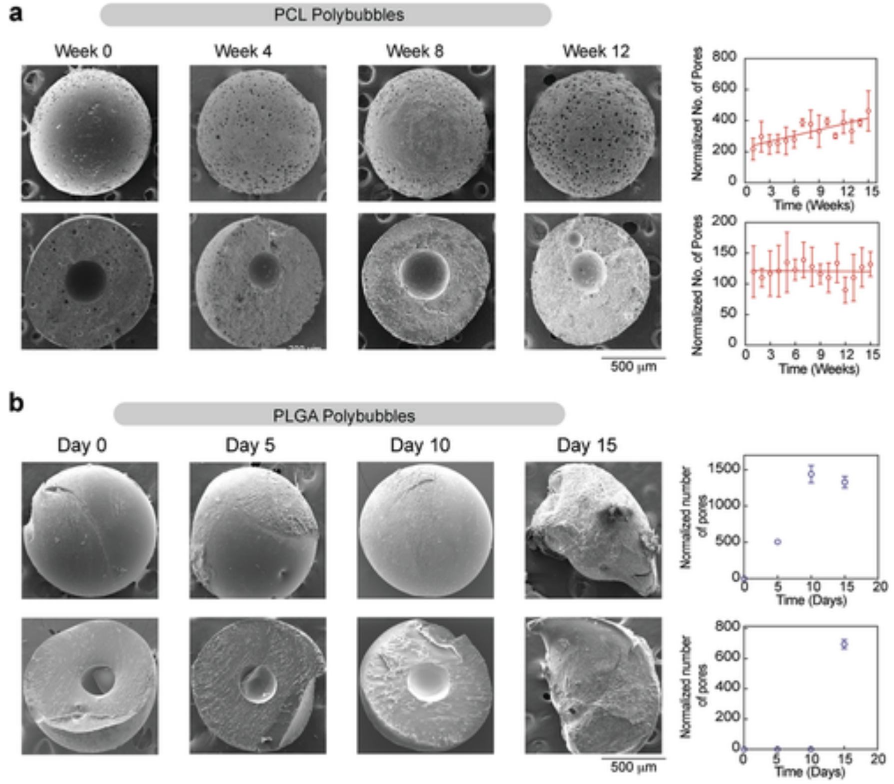

Figure 3.3 Degradation study of the polybubbles. a) Cut PCL polybubbles with increasing number of pores over 12 weeks on the outer surface and constant number of pores on the inner surface of PCL polybubbles. Number of pores increased on the surface of polybubble that was in direct contact with PBS during incubation while number of pores on the inner surface will only increase upon complete degradation of PCL. b) Cut PLGA polybubbles with increasing number of pores over 15 days on the

outer and inner surface of PLGA polybubbles. Number of pores increase as PLGA degrades resulting in delayed release of cargo. Reprinted with permission from John Wiley and Sons from Arun Kumar *et al.* [140]

3.2.4. Laser activation of polybubbles and on-demand release

Our polybubble technology could further benefit the goal of improved vaccine coverage by facilitating increased control over the timing of release. Release kinetics are generally dependent on various factors including polymer type, molecular weight, monomer ratio, and cargo type. However, designing different polymer systems to cater various vaccine schedules is not efficient. Thus, we focused on incorporating "on-demand" delivery of cargo in our polybubble platform (**Figure 3.4a**). By activating the polybubbles after they are injected, the release of cargo can be modulated on a need basis. NIR light can penetrate the skin making it attractive for *in vivo* applications and thus we wanted to use NIR-sensitive agents during the polybubble formation.

AuNRs have been extensively studied for their ability to absorb NIR light further leading to heat activation. CTAB-stabilized AuNRs were synthesized and were phase-transferred from aqueous solution to organic solvent, chloroform, based on previously published protocol[145] (**Figure S5**). The AuNRs' transverse and longitudinal diameters were 13 ± 4 nm and 50 ± 14 nm, respectively (**Figure 3.4b**). Hydrophobicized AuNRs were mixed with the polymer (PCL or PLGA) prior to polybubble formation thus localizing AuNRs in the polymer shell. Cargo was subsequently injected in the middle and the polybubbles were cured. Polybubbles were then incubated in PBS and were heat activated using NIR laser for 5 minutes. Timing of laser activation was determined to be 5 minutes after conducting a release study using different groups of PLGA polybubbles that were laser activated for 0, 5, 10, 15, and 20 minutes (**Figure S6**). We then characterized the release kinetics of these polybubbles upon the incorporation of AuNRs. Release studies were conducted under the same conditions as described above. The only variable that was altered was intermittent laser activation of the polybubbles. The supernatants were replaced with fresh PBS before the laser activation. Supernatants were collected after the 5 minutes of lasering and fluorescence was measured. This study showed that burst release occurred at earlier time points in both PCL and PLGA polybubbles compared to that of polybubbles without laser activation. For PCL polybubbles, burst release occurred on day 170 when incubated at 50 °C without laser activation while with laser activation the release was expedited to day 84 (**Figure 3.4c**). Similarly, for PLGA polybubbles, burst release peaked on day 19 when incubated at 37 °C while earlier burst release was observed to peak on day 7 from the polybubbles that were laser activated (**Figure 3.4c**). This study shows that there is a significant impact of AuNR-facilitated laser activation on the release kinetics of the cargo. Earlier release of cargo is likely due to the accelerated degradation of the polymer shell that is in turn caused by the increase in temperature. This feature of our polybubble platform thus has the potential to be clinically instrumental in the timely delivery of the cargo.

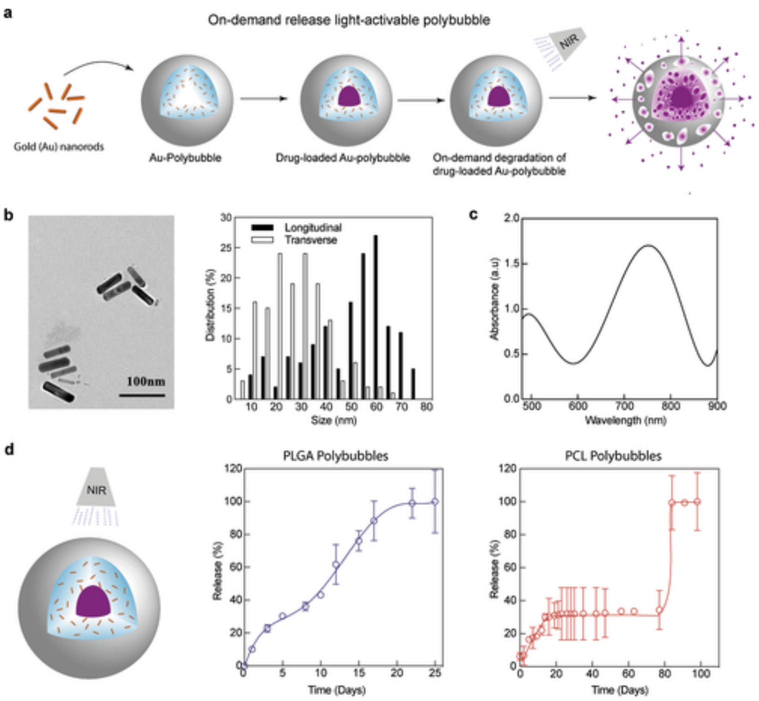

Figure 3.4 Characterization of gold nanorods (AuNRs) and laser-activated polybubbles. a) Polybubbles with AuNRs in the shell degrades faster upon multiple NIR laser activations. b) TEM images used for size characterization of longitudinal and transverse dimensions of synthesized AuNRs. c) Absorbance spectrum of AuNRs in the visible-NIR wavelength range. d) Expedited burst release from PLGA and PCL polybubbles (day 81) upon multiple periodic NIR laser activations. Reprinted with permission from John Wiley and Sons from Arun Kumar et al. [140]

Another interesting observation was made during the laser activation release study regarding repeated exposure of polybubbles to the laser. The temperature change from before and after laser activation stayed relatively constant even after multiple laser sessions. For PCL and PLGA polybubbles, the temperature change observed to be 12 ± 1 °C and 11 ± 2 °C, respectively, and this change was maintained over time (**Figure 3.5a**). In previous studies, AuNRs have been known to lose their absorption efficiency after being laser activated multiple times[146-148]. However, AuNRs retained their shape and thus maintained their absorption efficiency because AuNRs were entrapped within the rigid polymer shell. In addition to effective laser activation, validation of therapeutic efficacy of the cargo that is released upon laser activation is also crucial to ensure clinical success. PLGA polybubbles with centered DOX and AuNRs in the shell were incubated in cell culture media and were subjected to repeated NIR laser exposure. Supernatants were replaced with new media before and after each session of laser activation. Supernatants from both the groups, laser activated and non-laser activated polybubbles, were delivered to SKOV3 cells. Average increase in temperature was observed to be 12 ± 1 °C and was maintained throughout the release study (**Figure 3.5b**). Release of DOX was quantified using fluorescence measurement of the collected supernatants. Similar to the previous release studies, DOX release was expedited by 10 days in the laser group compared to the control group (**Figure 3.5c**). Reduction in cell viability was also significantly higher in cells that were treated with supernatants from laser-activated polybubbles compared to that of the control group on days 7 and 15 (**Figure 3.5d**). This reduction corresponds to the increased release of DOX from laser-activated polybubbles observed in **Figure 3.5c**. These results validate that therapeutic efficacy of cargo is infact preserved after the release from the polybubbles upon laser activation.

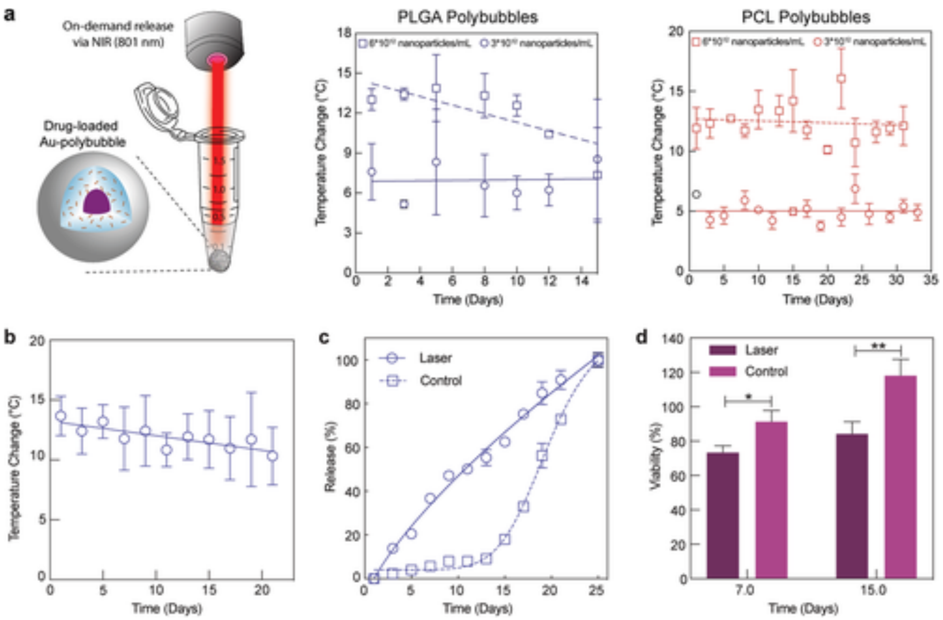

Figure 3.5 NIR-laser activation of polybubbles. a) *In vitro* activation of PLGA and PCL polybubbles using 801 nm laser resulting in temperature change of 11 ± 2 °C and 12 ± 1 °C, respectively. b) Laser activation of PLGA polybubbles and subsequent *in vitro* assessment of therapeutic efficacy of DOX. c) NIR Laser activation of PLGA polybubbles with centered DOX resulting in 12 ± 1 °C. d) Expedited release of DOX from NIR-activated PLGA polybubbles by 10 days compared to that of the control group. d) Reduced viability of SKOV3 cells observed when treated with DOX released from NIR laser activated polybubbles (n = 3). *p<0.05, **p<0.01, t-test. Reprinted with permission from John Wiley and Sons from Arun Kumar et al. [140]

3.2.5. *In vivo* and *ex vivo* laser activation of polybubbles

Upon successful laser activation of polybubble *in vitro*, we then tested *in* vivo efficacy of laser activation. We injected the PCL polybubbles with AuNRs in the shell into a melanoma tumor of balb-c white mice and observed the temperature differences from before and after laser activation (**Figure 3.6a**). There was a significant temperature increase of 8 ± 1 ℃ (t-test, P < 0.0001) after laser activation in mice that were injected with the AuNR-polybubbles compared to that of the control mice. Successful laser activation *in vitro* and *in vivo* thus strengthens the prospect of translatability of this platform. After successful *in vitro* and *in vivo* laser activation studies, we wanted to assess the release kinetics of the cargo in physiological conditions. We thus carried out *ex vivo* laser-activated release study in bovine tissue. Release studies were carried out using PLGA polybubble with another centered small molecule, acriflavine. Polybubbles were laser activated for 5 minutes once every two days and the supernatants were replaced with fresh PBS. On day 11, the polybubbles were removed from the PBS and were placed between bovine cartilage and 1 cm of bovine meat (**Figure 3.6b**). Fluorescence images that were taken before and after laser activation showed that acriflavine was released into the surrounding cartilage upon laser activation. Quantification of the fluorescence images showed that fluorescence within the polybubble decreased from 98% to 30% after laser activation indicating the release of cargo (**Figure 3.6g**). In contrast, fluorescence of the cartilage increased from 2% to 70% after laser activation. This indicates that laser activation resulting in expedited cargo release can be successfully carried out *ex vivo*. Hence, polybubble technology can potentially be activated extracorporeally using NIR laser to cater on-demand delivery of the cargo.

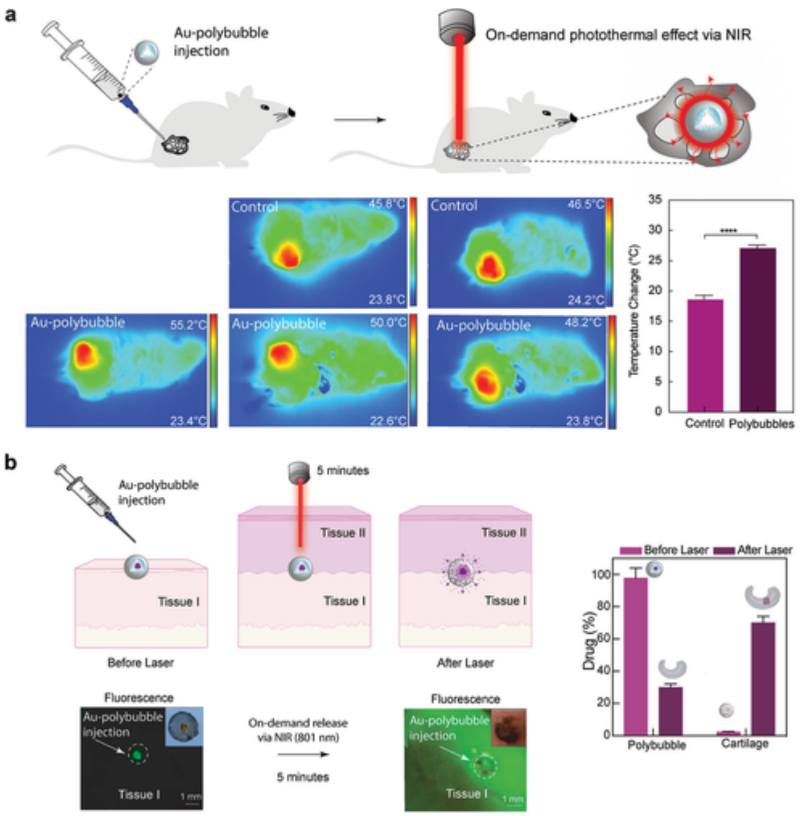

Figure 3.6 *In vivo* and *ex vivo* laser activation of polybubbles. a) *In vivo* laser activation of AuNR-polybubbles upon injection into melanoma tumor of Balb-C mice and temperature increase of 8 ± 1 °C observed after *in vivo* NIR laser activation of AuNR-polybubbles (n=3). ****p<0.0001, t-test. b) *Ex vivo* release study of PLGA polybubble with centered acriflavine upon laser activation. Acriflavine from PLGA polybubbles was released onto the cartilage upon NIR laser activation (n = 2). Scale bars = 1 mm. Reprinted with permission from John Wiley and Sons from Arun Kumar et al. [140]

3.3. Conclusions

We have successfully developed a polyester-based platform technology for controlling the release of cargo. Unlike other emulsion-based approaches, our technology comprises of a single large cargo pocket in the middle versus many small cargo pockets dispersed throughout the polymer shell, like in the case of micro/nanoparticles. This essentially minimizes the surface area of the cargo that is exposed to organic solvent. As a result, a variety of cargo types can be used including antigens, proteins and peptides that are often sensitive to organic solvents. These polybubbles were further used to achieve novel delayed burst kinetics in both types of polyesters, PCL and PLGA. Small and large molecule cargo were used to demonstrate delayed burst release from the polybubbles strengthening the claim about cargo compatibility. Release kinetics was also successfully modulated using NIR-activatable AuNRs. Multiple laser activations enabled the temperature of the polybubbles to be increased consistently by at least 13 °C in both PCL and PLGA polybubbles. Use of AuNRs further expedited the release of cargo in PCL polybubbles and in PLGA polybubbles *in vitro* and *ex vivo*. Overall, our theranostic-enabling delivery platform technology is based on biodegradable components that can be used for controlled delivery of many therapeutic agents including small molecules, antigens, proteins, peptides, and nucleic acids**.**

3.4. Experimental Section

3.4.1. Materials

Acriflavine (Chem-Impex International); acryloyl Chloride (Sigma Aldrich); ascorbic acid (Fisher Chemical); bovine serum albumin 488 (BSA-488) (Invitrogen); bromosalicylic acid (ACROS Organics); carboxymethylcellulose (CMC) (Alfa Aesar); centrimonium bromide (CTAB) (); chloroform (Fisher Scientific); chloroauric acid (Fisher Scientific); dichloromethane (DCM) (ACROS Organics); diethyl ether (Fisher Chemical); doxorubicin hydrochloride (Fisher Scientific); 2-hydroxy-4′-(2-hydroxyethoxy)-2-methylpropiophenone (photoinitiator) (Sigma Aldrich); mPEG thiol (Laysan Bio); phosphate saline buffer (PBS) (Gibco); polycaprolactone (14 kDa; Sigma

Aldrich); polycaprolactone triol (300 Da) (ACROS Organics); poly (lactic-co-glycolic acid) diacrylate (5kDa) (CMTec); potassium carbonate (K2CO3) (ACROS Organics); silver nitrate (Fisher Chemical); sodium borohydride (Fisher Chemical); triethyl amine (ACROS Organics)

3.4.2. Methods

3.4.2.1. Polymer for polybubble shell

Two types of polyesters were used, namely, PCL and PLGA. For the formation of PCL polybubbles, 1000 mg/mL of 14 kDa PCL and synthesized 300 Da PCL triacrylate (PCLTA) were mixture in a 1:3 (vol/vol). PCL is known to have a slower degradation rate and thus mixture of non-crosslinked and crosslinked chains would be beneficial in increasing the degradation rate thus potentially leading to earlier cargo release. We will discuss the synthesis, the quantification of PCLTA's viscosity, and quantification of PCLTA's absolute molecular weight. For PLGA polybubbles, 1200 mg/mL of commercially purchased 5 kDa PLGADA was prepared in chloroform.

3.4.2.1.1. Polycaprolactone triacrylate (PCLTA) Synthesis

In a round bottom flask, 3.2 mL of PCL triol was dried overnight at 50 °C under the low-pressure conditions using a water bath. Potassium carbonate (K_2CO_3) of mass 4.146 g was dried at 90 °C overnight. Two-fold excess of dichloromethane (DCM) was used to dissolve PCL triol and dried K_2CO_3 was added to this mixture. Acryloyl chloride was measured based on the 1:3 molar ratio of PCL triol and acryloyl chloride. Acryloyl chloride was then dissolved in 2-fold excess of DCM and was added dropwise to the PCL triol and K_2CO_3. The reaction was carried out for 24 hours under argon at room temperature and was filtered to remove excess K_2CO_3. The filtrate was then purified in 3-fold excess diethyl ether on a secondary container with ice. The purified PCLTA was then rotary evaporated to remove excess diethyl ether. The resultant oily PCLTA was then stored in the vacuum chamber overnight to remove residual diethyl ether.

3.4.2.1.2. Quantification of PCLTA viscosity

PCLTA was mixed with various concentrations (0 mg/mL, 20 mg/mL, 60 mg/mL, 80 mg/mL) of reacted K_2CO_3 that was filtered after PCLTA synthesis. Anton Paar rheometer was used to change shear rate from 1 to 1000 1/s with 31 data points. Then dynamic viscosity was calculated using shear stress (Pa) and shear rate (1/s).

3.4.2.1.3. Quantification of absolute molecular weight of PCLTA

Mercury system (300 Hz) was used to analyze the polymer composition of PCLTA. PCLTA was quantified via nuclear magnetic resonance (NMR; TYPE; Bruker) by dissolving 100 μL sample in 900 μL of deuterated (D)-chloroform. Then 700μL of each of the solution was transferred to their respective NMR tubes. Distinct proton signals corresponding to vinyl (endgroup) protons were identified and number of repeating units were calculated using the formula: n = ((sum of CH2 proton integrals)/# of CH2 protons) / (integral per proton value). Molecular weight of the polymer was then calculated using the formula: (FW end groups) + ((FW repeating unit)*(n)) [149].

3.4.2.2. Polybubble formation, solidification, and lyophilization

3.4.2.2.1. Polybubble formation

For further information about polybubble formation, please refer to [150]. Excess K_2CO_3 that was filtered out during the PCLTA synthesis was mixed with PCLTA to yield concentration of 60mg/mL to increase the viscosity to assist in cargo centering. PCLTA and K_2CO_3 mixture was then mixed with commercially purchased non-acrylate PCL in a 3:1 volume ratio. Polybubble tube using stainless steel (O.D.: 0.508 mm, I.D.: 0.254 mm) or Nitinol (O.D.: 0.4064 mm, I.D.: 0.01 mm, 5 feet)

3.4.2.2.2. Ultraviolet (UV)-curing and lyophilization of the polybubble

To cure polymer mixture, 200 μL of either PCL/PCLTA or PLGADA was triterated with 2 μL of photoinitiator. After polybubbles were formed in 10% CMC solution in a 4 dram glass vial, the polybubbles were exposed to UV for 60 seconds. Cured polybubbles were then flash frozen in liquid nitrogen for 30 seconds and were lyophilized overnight.

3.4.2.3. Cargo used for loading polybubbles

3.4.2.3.1. Small molecules

150 μL of 500 μM doxorubicin (DOX) was added to 100 μL of 5% CMC. This solution was then injected into the polybubble using a stainless-steel tube using a 33 G round wire (O.D.: 0.2032 mm, I.D.: 0.1016 mm). 10 mg/mL acriflavine was prepared in DI water as cargo stock solution and then 1 mg/mL acriflavine was prepared using the 10 mg/mL stock solution in 5% CMC solution (aqueous). For cargo in the shell, 10 mg/mL acriflavine was prepared in DMSO and 10% (v/v) acriflavine was mixed with the polymer solution.

3.4.2.3.2. Protein-dye conjugate

0.5 mg/mL of BSA-488 was injected in the middle of the polybubbles and release studies were carried out at 37 °C and 50 °C.

3.4.2.3.3. Loading of drug within the polybubble

Syringe pump (KD Scientific) was used to inject the polybubbles at the rate of 0.5 μL/sec. 31 G needle was used manually inject 1 mg/mL acriflavine or 0.5 mg/mL BSA-488 in 5% CMC in the middle of the polybubble.

3.4.2.4. Centering of drug within the polybubble and release studies

3.4.2.4.1. Centering of drug within the polybubble

Viscosity of the polymer was modulated increasing the concentration of K_2CO_3 that was isolated after the synthesis of PCLTA. Viscosity of the cargo was modulated using 5% (w/v) CMC.

3.4.2.4.2. Release Studies (PCL)

Release studies of PCL polybubbles with cargo in the middle and in the shell were incubated in 400 μL of PBS at 37 °C. However, PCL is known to have a longer degradation time [151] and thus accelerated degradation studies were conducted by increasing the incubation temperatures. Polybubbles were incubated at 50 °C, 70 °C, and 90 °C and supernatants were collected at the desired time points. Samples were then filled with 400 μL of fresh PBS. Fluorescence intensities of the cargo in the supernatants were later measured using Cytation 5 (Biotek). Fluorescence data were then compared to that of the calibration curve of the cargo to determine the amount of cargo released.

3.4.2.5. Characterization of polybubbles in the absence of AuNRs

3.4.2.5.1. Quantification of melting temperature of PCL Polybubble

Differential Scanning Calorimetry (DSC) (Q_2O, TA Instruments) was used to quantify the melting temperature transition point (T_m). Between 5 mg and 10 mg of polymer sample was weighed in an aluminum pan (T_0, TA Instruments) and the lid was secured using a standard crimper. To quantify the PCLTA polybubble, the heating cycle ramped up the temperature from -40 °C to 150 °C at 1 °C/minute (our instrument was not capable of going below -40 °C and we were interested in quantifying the T_m).

3.4.2.5.2. Release Studies

Polybubbles were incubated in 400 μL of PBS and supernatants were collected at various time points. Polybubbles were then incubated with fresh PBS. Tubes were secured with yellow cap lock to prevent evaporation of PBS.

3.4.2.5.3. Quantifying internal drug distribution

PCL polybubbles with cargo in the middle were incubated in PBS at 50 °C for time points ranging from week 1 to week 15. Polybubbles from each time point were removed from the supernatants and were cut in half using the razor blade. Halved polybubbles were then imaged using Zeiss fluorescent microscope. Fluorescence in the shell of the polybubble was quantified by equally dividing the top half of each polybubble into five parts. Fluorescent intensities were quantified using ImageJ software.

3.4.2.5.4. Quantification of pore formation

Polybubbles that were cut in half for assessing drug distribution were used for this study. The halved polybubbles were sputter coated with gold such that the outer surface of one half of the polybubble and the inner surface of the other half of the polybubble were coated. SEM images of the polybubbles from each time point (every week from week 1 to week 15) were taken using the FEI Quanta 600 and triplicates were used for each time point. The SEM images were then converted to black and white images in ImageJ such that the pores were black. Then the pore sizes were measured using the circularity constraint in ImageJ. Number of pores along with the standard deviation were then determined for each time point.

3.4.2.6. AuNR synthesis, hydrophobicization, and characterization

3.4.2.6.1. AuNR synthesis

We added 420 µL of seed solution (as follows) to the growth solution (as follows) which was left to react for 16 hours. Excess CTAB was then removed by centrifuging for 30 minutes at 8k relative centrifugal force (RCF). The AuNR seed solution was made by mixing 250 µL of 10 mM $HAuCl_4$, 7.5 mL of 100 mM CTAB, and 600 µL of 10 mM ice cold $NaBH_4$ to a tube. The contents were then mixed for two minutes. The AuNR growth solution was made by thoroughly mixing 40 mL of 100 mM CTAB, 1.7 mL of 10 mM $HAuCl_4$, 250 µL of $AgNO_3$, and 270 µL of 17.6 mg/mL Ascorbic acid to a tube.

3.4.2.6.2. Hydrophobicization of AuNRs

In order we used two different methods for hydrophobicizing AuNRs. The first entailed toluene, and the second entailed chloroform. In the toluene-based approach, we added 2 mL of AuNRs to a scintillation vial and added 0.102 mL of undecanethiol to the vial. For every 2.102 mL of AuNR and undecanethiol, 0.51 mL of acetone and toluene was added. Added another 0.51 mL of acetone. This was spun in multi-stir plate for a few seconds. Pipetted out the top layer of organic phase and stored it in a separate scintillation vial. Repeated the addition of acetone and toluene steps and separation of organic phase until the aqueous phase is cloudy and colorless and the organic phase is clear [152]. For the chloroform-based approach, the pH of 5.1 nM of CTAB-stabilized AuNRs was adjusted to 10 using 1 mM NaOH and AuNRs were stirred with 0.3 mM mPEG thiol at 400 RPM overnight [145]. 0.4 M of DDA was prepared in chloroform and was stirred with PEGylated AuNRs for four days at 1200 RPM.

3.4.2.6.3. AuNR characterization

We characterized the AuNRs' transverse and longitudinal diameters using transmission electron microscopy (JEM-2010 TEM; JEOL). A stock solution of AuNRs were placed for 30 seconds on the carbon-coated copper grid (10nm thickness Formvar film grid; Electrin Microscop Services) face to allow for AuNR adsorption with and without ethanol. Subsequently, the excess solution was blotted for removal. The concentration of AuNRs were characterized using Cytation 5 (Biotek) assuming extinction coefficient of $2*10^9$ L/mol.cm [153]. Three wells of an acrylic 96 well plate were filled with 100 µL of filtered AuNRs. One well was filled with 100 µL of DI water to obtain the background absorbance. Then the spectral scanning absorbance setting was used to measure the absorbance of AuNRs between 300 nm and 900 nm with a step size of 1 nm.

3.4.2.7. Characterization of polybubbles with shell-loaded AuNRs

3.4.2.7.1. AuNR and polybubble heating (in vitro)

Because near infrared (NIR) penetrates biological tissue on the order of a few centimeter [154],we were interested in using NIR wavelengths (801 nm) to heat polybubbles and we did so using AuNRs which have surface plasmon resonance (SPR) wavelengths in the NIR which enables them to heat. We similarly heated polybubbles with AuNRs (in 400 µL PBS) for 5 minutes using the NIR laser with 13.4 watts (spot size of ~1 cm) and temperature of both PCL and PLGA polybubbles before and after lasering was compared. An FTIR camera was used to record the temperature change during the lasering process.

3.4.2.7.2. Drug release with shell-loaded AuNRs

Polybubbles with small molecule, acriflavine, in the middle and AuNRs in the shell were incubated at 37 °C for PLGADA polybubbles and at 50 °C for PCL/PCLTA polybubbles. Every Monday, Wednesday, and Friday, the polybubbles were laser activated for 5 minutes using the NIR laser at 801 nm and 8 A power. Supernatants were collected before laser activation and polybubbles were incubated with 400 µL of fresh PBS. To measure the amount of cargo released after laser activation, supernatants were collected again and fluorescence intensities were measured using Cytation 5 (Biotek, VT). Polybubbles were incubated with 400 µL of fresh PBS until the next laser activation time point.

3.4.2.8. In vivo work involving the thermotherapy capabilities of the polybubble

3.4.2.8.1. Cell culture for in vivo study

Melanoma (B16F10) cells, passage 5, were cultured in T175 flasks at 1 X 10^5 cells/mL in RPMI-1640 medium with L-Glutamine supplemented, 10 % fetal bovine serum (FBS), and 2 % penicillin streptomycin. B16F10 at a density of 5 X 10^6 cells were seeded in a T175 flask under standard conditions at 37 °C with 5 % CO_2 and 100 % humidity.

3.4.2.8.2. Subcutaneous (s.c.) inoculation of melanoma cells and In vivo study

All the experimental protocols were approved by Texas A&M University Institutional Animal Care and Use Committee. To produce solid melanoma in the mice, BALB/c mice (n=6) were inoculated with B16F10 cells via subcutaneous injection of 5 X 10^6 cells in 100 µL of PBS. After tumor inoculation, the tumor nodules were allowed to grow approximately 50 to 100 mm^3 for 2 weeks. One polybubble in 100 µL PBS was applied to the tumor via intratumoral injection. Immediately after the intratumoral injection, near infrared (NIR) laser light (Jenoptik Laser GmbH, Jenoptik, Germany) at 803 nm with 8 A applied to tumor area for 3 minutes. To validate the heat generation, the temperature of the exposed tumor with a microbubble and with PBS (without a polybubble) as a control was monitored by a thermal camera (FLIR-A300, FLIR Systems Inc., MA, USA) during the NIR irradiation.

3.4.2.9. In vitro and ex vivo work involving on-demand release of polybubbles upon laser activation

3.4.2.9.1. Cell culture for in vitro study

PLGA polybubbles with AuNRs in the shell were formed as described in 4.2.2 and 0.1 µL of 3 mg/mL DOX was injected in the middle. Polybubbles were incubated in 200 µL McCoy's 5A media and were laser activated for 5 minutes using 8A of 801 nm NIR laser once every two days. Supernatants were collected after each laser activation and were replaced with fresh media. 100 µL of the supernatant was used to obtain fluorescence measurements using Cytation 5 (Biotek). SKOV3 cells were seeded in a 96-well plate (5000 cells/well) and 16 hours after seeding, 100 µL of the supernatants from days 7 and 15 were delivered to SKOV3 cells.

3.4.2.9.2. Ex vivo study

PLGA polybubbles with AuNRs in the shell were formed as described in 4.2.2 and 0.1 µL of 1 mg/mL acriflavine was injected in the middle. Polybubbles were incubated in 200 µL PBS and were laser activated for 5 minutes using 8A of 801 nm NIR laser once every two days. Supernatants were collected after each laser activation and were replaced with fresh PBS. On day 10, polybubbles were placed between a piece of bovine cartilage and 1cm meat. Fluorescence images were obtained before laser activation. 8A of 801 nm NIR laser was used to activate the sandwiched polybubble for 5 minutes. Fluorescence images were then obtained after laser activation. Fluorescence intensities in the polybubbles and the cartilage were quantified using Image J analysis.

3.4.2.10. Statistics

All the statistical analyses were performed using GraphPad Prism software (GraphPad Software, La Jolla, CA, USA). Triplicates for each group were used for all the *in vitro* studies. Student's t- tests were conducted between the control and experimental groups in **Figures 3.1d** and **3.6d**. Values were considered to be statistically significant if p-values were less than 0.05. One-way ANOVA was conducted between the three groups in **Figure 3.1h**. In the *in vivo* study conducted using laser-activated polybubbles, temperature change of the experimental group after laser activation are reported as average value from the independent triplicate values. For the control group, temperature change after laser activation are reported as average value from the technical triplicates. Temperature differences were analyzed using student's t-test and were considered statistically significant if p-values were less than 0.05.

4. CHARACTERIZATION OF CYTOCOMPATIBLE PAN/DEFECT-RICH MOS_2 NANOFIBERS FOR BIOMEDICAL APPLICATIONS

4.1. Introduction

Nanomaterials have unique size, shape, chemical, and anisotropic properties that are highly tunable. These materials can thus potentially be tuned to be used for various biomedical applications including biosensing, diagnostics, drug delivery, and catalysis[155, 156]. Dimensionality of the particles have also shown to alter the properties and functionalities of nanomaterials[157]. For example, one-dimensional (1D) carbon nanofibers have been studied extensively for their noteworthy thermal, mechanical, and electrical properties[158]. Carbon nanofibers are synthesized using two methods, namely vapor growth and spinning. Spinning methods results in high yield of nanofibers and is thus a preferred synthesis approach[159]. Polyacrylonitrile (PAN) is a precursor polymer that is widely used for spinning accounting for about 90% of manufactured carbon nanofibers[159]. PAN nanofibers (PNF) are also known for their high carbon yield, hydrophilicity, and stability[160]. Properties of PNF can be enhanced further for biomedical applications by incorporating two-dimensional (2D) transition metal-based nanofillers[161, 162].

Molybdenum disulfide (MoS_2) 2D nanostructures are promising transition metal dichalcogenides because of their unique chemical and optical properties. MoS_2 nanostructures have recently gained attention in biomedical applications including bioimaging[163], biosensing[164, 165], drug delivery[166, 167], and cancer theranostics[168, 169]. The potential use of MoS_2 in theranostics is due to their near-infrared (NIR) absorbance, efficient photothermal conversion, and high biocompatibility[170, 171]. MoS_2 structures were also found to degrade faster in conditions mimicking low hydrogen peroxidase biological environment. Superior biodegradability and biocompatibility make MoS_2 structures better candidates for biomedical applications compared to other 2D nanostructures[172]. 2D MoS_2 also possess high surface area making them useful for high drug loading and imaging modalities. In our recent studies, we have shown that hydrophobicity of MoS_2 can be increased by introducing atomic defects[173]. These defects were introduced by altering the ratios of the precursor solutions where higher sulfur content resulted in increased hydrophilicity of the MoS_2 structures. Increased hydrophilicity led to higher platelet activation illustrating the effects of atomic defects on cell adhesion that could potentially be leveraged in biomedical applications. Incorporating MoS_2 with the PNFs could thus improve mechanical strength and biocompatibility of the resultant nanostructures.

Electrospinning is a common and effective approach used to construct mechanically stable nanofibers with high specific surface area. Resulting membrane-like structure resembles that of extracellular matrices thus making it attractive option for biomedical applications[160, 174]. In this method, polymer solution is extruded using a syringe and high voltage is applied to the polymer droplet at the tip of the syringe. Surface tension then causes the formation of Taylor cone and when critical value of applied electrical potential is reached, jet of solution is ejected forming fibrous structures. In this paper, we synthesized defect rich MoS_2 by modulating different precursor ratios and characterized them extensively. We then combined different weight formulations of 1:5

MoS_2, with high surface area and superior optical properties, and PAN to create nanofibers using electrospinning. The biocompatibility of these fibers was then tested in human stem cells. This unique NIR-enabling composite scaffold can potentially be used for many biomedical applications including drug delivery, biosensing, and theranostics.

4.2. Results & Discussion

4.2.1. Characterization of Defect-rich MoS_2 Particles

Hydrophobicity of 2D MoS_2 nanostructures was modified by introducing atomic defects through modulation of precursor ratio of Mo and S. Morphology of the nanostructures were characterized using scanning electron microscopy (SEM). MoS_2 nanoassemblies with atomic defects had nanoflower structures and the "petal-like" morphology was increasingly prominent in ratios with increasing S precursor (**Figure 4.1A**). This exfoliated petal-like morphology results from the layering of nanosheets in the presence of atomic defects. This morphological trend with increasing S also increases overall surface area making these defect-rich MoS_2 nanoflowers an attractive option for biomedical applications like drug delivery.

Stability of MoS_2 nanoflowers was assessed by measuring their zeta potential which was observed to become increasingly negative with increasing S concentration (**Figure 4.1B**). Structural analysis of the nanoflowers to confirm the hexagonal atomic arrangements of Mo and S was carried out using X-ray diffraction (XRD) and X-ray photoelectron spectroscopy (XPS). Atomic defects with increasing S precursor was confirmed by the peak broadening in the 002, 100, 103 and 110 planes in XRD pattern (**Figure 4.1C**). Atomic defects could alter the d-spacing between the lattice planes. This increase in interlayer spacing likely caused further changes in diffraction angles consequently resulting in broader peaks.

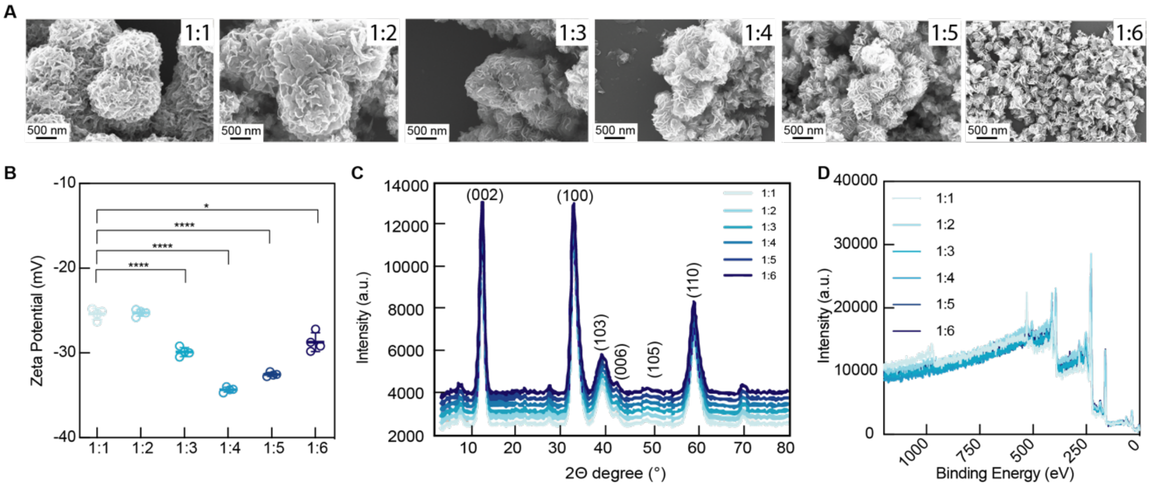

Figure 4.1 Synthesis of defect-rich MoS_2. A) SEM images of MoS_2 nanostructures with different precursor ratios shows more defined "petal-like" morphology in ratios with higher sulfur. B) zeta potential of MoS_2 nanostructures with different precursor ratios shows increasing negative charge in ratios with higher sulfur. C) XRD pattern shows 2H phase present in the MoS_2 lattice for different Mo:S ratios D) XPS spectra of MoS_2 nanostructures with different precursor ratios exhibiting the binding energies of Mo and S

The chemical state of the MoS_2 nanoflowers was further investigated using XPS peaks (**Figure 4.1D**). The XPS peaks were then deconvoluted to identify the binding energies of Mo and S atoms (**Figure 4.2A**). Binding energies of Mo^{4+} $3d_{5/2}$, Mo^{4+} $3d_{3/2}$, S^{2-} $2p_{3/2}$, S^{2-} $2p_{1/2}$ for nanostructures with 1:4, 1:5, and 1:6 precursor ratios are listed in (**Figure 4.2B**). Difference in binding energies of Mo^{4+} $3d_{5/2}$ and $3d_{3/2}$ were $\Delta = 3.20$ eV, 3.10 eV and 3.15 eV for nanoflowers with 1:4, 1:5, and 1:6 precursor ratios, respectively. This further supports the presence of dominant 2H phases in the nanoflowers with high sulfur content resulting in a hexagonal arrangement with a defect. Optical properties of these nanostructures were also analyzed to assess their potential use in biomedical imaging and theranostics. Based on the characterization results described above, MoS_2 with 1:4, 1:5, and 1:6 precursor ratios are observed to have similar physical and chemical characteristics. However, well-resolved, petal-like, morphology is more prominent in the nanoflowers formed using 1:5 compared to that of 1:4 and 1:6 (**Figure 4.2C**). Favorable atomic defects in 1:5 MoS_2 results in this highly porous morphology with increased surface area that could in turn be beneficial for various biomedical applications. Absorption intensity was increased in the UV and NIR wavelengths along with a slight red shift for 1:5 MoS_2 compared to that of 1:4 and 1:6 MoS_2 nanostructures (**Figure 4.2D**). This enhanced absorption highlights the superior optical activity of 1:5 MoS_2 nanostructures. Crystalline structures of these two ratios with respect to atomic defects were further studied using Raman spectroscopy (**Figure 4.2E**). MoS_2 crystalline nanostructures are layers of covalently bonded MoS_2 molecules held by van der Waals forces. In this arrangement, Mo atoms can be coordinated using S atoms in two geometries: trigonal prismatic and octahedral. Raman spectra of the three ratios indicate that the E_{2g} peaks (270 cm^{-1}) indicative of the octahedral coordination were absent in 1:4 ratio but were similar in 1:5 and 1:6 ratios. E^1_{2g} and A_{1g} peaks indicative of the trigonal prismatic coordination had higher intensities in 1:5 ratio compared to the other two ratios. These differences in Raman shifts are indicative of S-dependent atomic defects in the three ratios consequently leading to the observed differences in morphologies. Additionally, peak intensity ratios of A_{1g}/ E^1_{2g} were found to be increased in nanoflowers with 1:5 precursor ratio (1.55) compared to that of 1:4 ratio (1.2) and 1:6 ratio (1.4). This observation further confirms the increased crystal layer thickness in 1:5 MoS_2 nanoflowers as the interlayer van der Waals interactions were optimal with this precursor ratio.

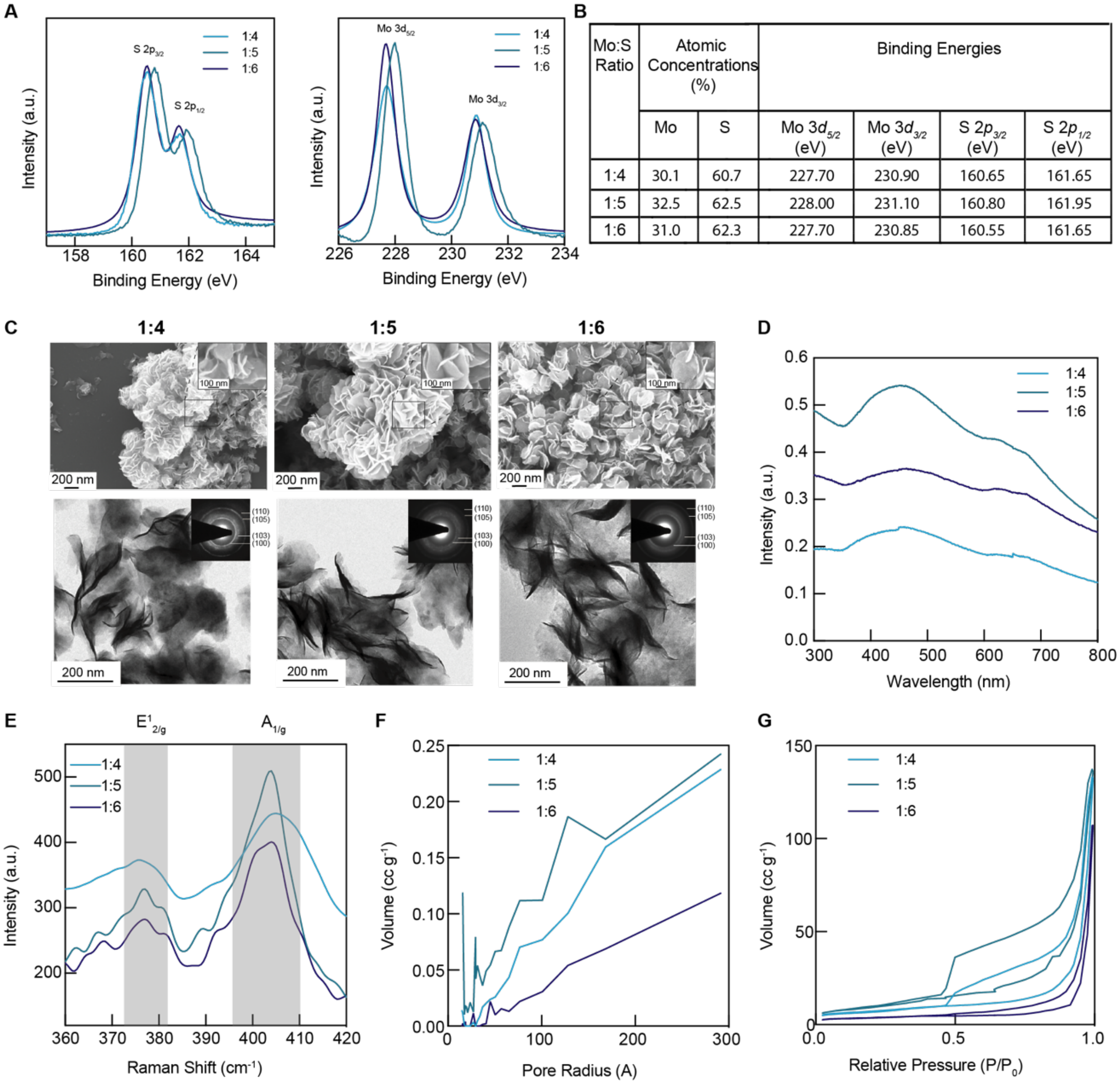

Mo:S Ratio	Atomic Concentrations (%)		Binding Energies			
	Mo	S	Mo $3d_{5/2}$ (eV)	Mo $3d_{3/2}$ (eV)	S $2p_{3/2}$ (eV)	S $2p_{1/2}$ (eV)
1:4	30.1	60.7	227.70	230.90	160.65	161.65
1:5	32.5	62.5	228.00	231.10	160.80	161.95
1:6	31.0	62.3	227.70	230.85	160.55	161.65

Figure 4.2 MoS_2 with high sulfur precursor content. A) Deconvoluted XPS spectra of 1:4, 1:5 and 1:6 MoS_2. **B)** Atomic concentrations and peak positions of MoS_2 with 1:4, 1:5 and 1:6 precursor ratios from deconvolution of XPS peaks in A. **C)** SEM and TEM images highlight the morphological differences in 1:4, 1:5 and 1:6 MoS_2 nanoflowers. "Petal-like" structure is more defined in 1:5 MoS_2 compared to that of 1:6. **D)** Absorbance spectra indicates increased absorbance in the ultraviolet (UV) and near-infrared (NIR) region for 1:5 MoS_2 nanoflowers based on the higher peak intensity. **E)** Raman spectroscopy also shows increased intensity of signature peaks for 1:5 MoS_2. **F)** Pore distribution analysis shows increased high pore volume for MoS_2 with 1:5

precursor ratio (0.25 cc g^{-1}). **G)** Overall surface area was also found to be higher in 1:5 MoS_2 nanoflowers (145 cc g^{-1}).

Surface area and porosity of MoS_2 assemblies formed using higher precursor ratios were analyzed to select the MoS_2 nanoassemblies with optimal surface properties for biomedical applications. The adsorption-desorption isotherm of different ratios of MoS_2 samples, their respective surface areas and Barrett-Joyner-Halenda (BJH) pore radius results with inset of pore size distributions were shown in **Figures 4.2F** and **4.2G** respectively. The Brunauer-Emmett-Teller (BET) and pore size distribution figures of MoS_2 show that the materials are type V isotherms with hierarchical pore structure. Particularly, the MoS_2 with 1:5 ratio showed a better pore size distribution with hierarchical pores and maximum pore volume of 0.208 cc g^{-1}. Also, it possesses high surface area (33.976 m^2/g) comparatively, which supply more active sites, added advantage for biomedical applications including biosensing, bioimaging, and drug delivery. Additionally, the combination of micro and meso pores in MoS_2 (1:5), provides efficient channels for mass transport and facilitate interface contact between the catalyst and biological molecules.

4.2.2. Characterization of MoS_2/PAN Nanofibers

Defect-rich 1:5 MoS_2 nanostructures could potentially be used to improve the mechanical properties and cytocompatibility of carbon nanofibers, such as PAN, specifically for biomedical applications. Based on the previously described morphological and chemical characterizations of MoS_2 nanostructures with different precursor ratios, 1:5 ratio with increased surface area was chosen to synthesize the PAN/MoS_2 nanofibers.

Electrospinning was used to fabricate these PAN nanofibers with 0 wt. %, 2 wt. %, 4 wt. %, and 8 wt. % of 1:5 MoS_2 (**Figure 4.3A**). Morphology of these fibers were assessed using SEM (**Figure 4.3B**). This study demonstrated bead formation within the nanofibers wherein there was an increase in size and number of beads formed within the nanofibers with increasing wt. % of MoS_2. Overall diameters of nanofibers were also observed to increase with increasing weight percentages of MoS_2 (**Figure 4.3C**). Functional groups in the PAN nanofibers were identified using FTIR spectroscopy in the range of 700 - 4000 cm^{-1}. A sharp peak was observed at 1680 cm^{-1} is attributed to the -C=N stretching of the imine bond in the stabilized PAN/MoS_2 nanofibers (**Figure 4.3D**). The peak intensity is observed to increase with increasing MoS_2 concentration in the nanofibers demonstrating the interaction between MoS_2 nanosheets and PAN. Defect-rich MoS_2 provides active sites that are electron deficient, which in turn likely results in an interaction with the imine bond leading to the formation of $-C=N^{+}$[175]. Thermal stability of the PAN nanofibers with varying wt. % of MoS_2 was assessed using differential scanning calorimetry. PAN nanofibers were observed to have a melting temperature (T_m) of 296°C which increased up to 310 °C with incorporation of MoS_2 (**Figure 4.3E**). This increase in T_m of PAN nanofibers with MoS_2 indicates the possible covalent interaction between PAN and MoS_2 further improving the stability of the nanofibers.

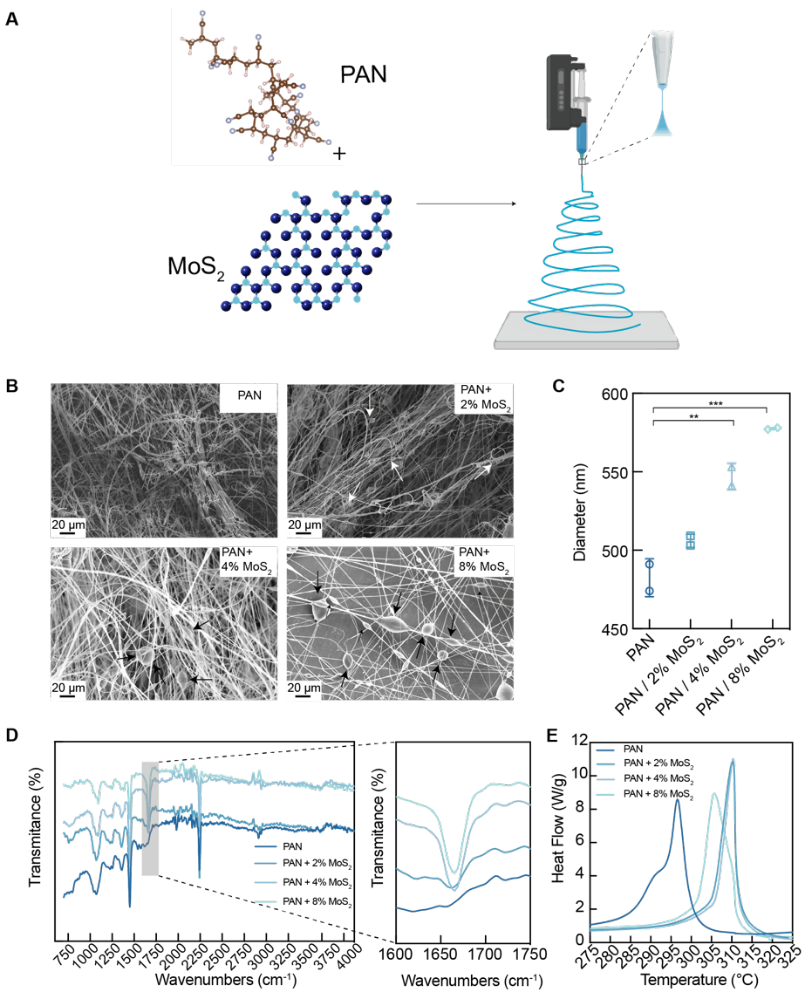

Figure 4.3 Electrospun PAN and defect-rich MoS$_2$ nanofibers. A) Scheme outlining the formation of electrospun PAN nanofibers with 1:5 MoS$_2$ nanoflowers. **B)** SEM images of PAN nanofibers show increasing number of bead-like structures with increasing MoS$_2$ concentration. **C)** Diameter of the beads are also observed to be increasing with increasing MoS$_2$ concentration. **D)** FTIR spectra shows a sharp peak around 1680 cm^{-1} indicating a signature peak of MoS$_2$ with increasing concentration of MoS2 in PAN nanofibers. **E)** DSC curves indicates improved thermal stability of the PAN nanofibers with the incorporation of MoS$_2$ nanoflowers.

4.2.3. Mechanical and Electrical Characterization of MoS$_2$/PAN nanofibers

Effect of MoS$_2$ nanostructures on the mechanical strength of the PAN nanofibers was assessed by studying tensile strength for each composition. Incorporation of defect-rich 1:5 MoS_2 resulted in increased tensile strength and yield stress of PAN nanofibers (**Figure 4.4A**). This observation is likely due to the strong interactions between MoS_2 and PAN as confirmed by the introduction of sharp peak at 1680 cm^{-1} in FTIR spectra. Increasing concentration of MoS_2 nanostructures improved the tensile properties of PAN nanofibers until 4 wt% of MoS_2. Tensile strength of the PAN nanofibers seems to decrease at 8 wt% MoS_2 and is likely due to the effect of increased accumulation of MoS_2 assemblies along the nanofiber further reducing the mechanical stability of the fibers. Hydrophilicity of the PAN nanofibers were also assessed by measuring water contact angle to assess the potential changes in cell adhesion and protein adsorption. PAN nanofibers were observed to become more hydrophilic with the incorporation of defect-rich 1:5 MoS_2 nanostructures (**Figure 4.4B**). Although PAN nanofibers were porous, water droplets were absorbed by PAN without MoS_2 after 2 seconds. In contrast, water droplets were absorbed after 1 second when placed on top of the MoS2-incorporated PAN nanofibers indicating enhanced hydrophilicity of the nanofibers. Additionally, assessment of initial contact angle of water droplets on the four types of nanofibers support this observation of increased hydrophilicity (**Figure 4.4C**). Initial water contact angle was observed to be higher (114 ± 6°) in PAN nanofibers without MoS_2 compared to lower contact angles observed in PAN nanofibers with 2 wt% (102 ± 3°), 4 wt% (103 ± 4°), and 8 wt % (102 ± 4°) MoS_2. These water contact timing and angle observations indicates that hydrophilicity of PAN nanofibers can be tuned with the incorporation of defect-rich MoS_2 further influencing cell adhesion properties.

Electrical properties of MoS_2/PAN nanofibers were evaluated using electrochemical impedance spectroscopy (EIS) with increasing MoS_2 concentration. EIS measurements were carried out in the frequency range of 0.1 kHz to 1000 kHz in 0.1 M PBS at open circuit potential with AC perturbation of 10 mV via the silver-based 2-probe set up. Impedance measurements showed that all the PAN nanofiber samples with or without MoS_2 possess charge transfer resistance. The Bode plot indicates that impedance decreases with increasing MoS_2 concentration within the PAN nanofibers (**Figure 4.4D**). This decline in impedance seems to reach its minimum with the incorporation of 4% MoS_2 as impedance at higher frequency of 1kHz indicates no significant difference in impedance between nanofibers with 4% MoS_2 and 8% MoS_2 (**Figure 4.4D**). Defect-rich MoS_2 likely decreased the charge transfer resistance as the vacancies in the 1:5 MoS_2 potentially aiding in transfer of charge and thus flow of current. This decrease in impedance shows that incorporation of MoS_2 results in higher conductivity. Additionally, Bode phase shift plots supported this trend of decreasing impedance with increasing MoS_2 as the PAN nanofibers with higher MoS_2 % plateaued closer to 0°, which is indicative of resistive response of supercapacitors. These findings thus suggest that incorporation of 4% MoS_2 can result in the optimal improvement of the electrochemical properties of PAN nanofibers.

Cyclic voltammetry (CV) was also performed on the nanofibers that were placed in 0.1 M PBS at the scan rates of 100 mVs^{-1}. Emergence of anodic and cathodic peak potentials can be observed in PAN nanofibers that were incorporated with MoS_2 (**Figure 4.4E**). These oxidative and reductive peaks at 0.08 V and -0.16 V, respectively, indicate that redox reactions are occurring in the electrodes in the presence of defect-rich MoS_2.

Specifically, these reversible redox peaks give rise to a parallelogram shape of the voltammetry, deviation from an otherwise rectangular shape that is characteristic of pseudocapacitance. As described in previous studies, incorporation of electroactive metal particles could result in enhancement of specific capacitance of carbon-based materials [176, 177]. This hypothesis was supported by the results from CV as specific capacitance values were observed to be 12.2, 17.7, 15.2, 16.7 μF/g for PAN, PAN/2% MoS_2, PAN/4% MoS_2, and PAN/8% MoS_2, respectively (**Figure 4.4F**). This enhanced pseudocapacitive charge storage in PAN/MoS_2 nanofibers is a result from faradic current resulting from oxidation and reduction of MoS_2. Overall current magnitude of the peak also increased with increasing MoS_2 concentration resulting from increased electron transfer indicating further highlighting the pseudocapacitance behavior of PAN/MoS_2 nanofibers. Enhanced electrochemical property of PAN/MoS_2 thus paves way for potential use of these nanofibers in biomedical applications including biosensing and electrochemical sensing.

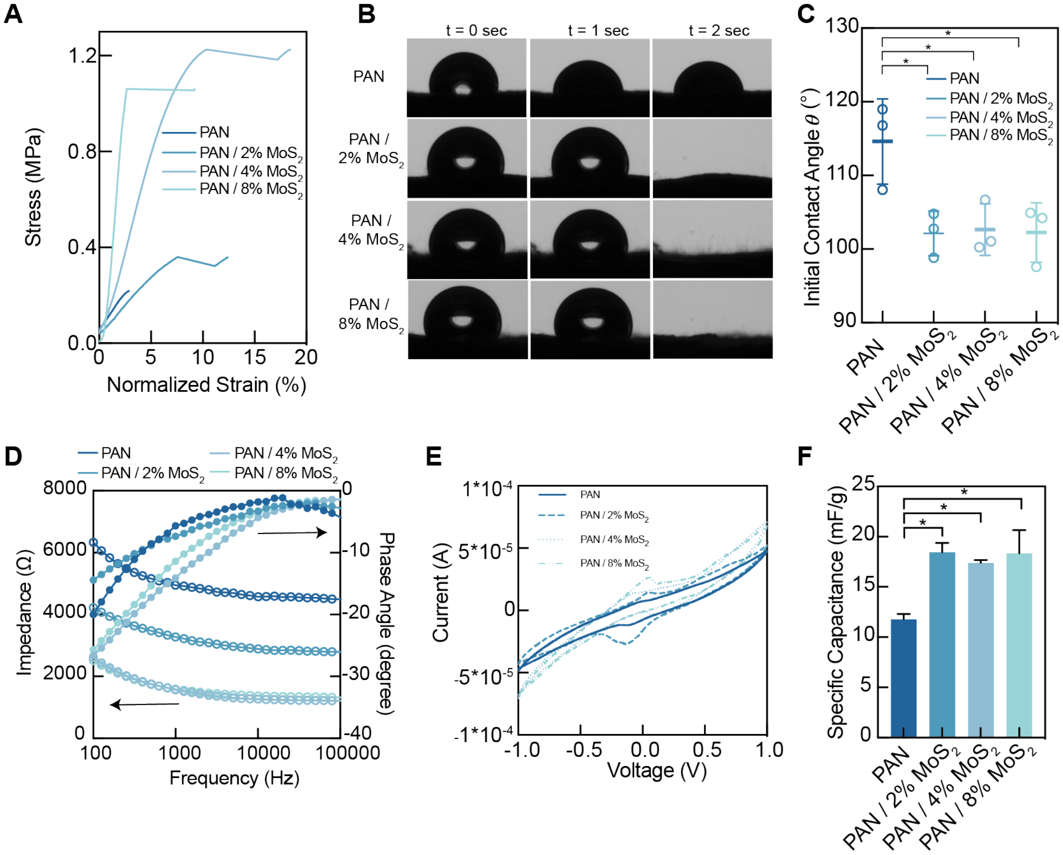

Figure 4.4 Mechanical and Electrical Properties of MoS_2/PAN Nanofibers. A) Stress-strain curves of PAN nanofibers indicates increasing tensile strength of nanofibers with incorporation of MoS_2 nanostructures. **B)** Water contact angles of PAN at 0, 1, and 2 seconds indicating increased hydrophilicity with MoS_2 nanostructures. **C)** Initial water contact angle (at t = 0 seconds) of PAN nanofibers shows that contact angle decreased in nanofibers with MoS_2. **E)** Bode plot of PAN nanofibers demonstrates decrease in impedance and increase in phase angle corresponding to improved conductivity with increasing MoS_2. **F)** Cyclic voltammetry (CV) measurements of PAN nanofibers showing emergence of pseudocapacitive behavior with respect to increased MoS_2. **G)** Increase in specific capacitance in PAN nanofibers due to the faradaic reactions after the incorporation of MoS_2 further validates the electrochemical potential of defect-rich MoS_2.

4.2.4. Cytocompatibility of MoS_2/PAN Nanofibers

Human mesenchymal stem cells (hMSCs) have been extensively used in tissue engineering because of their proliferation and differentiation potential. Microenvironment of these cells dictate the path of differentiation and thus biomaterials with external stimuli mimicking that of extra cellular matrix are used to support the growth of hMSCs. We thus investigated cell viability and adhesion of hMSCs onto the electro spun nanofibers. Cells were seeded on top of the PAN/MoS_2 nanofibers with varying wt. % of MoS_2. Viability of hMSCs on days 1, 3, and 7 were assessed using alamar blue assay (**Figure 4.5A**). Viability was reduced to ~ 50 % when hMSCs were incubated for 24 hours on nanofibers with PAN and 0 wt. %, 2 wt. %, 4 wt. % MoS_2. Cells incubated with PAN nanofibers with 8 wt. % MoS_2 showed significant reduction in viability of ~ 35 %. However, cell viability significantly improved with longer incubation period. PAN with 4 wt. % MoS_2 showed increased viability on days 3 (***, $p < 0.001$) and 7 (*, $p < 0.05$) compared to that of PAN without MoS_2. In addition to cell viability, we also investigated the presence of reactive oxygen species (ROS) in the cells was also investigated. ROS have been observed to increase during cellular environmental stress triggered, cell destructive pathways including apoptosis. ROS assay indicated that ROS concentration in the cytoplasm was lower in hMSCs incubated with PAN/MoS_2 nanofibers compared to that of PAN nanofibers (**Figure 4.5B**). This shows the ability of MoS_2 to improve cytocompatibility of the PAN nanofibers paving the way for safe use of these nanofibers in biomedical applications. Adhesion and morphology of hMSCs were also assessed using nuclei and actin dyes after hMSCs were seeded onto the PAN nanofibers with and without MoS_2. Fluorescence images of hMSCs indicated that cell adhesion and proliferation improved in PAN nanofibers with MoS_2 compared to that of PAN nanofibers (**Figure 4.5C)**. In addition to proliferation, actin staining indicated elongated morphology of PAN nanofibers with and without MoS_2. These cell studies combined with the mechanical properties prove that cytocompatibility of PAN nanofibers can be improved with the incorporation of 4 wt% MoS_2 and can thus be used for biomedical applications.

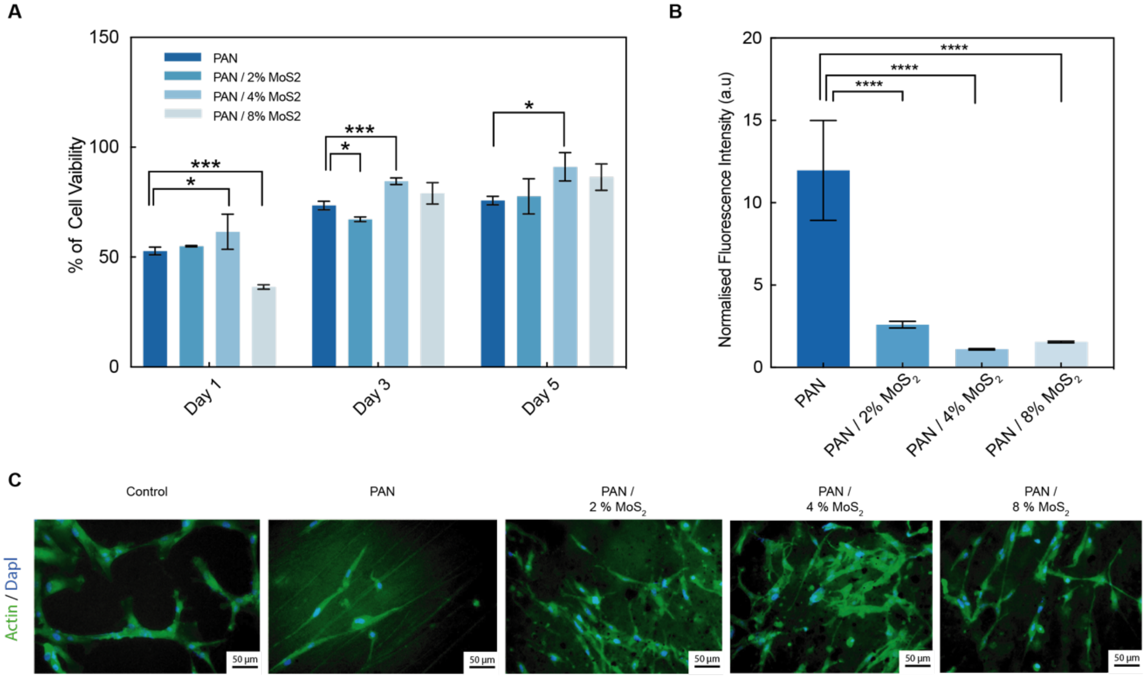

Figure 4.5 Cytocompatibility of PAN/MoS_2 Nanostructures. A) Alamar Blue assay was used to assess proliferation of hMSCs on PAN/MoS_2 scaffolds. Proliferation of hMSCs significantly increased when seeded on PAN scaffolds with 4% MoS_2 on days 1, 3, and 5. The data represent mean – standard deviation (n = 3, ANOVA $*p < 0.05$, $***p<0.001$). **B)** Reactive oxygen species (ROS) in the hMSCs seeded on PAN/MoS_2 nanofibers were quantified. Significant reduction in ROS produced within the hMSCs were observed on PAN/MoS_2 nanofibers compared to that of PAN nanofibers. **C)** Actin and nuclei staining showed that hMSCs readily attached and spread on PAN/MoS_2 nanofibers compared to that of PAN nanofibers 5 days after seeding. No significant differences in cellular attachment and elongation were observed with respect to wt. % of MoS_2.

4.3. Conclusion

Carbon nanofibers, like PAN fibers, are promising candidates for biomedical implants and scaffolds due to their beneficial mechanical properties and biocompatibility.

The properties of these fibers can further be optimized with use of metal nanoparticles such as MoS_2. We successfully fabricated and characterized defect-rich MoS_2 nanoflowers by modifying the precursor ratios. MoS_2 nanoflowers with precursor 1:5 ratio (Mo:S) was found to have a "petal-like" morphology with high surface area. This 1:5 MoS_2 nanoflower was combined with PAN to form nanofibers using electrospinning. Successful incorporation of MoS_2 resulted in increase in diameter of PAN nanofibers. Furthermore, cytocompatibility of PAN nanofibers was improved in the presence of MoS_2 nanoflowers through increased hMSC adhesion and proliferation. These unique characteristics of PAN/MoS_2 nanofibers can thus be potentially used in biomedical applications including imaging, theranostics, and tissue engineering.

4.4. Experimental Section

4.4.1. Synthesis of MoS_2

Potentially scalable, simple and cost-effective hydrothermal technique was employed to synthesis defect-rich Molybdenum disulfide (MoS_2) solutions using precursor solutions, 1mmol of hexammonium hepta molybdate tetra hydrate ($(NH_4)_6 Mo_7O_{24}. H_2O$) (Mo) (Alfa Aesar, USA) and 7mmol of thiourea (CH_4N_2S) (S) (Alfa Aesar, USA). Mo and S precursors (1:1 ratio) were dissolved in deionized (DI) water and then subjected for magnetic stirring about 30 min. In the next step, the homogeneous solution was transferred into a Teflon lined stainless steel autoclave and heated at 220 °C for 18 h. Once the reaction was completed, the solution was collected, cooled and washed with deionized water and ethanol for three times. The as- formed MoS_2 product was then dried under vacuum at 50 °C for 2 days. Similarly, MoS_2 solutions with different Mo:S precursor ratios (1:2, 1:3, 1:4, 1:5 and 1:6) were also synthesized.

4.4.2. Electrospinning of MoS_2/PAN Nanofiber Mats

The as-synthesized and as-screened MoS_2 (1:5) was used as precursor material for preparing the electrospun fiber mats. The polyacrylonitrile (PAN, average M_W 150 000), purchased from Alfa Aesar, USA, was used as polymer support for nanofiber mats preparation. Different weight ratios of MoS_2 such as 2%, 4 %, 6 %, and 8 % with respect to PAN polymer (9 wt. %) were used for nanofiber mat preparations. The PAN polymer was dispersed in 20 mL of *N,N*-dimethylformamide (DMF) ((Merck, USA) for 30 minutes at 70 °C for thorough mixing. Then the MoS_2 with different wt. % ratios were added into the finely dispersed PAN polymer solution and kept it for magnetic stirring for 12 h at room temperature. After that the polymer solution was transferred to a 20 mL syringe to carry out electrospinning, wherein the flow rate was set at 1 mL/hr. The distance between the tip of the syringe needle and the aluminum foil collector was set to 12 cm and applied voltage was set at 12 kV. Finally, the as-spun MoS_2/PAN nanofiber mats were collected from the aluminum foil, vacuum dried at 50 ^{o}C for 48 h, and subjected for stabilization at 300 ^{o}C in muffle furnace, with a ramp rate 1°C min^{-1} to remove the solvent.

4.4.3. Characterization of MoS_2/PAN Nanofiber Mats

Scanning electron microscope (SEM) was used to characterize morphology of MoS_2, PAN, and MoS_2-PAN (FESEM, Quanta 200, Zeiss, Germany). Transmission electron microscopy (TEM) images were collected using TEM Tecnai 20 G^2 STWIN, USA at 200 kV. Zeta potential of MoS_2 nanoparticles were obtained using Zetasizer

(Malvern Instruments, UK). X-ray diffraction (XRD) patterns were collected using X'Pert Pro, PAN analytical, Netherlands with Cu Kα radiation (λ= 1.5406 Å). Absorbance of MoS_2 nanoparticles was characterized using plate reader (Varian Cary 50 Bio UV-Vis Spectrophotometer (USA)). Raman spectra was used to confirm the composition of the MoS_2 nanoparticles. MoS_2 powders (1:1 to 1:6) were placed on glass slides and were excited by 532 nm green laser to obtain Raman spectra (WiTec, Germany using laser light of 532 nm wavelength). X-ray photoelectron spectroscopy (XPS) analysis was conducted using PHI 5000 Versa Probe II, FEI Inc. spectrometer. The binding energy values of all the samples were referenced to C 1s hydrocarbon peak at 284.6 eV. The diameter of fibers was calculated using ImageJ software. The surface and textural properties of MoS_2 nanoparticles were characterized by N2 adsorption–desorption isotherms, measured at 77 K using Quantachrome Autosorb iQ-MP/iQ-XR. Brunauer–Emmett–Teller (BET) equation was used to calculate the surface area and pore size of the respective MoS_2 nanoparticles. Pore size distribution (PSD) curves were plotted based on the Barrett–Joyner–Halenda (BJH) method.

Infrared spectroscopy was carried out on the PAN nanofibers using FTIR spectrometer (FTIR Bruker ALPHA-Platinum) in the range of 4000-600 cm^{-1}. Thermal properties of MoS_2/PAN nanofiber mats were assessed using differential scanning calorimetry (DSC Q10) under continuous nitrogen flow. Samples were heated from 40 °C to 350 °C at a heating rate of 8 °C/min. Surface wettability of the PAN nanofibers were investigated by measuring water contact angle using a goniometer (KSV Instruments CAM 200). A drop of 4 μL of water was dropped on the surface of the nanofibers with varying concentrations of defect-rich MoS_2 nanostructures. Frames were recorded at 1 second intervals immediately after dropping the water bead. Contact angles were then measured using the software and were averaged for triplicates of each sample. Mechanical properties of the nanofibers were assessed using the tension clamp in the dynamic mechanical analyzer (DMA Q800). The nanofiber mats with varying concentration of defect-rich MoS2 were cut into a rectangular shape (7mm × 6mm) with thickness of 0.3mm. Stress-strain curves were obtained at room temperature with a force ramp rate of 0.3 N/min.

4.4.4. Cell Viability and Oxidative Stress Studies

Human mesenchymal stem cells (hMSCs) were cultured using α-MEM media (Gibco) with 10 % fetal bovine serum and 1 % penicillin/streptomycin in high humidity at 37 °C and 5 % CO_2. The hMSCs were sub-cultured at 75% confluency and were used before passage 5 using trypsin. MoS_2/PAN nanofibers (2 wt%, 4 wt%, 6 wt%, and 8 wt%) were sterilized using 70% ethanol for 30 minutes followed by 3 PBS washes with 1 hour between the washes. Cells were then seeded on the MoS_2/PAN nanofibers assembled in two 96-well plates at a density of 5000 cells/well. After 24 hours, cell viability was assessed using Alamar Blue Assay (Invitrogen) based on the manufacturer's protocol. In the other 96-well plate, cellular oxidative stress was assessed using 5 μM CellROX reagent (Invitrogen) based on the manufacturer's protocol.

4.4.5. Cell Morphology Studies

Cell morphology was characterized using fluorescence microscopy to observe actin arrangement and nuclei. Nanofibers seeded with hMSCs were fixed with paraformaldehyde for 10 minutes 72 hours after seeding and was followed by 5 minutes PBS washes twice. Cells were then permeabilized using 0.5% Triton X for 10 minutes and was also followed by 2 PBS washes. Actin cytoskeleton of the cells was stained using 25 vol % of Alexa Fluor-594 phalloidin (Abcam) and nuclei was stained using (2'-[4-ethoxyphenyl]-5-[4-methyl-1-piperazinyl]-2,5'-bi-1H-benzimidazole) (Hoechst) (Life Technologies). The fluorescence images were obtained using Zeiss Axio Vert.A1.

5. DRUG-ELUTING SHAPE MEMORY FOAM AS AN ADJUVANT TO BREAST CANCER SURGERY

5.1. Introduction

In 2021, about 16.9 million people are projected to be diagnosed with cancer and 608,570 will likely die of cancer [178]. In particular, breast cancer has the highest mortality in women compared to any other cancer and is estimated to cause deaths of ~43,600 women in 2021 in the United States alone [74, 179]. For early-stage breast cancer, surgical removal of the tumor is the primary clinical interventions with or without reconstruction. Although initially effective, tumor recurrences are observed in 30% of breast cancer patients even without the presence of cancer cells in the lymph nodes [180]. This recurrence could result from the physiological post-operative stress or residual cancer cells lingering near the surgical site leading to micrometastases [181]. Surgical removal of the tumor is usually accompanied with the removal of a portion of the surrounding tissue to eliminate residual cancer cells. Surgery is also followed by the administration of high-dose chemotherapy to reduce chances of recurrence [182]. Both these approaches help reduce the number of residual cells near the surgical site but have certain limitations: 1) current imaging techniques used during surgery cannot provide precise boundary of cancer cells to ensure that a clean surgical boundary is achieved, and 2) non-targeted chemotherapy often results in less therapeutic efficacy and high cytotoxicity. Another challenge with the surgical approach is the closure of the tissue void that is created after the tumor resection. Conventionally, degradable or non-degradable sutures are used to close the tissue void but are associated with challenges that has prevented widespread clinical adoption [183]. Thus, there is a growing interest in developing novel drug delivery platforms to precisely seal the tissue void while therapeutically impeding the development of metastasis.

Variety of materials have been developed to enable localized and controlled release of chemotherapeutic agents while closing the post-surgical void. Drug-eluting sutures were designed using degradable polymers like poly (lactic-co-glycolic acid) (PLGA) because of their tunable degradation and drug release kinetics [184]. Although the absorbable sutures can enable chemotherapeutic release, there are several challenges including shorter release timing, limited control over drug dosage, delayed wound healing, and mechanical instability. Polymers like PLGA are hydrolytically cleavable and this hydrolytic degradation is expedited in the human body because of the presence of enzymes [185]. This could result in result in faster reduction in tensile strength of the absorbable sutures causing: 1) pre-mature rupture of suture leading to delayed wound healing and 2) accidental dose dumping resulting in adverse side effects. It is also important to note that most of the absorbable sutures are designed for complete dissolution within a couple of weeks. This in turn imposes shorter drug release time and lower drug dosage to avoid cytotoxicity. To ensure that the dormant cancer cells are killed, long-term sustained release of chemotherapy is often preferred. Hence, there was a shift in focus towards injectable or implantable biomaterials with longer degradation rates and sealing capabilities.

Drug-loaded hydrogels have been developed as an alternative adjuvant strategy because of their highly porous structure and tunable mechanical properties [89]. Hydrogels can also be formed *in situ* to enable better sealing of the surgical void. Additionally, small molecule hydrophilic drugs can be loaded in high density owing to the swelling property of the hydrogels. Biocompatible and biodegradable hydrogels like hyaluronic acid (HA) has been successfully used to encapsulate chemotherapeutic drugs like doxorubicin (DOX) and gemcitabine [186]. Although controlled release of the drugs was achieved using the HA gels *in vitro*, earlier drug release was observed *in vivo* likely due to the expedited degradation in the presence of enzymes. Poor *in vitro*- *in vivo* correlation of drug-loaded hydrogels could result in unpredictable release profile and possibly compromising desired therapeutic outcomes. Another limitation with the use of hydrogels involve lower and non-homogenous drug loading observed with hydrophobic drugs [187]. This is especially relevant for chemotherapy because there are a large number of the anti-cancer agents that are hydrophobic. Furthermore, hydrogels often have low tensile strength that could result in gels being slipped away from the resection site after implantation causing off-target chemotherapeutic delivery further leading to cytotoxicity. These challenges with ineffective sealing and drug delivery could potentially be solved with the use of biomaterial scaffolds.

Biomaterial scaffolds are often polymer-based with tunable chemical and physical properties. Unlike sutures and hydrogels, scaffolds are mechanically stable to be implanted at the resection site [94]. Premature drug release can also be potentially avoided as polymer-based scaffolds have a well-studied and controllable degradation rates both *in vitro* and *in vivo*. Additionally, shape and properties of the scaffold can be precisely engineered in a reproducible manner because they are pre-formed unlike *in situ* hydrogels. These pre-formed scaffolds can be non-degradable or degradable. With non-degradable implants, drug release can be controlled and concerns over by products can be avoided. However, non-degradable implants have to be surgically removed which can result in complications involving formation of fibrous tissue over the scaffold. Hence, developing degradable polymers with biocompatible by products are preferred [188]. Gliadel wafer is a biodegradable polyanhydride scaffold loaded with chemotherapeutic drug called carmustine and has been very successful in reducing recurrence rate of glioblastomas [189]. These wafers are placed in the brain cavity that is left after tumor resection and facilitate continuous release of carmustine for 2 to 3 weeks. Median survival of glioblastoma patients increased by 41% with the use of Gliadel wafers [190]. Despite the promising potential of the drug-loaded biomaterial scaffold, there are several limitations. Pre-formed degradable scaffolds often have a solid-form that has limited malleability, which is not ideal for precisely sealing irregular post-surgical cavity that is often observed in breast cancer patients [186]. There is thus a need for novel controlled delivery platform that can precisely adapt and seal the irregular tumor cavity.

In this study, we introduce a tissue-void filling and drug-eluting shape memory polymer (SMP) foam. SMP foam used in this study is the reaction product of HPED, TEA, and 2,2,4-trimethyl hexamethylene diisocyanate (TMHDI) [191]. This combination of monomers that was previously developed by our group has resulted in a highly porous foam that has previously been included as a component in a CE-approved neurovascular embolization device [192]. These favorable surface properties can be leveraged for improved drug loading for drug delivery applications. Specifically, controlled delivery of the loaded drugs from the SMP foams can also be achieved by initiating drug release through SMP foam actuation at body temperature. Two naturally fluorescent drugs, anti-septic drug called acriflavine (Acri) and chemotherapeutic drug called doxorubicin (DOX) were used as cargo to coat the SMP foams. We also incorporated viscosity modulating agent, polyvinyl alcohol (PVA), to improve drug loading onto the foam and modulate release profiles. from reticulated and non-reticulated TMHDI foam. Increased drug loading and controlled drug release was accomplished *in vitro* using this platform. Additionally, functionality of the released drug was also successfully maintained post release. Previous studies have shown that SMP foams also enables enhanced wound healing. By combining this property with drug loading and precise sealing, SMP foams can be potentially used clinically to reduce breast cancer recurrence.

5.2. Results & Discussion

5.2.1. Drug-loaded SMP foams

Low density SMP foams were synthesized using gas blowing procedure to result in uniform porous internal structure. This method has been previously shown to be effective in fabricating controllable low-density crosslinked foams [193]. Resultant structure is a foam with pores that are isolated by thin membranes. These membrane pores can be disrupted using mechanical reticulation techniques to yield interconnected open pores that could potentially lead to better cellular infiltration after implantation [194, 195]. Additionally, viscosity-modulating agents, like polyvinyl alcohol, have been widely used to increase drug contact time with the muchoadhesive membrane for oral drug delivery formulations [196, 197]. This principle was used to improve drug loading onto the foams. To this end, both reticulated and non-reticulated HD80 SMP foams were loaded with a model small molecule drug, Acri, mixed with varying concentrations of PVA. Release studies were then conducted by incubating the drug-loaded foams in PBS at 37 °C to enable actuation (**Figure 5.1A**). The results indicated that overall drug release increased with increasing PVA concentration supporting the initial hypothesis about the role of viscosity modulating agents. Higher PVA concentration (3%, 10%) resulted in ~4 times more drug release in both non-reticulated and reticulated HD80 foams compared to foams with no PVA (**Figure A5**). Another interesting distinction that was observed regarding drug loading is that non-reticulated foams enabled higher total drug release with or without PVA compared to that of reticulated foams. Drug release improved up to 40% in non-reticulated foams with 10% PVA indicative of higher drug loading. The cell membranes present between the pores likely provides additional surface area on the foams to be coated by the drug solution. This potentially results in higher drug loading on non-reticulated foams further leading to higher drug release.

Promising results from the release studies indicating improved drug loading with model drug, Acri, led to the incorporation of chemotherapeutic drug loading onto the foams. DOX is a naturally fluorescent chemotherapeutic agent that is commonly used in treating many cancers including breast cancer. Doxorubicin has a logP value of 1.3 indicating that it is more hydrophobic compared to that of Acri with logP value of -2.8 [198, 199].Thus, DOX loading could potentially be improved with the use of hydrophobic foams. Additionally, our previous studies have shown that moisture content in SMP foams can impede foam actuation [194]. Using a more hydrophobic foams like trimethylhexamethlyene diisocyanate (TMHDI) has shown to restrict moisture uptake further improving actuation efficiency. For these combined reasons, DOX was loaded onto non-reticulated TMHDI foams with varying PVA concentrations. DOX uptake onto the TMHDI foams were initially characterized using light microscopy (**Figure 5.1B**). The drug-loaded foams were cut in half to study the drug distribution in exterior and interior surface of the foams. Increasing drug loading is observed in the outer surface of the foams with increasing PVA concentration as hypothesized earlier. Although drug penetration in the core of TMHDI foams are not observed in the cross-section images, increasing drug penetration through the initial layers of pores is observed with the incorporation of PVA. To further study how DOX is distributed within the cells of the TMHDI foam, SEM images of the cut foams were captured (**Figure 5.1C**). Approximately, 90% of the cell membranes separating the pores in the exterior foam surface are disrupted in the presence of DOX without PVA or lower PVA concentration (1%). Cell membranes were disturbed to a lesser extent in foams with higher PVA concentrations (3%, 10%). Viscous drug coating on the exterior surface of the foam likely prevented the trace amount of DMSO in the DOX solution to rupture the cell membranes. PVA/DOX solution was adsorbed onto the foam and covered the pores in the foam during the incubation and drying process. This increased drug loading onto the foams was also confirmed with UV/Vis spectroscopy (**Figure 5.1D**). The increase in absorbance intensity with increasing PVA concentration indicates the increased drug concentration adsorbed onto the exterior surface of the TMHDI foams.

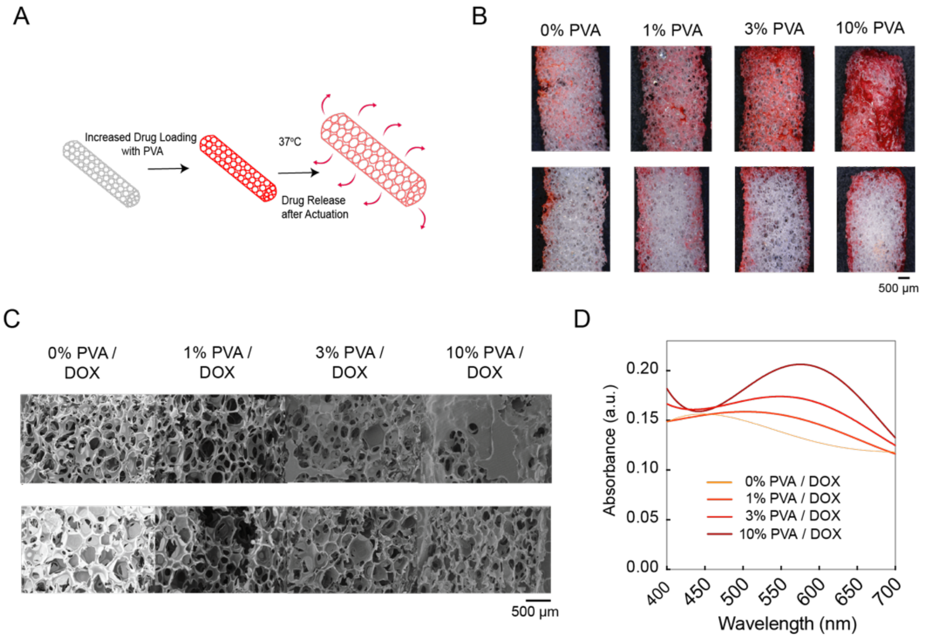

Figure 5.1 Increased DOX loading onto SMP foams. A) Scheme representing DOX loading and actuation of DOX-loaded SMP foam at 37 °C. **B)** Increased DOX loading is observed with increasing PVA concentration. **C)** SEM images of DOX-loaded SMP foams highlighting increased surface localization of DOX within the membrane between cells with increasing PVA concentration. **D)** Increase in DOX loading is validated using UV/Vis spectroscopy as increasing PVA concentration resulted in increase in absorption intensity.

5.2.2. Thermal and Expansion Behavior of Drug-loaded Foams:

Upon improving the drug loading onto the foam, it is crucial to ensure that the foams can be effectively crimped radially. Because this crimping process requires elevated temperatures, it is also important to understand the impact of drug solution on the thermal behavior of the TMHDI foams. Glass transition temperatures (T_g) of the foams were found to be 69 +/- 0.9 °C, 79 +/- 0.7 °C, 71 +/- 1.2 °C, 73 +/- 4.0 °C, and 62 +/- 3.3 °C for foams with no DOX/0% PVA, DOX/0% PVA, DOX/1% PVA, DOX/3% PVA and DOX/10% PVA, respectively (**Figure 5.2A**). The difference between the foam without DOX and foam with DOX in 3% PVA was not statistically significant. However, Tg slightly increased for foams with DOX formulations with 0% and 1% PVA and slightly decreased for foams with DOX/10% PVA. Although DOX formulations slightly modified the themal property of TMHDI foams, there was no drastic effect as higher PVA% seemed to offset the increase in Tg observed with DOX and lower PVA %. Small molecule drugs like DOX are usually stable at higher temperatures and can maintain therapeutic viability [200]. However, validating the therapeutic efficacy of DOX at higher temperatures is essential to determine ideal crimping temperature. Dose-dependent metabolic activity was first characterized by exposing MCF-7 human breast cancer cell line to varying concentrations of DOX. IC50 value was determined to be 0.08 μM and separate DOX solutions at this concentration was incubated at 37, 50, 65, and 75 °C, respectively. Metabolic activity of the cells was not affected significantly when DOX solutions were incubated at 37, 50, and 65 °C but metabolic activity increased, that is therapeutic efficacy was reduced, when DOX solution was exposed to 75 °C (**Figure 5.2C**). These results indicate that there is minimal effect of elevated temperature used for crimping on the therapeutic efficacy of DOX leading to promising non-invasive anti-cancer applications in the future.

Based on the thermal and metabolic results, foams coated with DOX in lowest PVA concentration (1%) and in highest PVA concentration (10%) were crimped radially at 65 °C. At this temperature, therapeutic efficacy of DOX is maintained and plasticization of foam can be achieved as transition usually occurs at a broad temperature range. After crimping DOX-loaded foams with 1% PVA was successfully fitted into a 18G needle (as this needle size is the upper limit for non-surgical procedures) but DOX-loaded foams with 10% PVA could only fit in a 16G needle (**Figure 5.2B**). Although 16G needle would be considered surgical, these promising results introduce the possibility of using drug-loaded TMHDI foams for future non-invasive procedures.

Once the DOX-loaded TMHDI foams is implanted into surgical site, foams are expected to be actuated at 37 °C filling the irregular tissue void post-surgery. Hence, there is a need to ensure that expansion properties of the foam are not severely impacted by the DOX/PVA coating. Expansion studies of crimped DOX-loaded TMHDI foams showed that foams without DOX or PVA recovered completely (100%) but DOX-loaded foams with 10% PVA recovered only up to 77% after 15 minutes (**Figure 5.2D**). However, DOX loaded foams with 10% PVA recovered up to 93% after 30 minutes. These differences were not statistically significant indicating that expansion capability of the foams, despite the observed downward trend, was conserved with the addition of DOX and PVA.

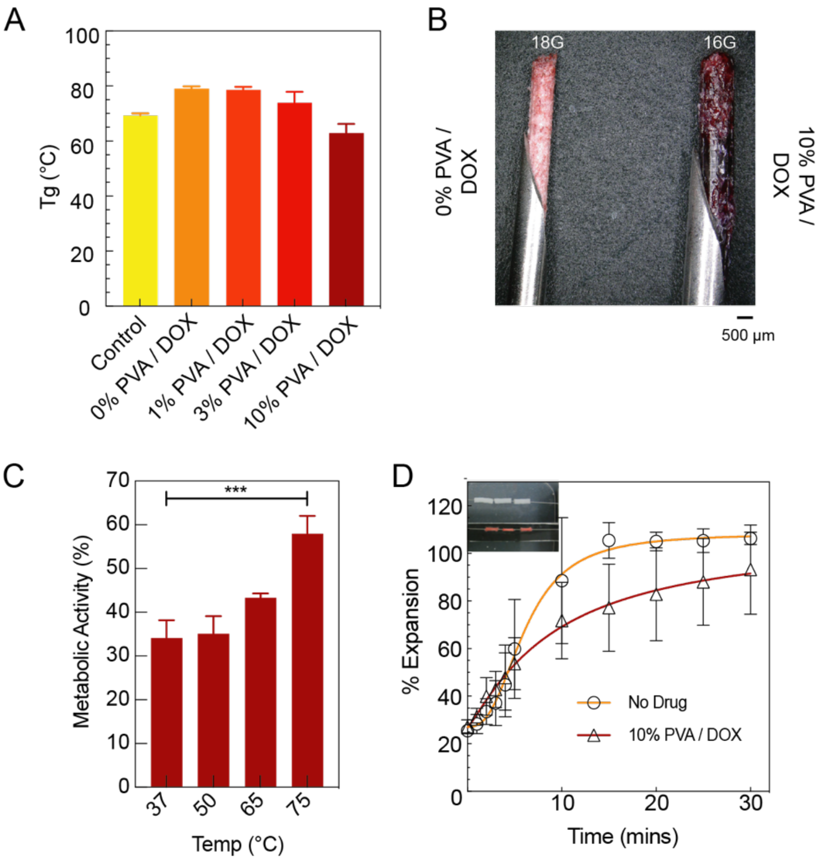

Figure 5.2 Thermal and expansion behavior after DOX/PVA loading. A) Thermal behavior of DOX-loaded SMP foams were characterized using T_g. Slight decrease in T_g was observed in foams with high PVA concentrations (3%, 10%). **B)** DOX-loaded foams with 10% PVA and without PVA were successfully into 16G and 18G needles, respectively. **C)** Functionality of DOX was not affected when exposed to crimping temperature of 65 °C. **D)** Expansion of DOX/PVA-loaded foams was not significantly affected indicating promise for efficient sealing of tissue-void.

5.2.3. *In Vitro* Drug Release, Viability, and Apoptotic Activity

DOX-loaded foams with varying PVA concentrations were incubated in media and drug release was measured using fluorescence at pre-determined time points to understand the release kinetics of DOX from the TMHDI foams (**Figure 5.3A**). Fluorescence intensity was converted to mass using the calibration curve that was obtained to establish a relationship between DOX concentration and corresponding fluorescent intensities

(**Figure 5.3B**). Similar to the initial release studies conducted using Acri in HDI foams, higher PVA formulated resulted in increased cumulative drug release (**Figure 5.3C** & **5.3D**). Initially (between 0 and 8 hours) of the release study, DOX-loaded foam without PVA resulted in burst release. This immediate release is likely due to the superficial coating of the foam by free DOX and in a clinical setting could result in higher DOX to be released causing side-effects. In contrast, DOX-loaded foams with higher PVA concentrations facilitated sustained release of DOX, which is ideal for the targeted adjuvant therapy application. After 8 hours, this trend reversed as released from DOX-loaded foam without PVA slowly tapered off while constant release was observed in foams with high PVA concentrations (1, 3, 10%). These results support our initial hypothesis that release kinetics can be modified using PVA to yield controlled and sustained drug release.

To determine the therapeutic efficacy of the released DOX, supernatants at pre-determined time points in the release study were administered to MCF-7 human breast cancer cells. Metabolic activities of the cells indicated a trend (**Figure 5.3E**) that supported the DOX release trend (**Figure 5.3C** & **5.3D**). During the initial phase of release (day 1), reduced metabolic activity of 21% and 31% was observed when treated with drug released from 0% and 10% PVA foams, respectively. This result corresponds to burst release of DOX observed in 0% PVA foams and higher drug release (due to higher drug loading) in 10% PVA foams. On the contrary, higher metabolic activities of 44% and 54% were observed when treated with drug released from 1% and 3% PVA foams, respectively. Release data from these two foams showed overall reduced drug release compared to the other two formulations, thus supporting the higher metabolic activity finding. Similar inferences can be made from metabolic activity and release studies at days 3 and 7. Therapeutic efficacy of DOX is thus maintained after its released from PVA-coated TMHDI foams.

Metabolic activity was used to represent the percentage of live cells. However, it is also important to characterize the cells that are undergoing apoptotic mechanism. This evaluation is especially important because DOX is a cytotoxic drug that is known to increase apoptotic activities in cells [201]. Capase-3 enzyme has been commonly used to characterize and quantify apoptotic activity in cells. High caspase-3 activities were observed to be highest for 0% and 10% PVA foams corresponding to the low metabolic activities observed in these formulations (**Figure 5.3F**). DOX-loaded foams with 1% and 3% PVA, low caspase-3 activities were observed aligning with high metabolic activities observed. Similar trend between metabolic activity and apoptotic activity was determined for days 3 and 7. Maintenance of therapeutic efficacy of released DOX was validated using this apoptotic study, further asserting promise for clinical use of DOX/PVA formulation.

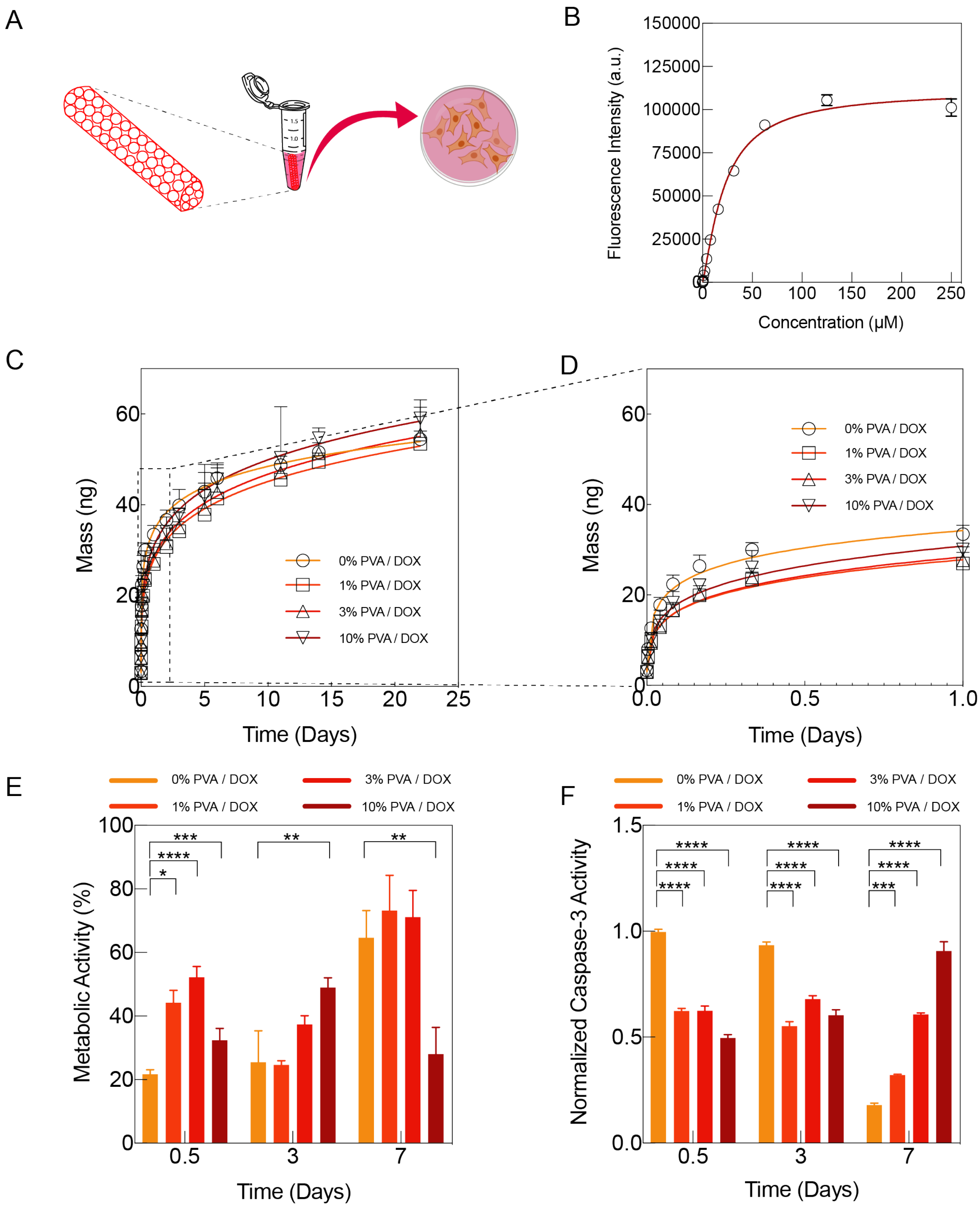

Figure 5.3 Assessment of DOX release and DOX functionality *in vitro*. A) Scheme of *in vitro* release studies of DOX/PVA-loaded foams conducted in cell media. **B)** DOX calibration that was used to quantify the mass of DOX that was released. **C)** Long-term sustained DOX release achieved through the incorporation of PVA. **D)** Burst DOX

release that is observed in the absence of PVA during the initial phase of release (before day 1). **E)** Therapeutic efficacy of DOX was maintained after the incorporation of PVA as demonstrated by the inverse relationship observed between amount of DOX released and metabolic activity of cells after administration of released DOX. **F)** Apoptotic activity of DOX was also maintained as witnessed by the inverse relationship between metabolic activity of cells in **E)** and caspase-3 activity of cells.

5.3. Conclusion

Current therapeutic strategy of administering systemic chemotherapy as an adjuvant to surgical resection of early stage breast tumor increases cytotoxicity and does not effectively prevent recurrence. Alternate polymer-based strategies like hydrogels and implants have limitations in terms of drug loading and effective tissue void sealing. To overcome these challenges, in this study we introduced a novel chemotherapeutic delivery formulation using PVA that is coated on SMP foams to enable sustained drug release and precise sealing of tissue void left after surgical resection thus preventing the spread of residual breast cancer cells.

Chemotherapeutic drug, DOX, loading was increased significantly onto the biocompatible TMHDI SMP foams with the incorporation of PVA. Additionally, thermal and actuation properties of the SMP foam was maintained after being coated by the DOX/PVA formulation. DOX/PVA-coated foam was shown to be effectively crimped radially leading to successful loading to the needle (DOX/0% PVA in 18G and DOX/10% PVA in 16G) for non-invasive delivery. This is especially crucial because in current treatment strategy, administration of systemic chemotherapy is not immediately administered after surgery to enable patient stabilization and avoid post-surgical complications. Hence, allowing for a non-invasive strategy could be extremely beneficial.

This combined with the effective SMP expansion post-actuation at body temperature highlights the potential use of this platform as a breast cancer adjuvant therapy. Sustained delivery of DOX was also successfully achieved through the incorporation of PVA avoiding the burst release that would have otherwise resulted (in < day 1). It is also important to note that therapeutic efficacy of DOX was not perturbed by the formulation or the release based on our successful *in vitro* studies in MCF-7 human breast cancer cells. Following these promising *in vitro* results, in depth investigation of the ability of DOX/PVA-loaded foams to prevent breast cancer recurrence in an *in vivo* model is needed. These *in vivo* studies which will also help with thorough characterization of release kinetics of DOX. Prior to conducting the *in vivo* studies, DOX/PVA-loaded SMP foams should be sterilized using E-beam, the thermal and expansion effects of which will be assessed and characterized.

5.4. Materials & Methods

5.4.1. SMP Foam Synthesis

SMP foam synthesis protocol was originally developed by Singhal et al. and TMHDI foams were synthesized based on this previously established protocol. Two-sided polyurethane synthesis reaction was used where Side A includes all isocyanate components, surfactants, and a cell opener. Trimethyl hexamethylene diisocyanate (TMHDI, mixture of 2,2,4- and 2,4,4-isomers, TCI America) was used as an isocyanate monomer and Ortegol (Evonik) was used as a cell opener. DC1990 and DC5943 were used as surfactants. Side B includes all the hydroxyl components and catalysts. N,N,N',N'-tetrakis (2-hydroxypropyl) ethylenediamine (HPED, 99%, MilliporeSigma) and triethanolamine (TEA, MilliporeSigma) in 60 mol% and 40 mol%, respectively, were used as hydroxyl monomers and BL-22 and T-131 (Evonik) were used as catalysts.

Portion of HPED and TEA were mixed with TMHDI-containing pre-polymer in a glovebox and were mixed by hand prior to curing. Oven (CascadeTek) was used to set the curing cycle program to ramp up to 50 °C and ramp down to room temperature for 48 hours. After the cure cycle completed, 2.5 and 5 wt% of DC1990 and DC5943, respectively, and 0.5 wt% of Ortegol were added to a FlackTek mixin cup (FlackTek, Inc.) and mixed at 2540 RPM for 1 min. Remaining portion of HPED and TEA were mixed with DI water in a FlackTek cup at 2540 RPM for 30 seconds twice. This solution was also manually mixed with a spatula prior to adding and mixing BL-22 and T-131 catalysts for 30 seconds. This mixture of hydroxyl monomers and catalysts was then added to the pre-polymer mixture followed by 15 seconds of mixing. Finally, 2 mL of physical blowing agent, Enovate 245fa (1,1,1,3,3-pentafluoropropane, Honeywell), was mixed with the solution with other components for 15 seconds. This final reaction mixture was poured onto a pan and incubated in an over at 90 °C for 30 min.

5.4.2. Drug Formulation

Stock drug solutions of 1mg/mL were prepared by mixing Acri or DOX powder in DMSO. PVA of varying concentrations (1%, 3%, 10%) were prepared by mixing the required amount of PVA powder in DI water which was subsequently stirred and heated at 80 °C for two hours. Stock drug solution was then added to the prepared PVA solution or DI water to make 1mL of solution with final concentration of 0.017 mg/mL and mixed thoroughly.

5.4.3. Drug Loading

Cleaned TMHDI foams were into smaller pieces that are 0.7 mm in length. The foams were then placed into tubes with drug/PVA or drug/water solutions and incubated overnight at room temperature in a rotator (MANUFACTURER) that was set to speed 0.4 RPM. The incubated foams were then retrieved from the solutions and were dried in a vacuum chamber at room temperature for 7 days.

5.4.4. Differential Scanning Calorimetry

Thermal properties of drug/PVA-loaded foams was analyzed using differential scanning calorimeter (DSC Q200, TA Instruments). Dry glass transition temperature (T_g) was measured by loading drug-loaded foams between 5-10 mg (n = 3) into T0 aluminum pans. DSC measurements ran from -40 °C to 120 °C with a ramp of 10 °C/min. This cycle was repeated twice where the samples were held at the lowest and highest temperatures for 2 min. T_g was calculated based on the second cycle based on the temperature inflection point using the TA Universal Analysis software.

5.4.5. Crimping and Needle Loading

Cleaned foams were cut into cylindrical foams with 3 mm diameter using biopsy punches. Cut foams were radially crimped by heating at 65 °C for 15 mins in a barrel stationed inside a Machine Solutions SC250 stent crimper. Foams were cooled to room temperature and were moved to desiccator for 48 hours before being used for needle loading to avoid premature foam expansion. Crimped foams containing drug and 0% or 10% PVA compositions were attempted to be inserted into 18G or 16G needle depending on the total diameter of the drug-loaded foam.

5.4.6. Expansion Study

TMHDI cut into cylindrical foams of 6mm diameter were crimped at 65 °C and dried for 48 hours at room temperature ($n = 3$) prior to use in expansion studies. Wire was used to thread these crimped foams, images of which were taken to determine initial crimped diameter prior to actuation. Foams were then placed in a water bath that was pre-heated to 37 °C after which images were recorded every min for the first 10 min. Between 10 min and 30 min, images were taken every 5 min. Collected images were analyzed using ImageJ software to determine the overall diameter (5 point in each foam were measured). These measurements were compared to the initial crimped diameter to determine percentage of expansion.

5.4.7. Temperature Study

DOX concentration of 0.08µM (IC50) was prepared by diluting 1mg/mL DOX stock solution (in DMSO) in Dulbecco's Modified Eagle Medium high glucose (DMEM HG) (media used for MCF-7 cells). Solutions were aliquoted into Eppendorf tubes for a final volume of 1mL. Tubes containing DOX solutions were incubated at the pre-determined temperatures (37, 50, 65, 75 °C) for 15 minutes to mimic the temperature conditions exposed during the crimping process. Solutions were cooled to room temperature after removing from the incubator. MCF-7 cells were seeded in a 96-well plate at the density of 5000 cells/well. Cooled incubated DOX solutions (0.1mL) were administered to MCF-7 cells 24 hours after seeding ($n = 3$/experimental group). Control group ($n = 3$) included treatment of MCF-7 cells with DMEM HG media without the presence of DOX. 72 hours after administration of DOX solutions, metabolic activity of the cells was assessed using MTS/PMS reagents from the CellTiter 96 AQueous Non-Radioactive Cell Proliferation Assay (Promega Corporation, Madison, WI) based on the manufacturer's protocol.

5.4.8. Drug Release

DOX (or Acri)/PVA-loaded TMHDI foams (n = 3/group) were placed in 0.4 mL of PBS or DMEM HG media and were incubated at 37 °C and 5% CO_2 to mimic physiological conditions. Supernatants were removed at various pre-determined time points (min to hours to days) and were measured for fluorescence at 416/514nm (Ex/Em) for Acriand 485/590nm for DOX using Cytation 5 (Biotek, VT). Foams were incubated with 0.4 mL of fresh DMEM HG media after the supernatant was collected.

5.4.9. *In vitro* Assessment

Supernatants collected from the release studies conducted in DMEM HG media were stored in -80 °C until the cell study was conducted. MCF-7 cells were culture to 70% confluency in DMEM HG media with 10% FBS and 1% Pen Strep at 37 °C and 5% CO_2. MCF-7 cells were then passaged and seeded in 96-well plate with seeding density of 5000 cells/well. Supernatants were thawed in water bath at 37 °C prior to administering to the cells. 24 hours after seeding, 0.1 mL of thawed supernatants were administered to the cells. Control group (n = 3) included treatment of MCF-7 cells with only DMEM HG media. Metabolic activity of the cells was assessed 72 hours after administration of DOX solutions using MTS/PMS reagents from the CellTiter 96 AQueous Non-Radioactive Cell Proliferation Assay (Promega Corporation, Madison, WI) based on the manufacturer's protocol. Apoptotic activity of the cells was measured and quantified 72 hours after administration of DOX solutions using Caspase-Glo® 3/7 Assay System (Promega Corporation, Madison, WI) based on the manufacturer's protocol.

6. CONCLUSIONS

6.1. Summary of Present Findings

Through this dissertation, we engineered three delivery platforms that can potentially be used for controlled delivery of vaccines and/or anti-cancer agents. Biodegradable polyesters were fabricated using a non-emulsion method to reduce organic solvent exposure of sensitive cargo (Chapter 2), and enable on-demand delayed burst release of cargo (Chapter 3). Second delivery platform was synthesized by incorporating defect-rich MoS_2 nanoassemblies into PAN nanofibers to improve cytocompatibility so that the nanofibers could potentially be used for small molecule delivery in the future (Chapter 4). Third delivery platform was designed for the use of a drug-loaded porous polyurethane foam with shape memory properties as an adjuvant to breast cancer surgery (Chapter 5). This diverse range of biomaterial-based delivery platforms provide promising therapeutic opportunities.

In our first platform, we fabricated polyester-based core shell particle called polybubbles for vaccine delivery applications (Aim 1 and Chapter 2). Polybubbles were synthesized by injecting polycaprolactone triacrylate (PCLTA) into an aqueous solution, forming a spherical bubble. Cargo was then manually injected into the bubble and was subsequently cured to improve structural integrity. Through this process, cargo centering proved to be challenging as cargo had the tendency to move upwards towards the surface of the polybubbles. We successfully reduced the cargo migration using a viscous solution, 5 wt% carboxymethyl cellulose (CMC), along with the cargo ensuring that the predicted release profile is uniform. Upon solving this challenge, we used anti-HIV antigen as a model cargo to assess cargo functionality within the polybubbles. We successfully demonstrated that 70% of antigen functionality was maintained even after 1 week of contact with the polybubbles. These encouraging results provide insight into the potential use of sensitive cargo, like antigens, in a controlled delivery system like the polybubble. Unlike traditional emulsion-based particles, our system has demonstrated the ability to reduce the contact of cargo with moisture (post-freeze drying) and organic solvent while maintaining cargo functionality.

Polybubble technology was further optimized to achieve cargo centering and novel on-demand release kinetics (Aim 2 and Chapter 3). Polybubbles were fabricated using poly (lactic-co-glycolic acid) PLGADA and PCLTA with shorter and longer degradation times, respectively. Polybubble's sphericity was maintained during the fabrication process by increasing the viscosity of outer aqueous solution using 10% CMC. Cargo was also centered using 5% CMC with the cargo and increasing polymer viscosity, thus preventing the upward migration towards the surface of polybubbles. We assessed the release kinetics of two cargo types, small molecule and large molecule, that were housed in PLGADA and PCLTA. Novel delayed burst release was observed owing to the bulk degradation property of the polyesters that were used to fabricate the polybubbles. We also achieved expedited release of small molecules through on-demand near-infrared (NIR) activation of polybubbles through the incorporation of NIR-sensitive gold nanorods (AuNRs). Functionality of small molecule cargo upon release was also assessed demonstrating that therapeutic efficacy of the cargo could be maintained with and without laser activation. These encouraging results highlight improved cargo versatility and novel release kinetics from the polybubbles demonstrating their potential use in downstream applications like vaccine delivery.

In our third study, we endeavored to optimize mechanical properties and cytocompatibility of PAN nanofibers for potential applications in drug delivery. We incorporated defect-rich MoS_2 nanoassemblies, that have unique mechanical, electrical, and optical properties, into PAN nanofibers through electrospinning. Defects were introduced in MoS_2 nanoassemblies by varying precursor ratio (Mo:S), further resulting in enhanced surface properties in PAN nanofiber compositions with high concentration of S. Defect-rich MoS_2 with 1:5 precursor ratio demonstrated high porosity, high surface area, and superior optical properties, making it an ideal choice to be incorporated into PAN nanofibers. Assessment of electrospun PAN/ MoS_2 nanofibers demonstrated increased bead formation along the nanofiber with increasing MoS_2 concentration. Interaction between MoS_2 and PAN resulted in improved mechanical strength, electrical conductivity, and hydrophilicity of the nanofibers. Additionally, increased hydrophilicity likely resulted in improved cell adhesion with the incorporation of defect-rich MoS_2, reaffirming the prospect of improved cytocompatibility. Improved physical properties and cytocompatibility of the PAN/MoS_2 nanofibers presents exciting possibilities for use of carbon-based nanofibers in a variety of biomedical applications including drug delivery.

Finally, in study 4, we developed a formulation to improve drug loading onto polyurethane-based shape memory polymer (SMP) foams to be used as an adjuvant therapy after the surgical resection of breast cancer tumors (Aim 4 and Chapter 5). Chemotherapeutic drug, DOX, loading was successfully increased through the addition of a viscosity modulating agent called polyvinyl alcohol (PVA). In addition to being used as a drug delivery platform, SMP foams have favorable properties that can be leveraged to be used for precisely sealing post-surgical tissue void. SMP can be actuated at physiological temperature allowing the foam to expand and fit irregular spaces, similar to that of post-surgical voids. To ensure that this expansion property is not hindered by DOX/PVA loading. Our assessments show that SMP properties are not significantly affected by our formulation process. Additionally, we also observed that the incorporation of PVA yielded in long-term sustained release of DOX compared to the burst release that was observed in drug formulation without PVA. This type of release kinetics is favorable to ensure that dose dumping of DOX is avoided as it can result in adverse side effects. We also successfully ensured that therapeutic efficacy of DOX is not compromised post-release from the SMP foams. These proof-of-concept results are encouraging and highlights the potential use of SMP foams as a drug delivery vehicle with tissue sealing capabilities. We are currently investigating the maintenance of DOX functionality and feasibility of tissue-void sealing in an *in vivo* setting.

6.2. Future Recommendations

Engineering three types of polymer-based platforms capable of catering to a variety of drug delivery-related challenges were discussed in this work. Promising results from the previously described studies highlights the importance of biomaterial-based platforms in improving efficacy of existing therapeutic agents like vaccines and chemotherapy drugs. However, in-depth analysis is needed to ensure that predictable release profiles are achieved using these platforms in dynamic *in vitro* and *in vivo* environments. Release kinetics of different cargo types should be assessed in animal models to thoroughly characterize release time and functionality with and without laser activation in polybubbles. With respect to PAN/MoS_2 nanofibers, small molecule drugs should be loaded and their respective release profiles should be characterized in a methodical manner. Lastly, release kinetics and therapeutic efficacy of DOX/PVA-loaded SMP foams can be assessed in an animal breast cancer model. SMP foams have previously been thoroughly investigated and has been approved for treating aneurysms. DOX is a common chemotherapeutic drug that is commonly administered to cancer patients and PVA is used in several clinical models for extended release formulations. Thus, biocompatibility of the individual components is not a concern. DOX/PVA-loaded foams have potential to be clinically translated and sterilization studies should be conducted prior to *in vivo* administration of DOX/PVA-loaded SMP foams. Additionally, effect of sterilization on the properties of SMP and DOX should also be closely monitored. Proposed future assessments will strengthen the possibility of clinical use of the three novel delivery platforms discussed in this dissertation.

REFERENCES

[1] Disease Burden and Mortality Estimates, 2016. http://www.who.int/healthinfo/global_burden_disease/estimates/en/index2.html.

[2] 10 Facts on Polio Eradication, 2017. http://www.who.int/features/factfiles/polio/en/.

[3] The Vaccines, 2016. http://polioeradication.org/polio-today/polio-prevention/the-vaccines/opv/.

[4] C.C. Quianzon, I. Cheikh, History of insulin, J Community Hosp Intern Med Perspect 2(2) (2012).

[5] B. Leader, Q.J. Baca, D.E. Golan, Protein therapeutics: a summary and pharmacological classification, Nat Rev Drug Discov 7(1) (2008) 21-39.

[6] G. Walsh, Biopharmaceuticals: recent approvals and likely directions, Trends Biotechnol 23(11) (2005) 553-8.

[7] D.V. Goeddel, D.G. Kleid, F. Bolivar, H.L. Heyneker, D.G. Yansura, R. Crea, T. Hirose, A. Kraszewski, K. Itakura, A.D. Riggs, Expression in Escherichia coli of chemically synthesized genes for human insulin, Proc Natl Acad Sci U S A 76(1) (1979) 106-10.

[8] H.A. Lagasse, A. Alexaki, V.L. Simhadri, N.H. Katagiri, W. Jankowski, Z.E. Sauna, C. Kimchi-Sarfaty, Recent advances in (therapeutic protein) drug development, F1000Res 6 (2017) 113.

[9] O.D. Krishna, K.L. Kiick, Protein- and peptide-modified synthetic polymeric biomaterials, Biopolymers 94(1) (2010) 32-48.

[10] G. Zhu, S.R. Mallery, S.P. Schwendeman, Stabilization of proteins encapsulated in injectable poly (lactide- co-glycolide), Nat Biotechnol 18(1) (2000) 52-7.

[11] A. Kumari, S.K. Yadav, S.C. Yadav, Biodegradable polymeric nanoparticles based drug delivery systems, Colloids Surf B Biointerfaces 75(1) (2010) 1-18.

[12] C. Dai, B. Wang, H. Zhao, Microencapsulation peptide and protein drugs delivery system, Colloids Surf B Biointerfaces 41(2-3) (2005) 117-20.

[13] M. Horiguchi, M. Arita, D.E. Kaempf-Rotzoll, M. Tsujimoto, K. Inoue, H. Arai, pH-dependent translocation of alpha-tocopherol transfer protein (alpha-TTP) between hepatic cytosol and late endosomes, Genes Cells 8(10) (2003) 789-800.

[14] K. Talley, E. Alexov, On the pH-optimum of activity and stability of proteins, Proteins 78(12) (2010) 2699-706.

[15] W. Wang, Instability, stabilization, and formulation of liquid protein pharmaceuticals, Int J Pharm 185(2) (1999) 129-88.

[16] M.C. Manning, D.K. Chou, B.M. Murphy, R.W. Payne, D.S. Katayama, Stability of protein pharmaceuticals: an update, Pharm Res 27(4) (2010) 544-75.

[17] R. Krishnamurthy, M.C. Manning, The stability factor: importance in formulation development, Curr Pharm Biotechnol 3(4) (2002) 361-71.

[18] S. Mitragotri, P.A. Burke, R. Langer, Overcoming the challenges in administering biopharmaceuticals: formulation and delivery strategies, Nat Rev Drug Discov 13(9) (2014) 655-72.

[19] M. Morishita, N.A. Peppas, Is the oral route possible for peptide and protein drug delivery?, Drug Discovery Today 11(19) (2006) 905-910.

[20] W. Jiskoot, T.W. Randolph, D.B. Volkin, C.R. Middaugh, C. Schoneich, G. Winter, W. Friess, D.J. Crommelin, J.F. Carpenter, Protein instability and immunogenicity: roadblocks to clinical application of injectable protein delivery systems for sustained release, J Pharm Sci 101(3) (2012) 946-54.
[21] T. Estey, J. Kang, S.P. Schwendeman, J.F. Carpenter, BSA degradation under acidic conditions: a model for protein instability during release from PLGA delivery systems, J Pharm Sci 95(7) (2006) 1626-39.
[22] J.F. Carpenter, M.C. Manning, T.W. Randolph, Long-term storage of proteins, Curr Protoc Protein Sci Chapter 4 (2002) Unit 4 6.
[23] W. Wang, S.K. Singh, N. Li, M.R. Toler, K.R. King, S. Nema, Immunogenicity of protein aggregates--concerns and realities, Int J Pharm 431(1-2) (2012) 1-11.
[24] W. Caparros-Wanderley, B. Clark, B.E. Griffin, Effect of dose and long-term storage on the immunogenicity of murine polyomavirus VP1 virus-like particles, Vaccine 22(3-4) (2004) 352-61.
[25] D.D. Banks, D.M. Hambly, J.L. Scavezze, C.C. Siska, N.L. Stackhouse, H.S. Gadgil, The effect of sucrose hydrolysis on the stability of protein therapeutics during accelerated formulation studies, J Pharm Sci 98(12) (2009) 4501-10.
[26] D. Chen, D. Kristensen, Opportunities and challenges of developing thermostable vaccines, Expert Rev Vaccines 8(5) (2009) 547-57.
[27] J.P. Amorij, A. Huckriede, J. Wilschut, H.W. Frijlink, W.L. Hinrichs, Development of stable influenza vaccine powder formulations: challenges and possibilities, Pharm Res 25(6) (2008) 1256-73.
[28] C.L. Karp, D. Lans, J. Esparza, E.B. Edson, K.E. Owen, C.B. Wilson, P.M. Heaton, O.S. Levine, R. Rao, Evaluating the value proposition for improving vaccine thermostability to increase vaccine impact in low and middle-income countries, Vaccine 33(30) (2015) 3471-9.
[29] S.W. James, S. Friel, An integrated approach to identifying and characterising resilient urban food systems to promote population health in a changing climate, Public Health Nutr 18(13) (2015) 2498-508.
[30] Immunization Coverage, 2018. http://www.who.int/en/news-room/fact-sheets/detail/immunization-coverage.
[31] D.M. Matthias, J. Robertson, M.M. Garrison, S. Newland, C. Nelson, Freezing temperatures in the vaccine cold chain: a systematic literature review, Vaccine 25(20) (2007) 3980-6.
[32] O.S. Kumru, S.B. Joshi, D.E. Smith, C.R. Middaugh, T. Prusik, D.B. Volkin, Vaccine instability in the cold chain: mechanisms, analysis and formulation strategies, Biologicals 42(5) (2014) 237-59.
[33] U. Bilati, E. Allemann, E. Doelker, Strategic approaches for overcoming peptide and protein instability within biodegradable nano- and microparticles, Eur J Pharm Biopharm 59(3) (2005) 375-88.
[34] S. Mohammadi-Samani, B. Taghipour, PLGA micro and nanoparticles in delivery of peptides and proteins; problems and approaches, Pharm Dev Technol 20(4) (2015) 385-93.

[35] F. Khademi, M. Derakhshan, A. Yousefi-Avarvand, M. Tafaghodi, Potential of polymeric particles as future vaccine delivery systems/adjuvants for parenteral and non-parenteral immunization against tuberculosis: A systematic review, Iran J Basic Med Sci 21(2) (2018) 116-123.
[36] S. Kim, K. Kim, S.Q. Choi, Controllable one-step double emulsion formation via phase inversion, Soft Matter 14(7) (2018) 1094-1099.
[37] R.L. McCall, R.W. Sirianni, PLGA nanoparticles formed by single- or double-emulsion with vitamin E-TPGS, J Vis Exp (82) (2013) 51015.
[38] I.D. Rosca, F. Watari, M. Uo, Microparticle formation and its mechanism in single and double emulsion solvent evaporation, J Control Release 99(2) (2004) 271-80.
[39] F. Danhier, E. Ansorena, J.M. Silva, R. Coco, A. Le Breton, V. Preat, PLGA-based nanoparticles: an overview of biomedical applications, J Control Release 161(2) (2012) 505-22.
[40] L. Li, S.P. Schwendeman, Mapping neutral microclimate pH in PLGA microspheres, J Control Release 101(1-3) (2005) 163-73.
[41] Y. Liu, A.H. Ghassemi, W.E. Hennink, S.P. Schwendeman, The microclimate pH in poly(D,L-lactide-co-hydroxymethyl glycolide) microspheres during biodegradation, Biomaterials 33(30) (2012) 7584-93.
[42] V.R. Sinha, A. Trehan, Biodegradable microspheres for protein delivery, J Control Release 90(3) (2003) 261-80.
[43] W. Park, K. Na, Dermatan sulfate as a stabilizer for protein stability in poly (lactide-co-glycolide) depot, Biotechnology and bioprocess engineering 14(5) (2009) 668.
[44] Y. Liu, S.P. Schwendeman, Mapping microclimate pH distribution inside protein-encapsulated PLGA microspheres using confocal laser scanning microscopy, Mol Pharm 9(5) (2012) 1342-50.
[45] L. Duque, M. Korber, R. Bodmeier, Improving release completeness from PLGA-based implants for the acid-labile model protein ovalbumin, Int J Pharm 538(1-2) (2018) 139-146.
[46] D.V. Goeddel, H.L. Heyneker, T. Hozumi, R. Arentzen, K. Itakura, D.G. Yansura, M.J. Ross, G. Miozzari, R. Crea, P.H. Seeburg, Direct expression in Escherichia coli of a DNA sequence coding for human growth hormone, Nature 281(5732) (1979) 544-8.
[47] S.D. Putney, P.A. Burke, Improving protein therapeutics with sustained-release formulations, Nat Biotechnol 16(2) (1998) 153-7.
[48] P.L. Privalov, Cold denaturation of proteins, Crit Rev Biochem Mol Biol 25(4) (1990) 281-305.
[49] F. Franks, Protein destabilization at low temperatures, Adv Protein Chem 46 (1995) 105-39.
[50] V.J. Hilser, J. Gomez, E. Freire, The enthalpy change in protein folding and binding: refinement of parameters for structure-based calculations, Proteins 26(2) (1996) 123-33.
[51] T. Ku, P. Lu, C. Chan, T. Wang, S. Lai, P. Lyu, N. Hsiao, Predicting melting temperature directly from protein sequences, Comput Biol Chem 33(6) (2009) 445-50.

[52] H.K. Liang, C.M. Huang, M.T. Ko, J.K. Hwang, Amino acid coupling patterns in thermophilic proteins, Proteins 59(1) (2005) 58-63.

[53] E. Mombelli, E. Shehi, P. Fusi, P. Tortora, Exploring hyperthermophilic proteins under pressure: theoretical aspects and experimental findings, Biochim Biophys Acta 1595(1-2) (2002) 392-6.

[54] A.V. Finkelstein, A.M. Gutin, A.Y. Badretdinov, Perfect temperature for protein structure prediction and folding, Proteins 23(2) (1995) 151-62.

[55] W.N. Souery, S. Arun Kumar, D. Prasca-Chamorro, D.M. Moore, J. Good, C.J. Bishop, Controlling and quantifying the stability of amino acid-based cargo within polymeric delivery systems, J Control Release 300 (2019) 102-113.

[56] C.J. Martinez Rivas, M. Tarhini, W. Badri, K. Miladi, H. Greige-Gerges, Q.A. Nazari, S.A. Galindo Rodriguez, R.A. Roman, H. Fessi, A. Elaissari, Nanoprecipitation process: From encapsulation to drug delivery, Int J Pharm 532(1) (2017) 66-81.

[57] N. Ibeanu, R. Egbu, L. Onyekuru, H. Javaheri, P.T. Khaw, G.R. Williams, S. Brocchini, S. Awwad, Injectables and Depots to Prolong Drug Action of Proteins and Peptides, Pharmaceutics 12(10) (2020).

[58] S. Schubert, J.J.T. Delaney, U.S. Schubert, Nanoprecipitation and nanoformulation of polymers: from history to powerful possibilities beyond poly(lactic acid), Soft Matter 7(5) (2011) 1581-1588.

[59] Y. Wang, P. Li, T. Truong-Dinh Tran, J. Zhang, L. Kong, Manufacturing Techniques and Surface Engineering of Polymer Based Nanoparticles for Targeted Drug Delivery to Cancer, Nanomaterials (Basel) 6(2) (2016).

[60] X. Li, X. Wang, A. Ito, Tailoring inorganic nanoadjuvants towards next-generation vaccines, Chem Soc Rev 47(13) (2018) 4954-4980.

[61] R. Mateu Ferrando, L. Lay, L. Polito, Gold nanoparticle-based platforms for vaccine development, Drug Discovery Today: Technologies (2021).

[62] C. Poon, A.A. Patel, Organic and inorganic nanoparticle vaccines for prevention of infectious diseases, Nano Express 1(1) (2020) 012001.

[63] Y.S. Chen, Y.C. Hung, W.H. Lin, G.S. Huang, Assessment of gold nanoparticles as a size-dependent vaccine carrier for enhancing the antibody response against synthetic foot-and-mouth disease virus peptide, Nanotechnology 21(19) (2010) 195101.

[64] F. Chiodo, P.M. Enriquez-Navas, J. Angulo, M. Marradi, S. Penades, Assembling different antennas of the gp120 high mannose-type glycans on gold nanoparticles provides superior binding to the anti-HIV antibody 2G12 than the individual antennas, Carbohydr Res 405 (2015) 102-9.

[65] H.K.V. Kumar, Nagasamy; Bhowmik, Himangshu ; Kuila, Anuttam Metallic Nanoparticle: A Review, Biomedical Journal of Scientific & Technical Research 4(2) (2018) 3765-2775.

[66] A. Jain, K.K. Bansal, A. Tiwari, A. Rosling, J.M. Rosenholm, Role of Polymers in 3D Printing Technology for Drug Delivery - An Overview, Curr Pharm Des 24(42) (2018) 4979-4990.

[67] W. Kempin, C. Franz, L.C. Koster, F. Schneider, M. Bogdahn, W. Weitschies, A. Seidlitz, Assessment of different polymers and drug loads for fused deposition modeling of drug loaded implants, Eur J Pharm Biopharm 115 (2017) 84-93.

[68] E. Mathew, G. Pitzanti, E. Larraneta, D.A. Lamprou, 3D Printing of Pharmaceuticals and Drug Delivery Devices, Pharmaceutics 12(3) (2020).
[69] K.J. McHugh, T.D. Nguyen, A.R. Linehan, D. Yang, A.M. Behrens, S. Rose, Z.L. Tochka, S.Y. Tzeng, J.J. Norman, A.C. Anselmo, X. Xu, S. Tomasic, M.A. Taylor, J. Lu, R. Guarecuco, R. Langer, A. Jaklenec, Fabrication of fillable microparticles and other complex 3D microstructures, Science 357(6356) (2017) 1138-1142.
[70] X. Chen, L. Wang, H. Yu, C. Li, J. Feng, F. Haq, A. Khan, R.U. Khan, Preparation, properties and challenges of the microneedles-based insulin delivery system, J Control Release 288 (2018) 173-188.
[71] L.Y. Chu, S.O. Choi, M.R. Prausnitz, Fabrication of dissolving polymer microneedles for controlled drug encapsulation and delivery: Bubble and pedestal microneedle designs, J Pharm Sci 99(10) (2010) 4228-38.
[72] K.J. McHugh, L. Jing, S.Y. Severt, M. Cruz, M. Sarmadi, H.S.N. Jayawardena, C.F. Perkinson, F. Larusson, S. Rose, S. Tomasic, T. Graf, S.Y. Tzeng, J.L. Sugarman, D. Vlasic, M. Peters, N. Peterson, L. Wood, W. Tang, J. Yeom, J. Collins, P.A. Welkhoff, A. Karchin, M. Tse, M. Gao, M.G. Bawendi, R. Langer, A. Jaklenec, Biocompatible near-infrared quantum dots delivered to the skin by microneedle patches record vaccination, Science Translational Medicine 11(523) (2019) eaay7162.
[73] A. Hou, B. Cohen, A. Haimovic, N. Elbuluk, Microneedling: A Comprehensive Review, Dermatol Surg 43(3) (2017) 321-339.
[74] Cancer Statistics. https://www.cancer.gov/about-cancer/understanding/statistics.
[75] K.B. Wood, Pairwise interactions and the battle against combinatorics in multidrug therapies, Proc Natl Acad Sci U S A 113(37) (2016) 10231-3.
[76] P. Parhi, C. Mohanty, S.K. Sahoo, Nanotechnology-based combinational drug delivery: an emerging approach for cancer therapy, Drug Discov Today 17(17-18) (2012) 1044-52.
[77] M.W.L. John L. Raytis, Surgical Stress Response adn Cancer Metastasis: The Potential Benefit of Perioperative Beta Blockade Landes Bioscience, 2013.
[78] S. Tohme, R.L. Simmons, A. Tsung, Surgery for Cancer: A Trigger for Metastases, Cancer Research 77(7) (2017) 1548-1552.
[79] A. Gagliardi, E. Giuliano, E. Venkateswararao, M. Fresta, S. Bulotta, V. Awasthi, D. Cosco, Biodegradable Polymeric Nanoparticles for Drug Delivery to Solid Tumors, Front Pharmacol 12 (2021) 601626.
[80] F. Masood, Polymeric nanoparticles for targeted drug delivery system for cancer therapy, Mater Sci Eng C Mater Biol Appl 60 (2016) 569-578.
[81] B. Mukherjee, B.S. Satapathy, L. Mondal, N.S. Dey, R. Maji, Potentials and challenges of active targeting at the tumor cells by engineered polymeric nanoparticles, Curr Pharm Biotechnol 14(15) (2013) 1250-63.
[82] D. Neha, M. Momin, T. Khan, S. Gharat, R.S. Ningthoujam, A. Omri, Metallic nanoparticles as drug delivery system for the treatment of cancer, Expert Opinion on Drug Delivery (2021) 1-30.
[83] Z.A. Nima, A.M. Alwbari, V. Dantuluri, R.N. Hamzah, N. Sra, P. Motwani, K. Arnaoutakis, R.A. Levy, A.F. Bohliqa, D. Nedosekin, V.P. Zharov, I. Makhoul, A.S.

Biris, Targeting nano drug delivery to cancer cells using tunable, multi-layer, silver-decorated gold nanorods, J Appl Toxicol 37(12) (2017) 1370-1378.
[84] J. Lee, Y.H. Lee, C.B. Jeong, J.S. Choi, K.S. Chang, M. Yoon, Gold nanorods-conjugated TiO2 nanoclusters for the synergistic combination of phototherapeutic treatments of cancer cells, J Nanobiotechnology 16(1) (2018) 104.
[85] S. Bagheri, M. Yasemi, E. Safaie-Qamsari, J. Rashidiani, M. Abkar, M. Hassani, S.A. Mirhosseini, H. Kooshki, Using gold nanoparticles in diagnosis and treatment of melanoma cancer, Artificial Cells, Nanomedicine, and Biotechnology 46(sup1) (2018) 462-471.
[86] J.B. Vines, J.H. Yoon, N.E. Ryu, D.J. Lim, H. Park, Gold Nanoparticles for Photothermal Cancer Therapy, Front Chem 7 (2019) 167.
[87] M. Champeau, J.M. Thomassin, T. Tassaing, C. Jerome, Current manufacturing processes of drug-eluting sutures, Expert Opin Drug Deliv 14(11) (2017) 1293-1303.
[88] D.Y. Fan, Y. Tian, Z.J. Liu, Injectable Hydrogels for Localized Cancer Therapy, Front Chem 7 (2019) 675.
[89] T.R. Hoare, D.S. Kohane, Hydrogels in drug delivery: Progress and challenges, Polymer 49(8) (2008) 1993-2007.
[90] J. Li, D.J. Mooney, Designing hydrogels for controlled drug delivery, Nat Rev Mater 1(12) (2016).
[91] C. Yang, N.T. Blum, J. Lin, J. Qu, P. Huang, Biomaterial scaffold-based local drug delivery systems for cancer immunotherapy, Science Bulletin 65(17) (2020) 1489-1504.
[92] T. Garg, G. Rath, A.K. Goyal, Biomaterials-based nanofiber scaffold: targeted and controlled carrier for cell and drug delivery, J Drug Target 23(3) (2015) 202-21.
[93] I.E. Palamà, V. Arcadio, S. D'Amone, M. Biasiucci, G. Gigli, B. Cortese, Therapeutic PCL scaffold for reparation of resected osteosarcoma defect, Scientific Reports 7(1) (2017) 12672.
[94] A.A. Exner, G.M. Saidel, Drug-eluting polymer implants in cancer therapy, Expert Opin Drug Deliv 5(7) (2008) 775-88.
[95] S.A. Plotkin, Vaccines: past, present and future, Nat Med 11(4 Suppl) (2005) S5-11.
[96] J. Lee, S. Arun Kumar, Y.Y. Jhan, C.J. Bishop, Engineering DNA vaccines against infectious diseases, Acta Biomater 80 (2018) 31-47.
[97] The top 10 causes of death, 2017. http://www.who.int/mediacentre/factsheets/fs310/en/. (Accessed 17th Nov 2017.
[98] W.H. Organization, Immunization Coverage Fact Sheet, 2018. http://www.who.int/news-room/fact-sheets/detail/immunization-coverage. (Accessed May 25 2018).
[99] C.G. Whitney, S.A. Harper, Lower respiratory tract infections: prevention using vaccines, Infect Dis Clin North Am 18(4) (2004) 899-917.
[100] W.H. Organization, Hepatitis B: Fact Sheet, 2017. http://www.who.int/news-room/fact-sheets/detail/hepatitis-b. (Accessed May 26 2018).
[101] WHO/UNICEF, Progress and Challenges with Achieving Universal Immunization Coverage: 2015 Estimates of Immunization Coverage. www.who.int/immunization/monitoring_surveillance/who-immuniz-2015.pdf (Accessed Sep 28 2017).

[102] M. Chojnacky, W. Miller, D. Ripple, G. Strouse, Nistir, G. Locke, P.D. Gallagher, Thermal Analysis of Refrigeration Systems Used for Vaccine Storage, (2009).
[103] WHO, Temperature Sensitivity of Vaccines, 2014. http://www.who.int/immunization/programmes_systems/supply_chain/resources/VaccineStability_EN.pdf. (Accessed Feb 1st 2018).
[104] J. Gomez-Gutierrez, I. Rodriguez-Crespo, J.M. Gonzalez-Ros, J.A. Ferragut, D.A. Paul, D.L. Peterson, F. Gavilanes, Thermal stability of hepatitis B surface antigen S proteins, Biochim Biophys Acta 1119(3) (1992) 225-31.
[105] M. Konar, R. Pajon, P.T. Beernink, A meningococcal vaccine antigen engineered to increase thermal stability and stabilize protective epitopes, Proc Natl Acad Sci U S A 112(48) (2015) 14823-8.
[106] I. Lab, "How do you keep vaccines cool? (Hint: look to space)." 2016. http://www.intellectualventureslab.com/investigate/how-do-you-keep-vaccines-cool-hint-look-to-space. .
[107] H.H. Tam, M.B. Melo, M. Kang, J.M. Pelet, V.M. Ruda, M.H. Foley, J.K. Hu, S. Kumari, J. Crampton, A.D. Baldeon, R.W. Sanders, J.P. Moore, S. Crotty, R. Langer, D.G. Anderson, A.K. Chakraborty, D.J. Irvine, Sustained antigen availability during germinal center initiation enhances antibody responses to vaccination, Proc Natl Acad Sci U S A 113(43) (2016) E6639-E6648.
[108] K.J. McHugh, R. Guarecuco, R. Langer, A. Jaklenec, Single-injection vaccines: Progress, challenges, and opportunities, J Control Release 219 (2015) 596-609.
[109] R. Gautam, Y. Nishimura, A. Pegu, M.C. Nason, F. Klein, A. Gazumyan, J. Golijanin, A. Buckler-White, R. Sadjadpour, K. Wang, Z. Mankoff, S.D. Schmidt, J.D. Lifson, J.R. Mascola, M.C. Nussenzweig, M.A. Martin, A single injection of anti-HIV-1 antibodies protects against repeated SHIV challenges, Nature 533(7601) (2016) 105-109.
[110] C. Lorin, L. Mollet, F. Delebecque, C. Combredet, B. Hurtrel, P. Charneau, M. Brahic, F. Tangy, A single injection of recombinant measles virus vaccines expressing human immunodeficiency virus (HIV) type 1 clade B envelope glycoproteins induces neutralizing antibodies and cellular immune responses to HIV, J Virol 78(1) (2004) 146-57.
[111] G. Boehm, M. Peyre, D. Sesardic, R.J. Huskisson, F. Mawas, A. Douglas, D. Xing, H.P. Merkle, B. Gander, P. Johansen, On technological and immunological benefits of multivalent single-injection microsphere vaccines, Pharm Res 19(9) (2002) 1330-6.
[112] A.A. Murphy, A.J. Redwood, M.A. Jarvis, Self-disseminating vaccines for emerging infectious diseases, Expert Rev Vaccines 15(1) (2016) 31-9.
[113] Y. Fu, W.J. Kao, Drug release kinetics and transport mechanisms of non-degradable and degradable polymeric delivery systems, Expert Opin Drug Deliv 7(4) (2010) 429-44.
[114] S.Y. Tzeng, R. Guarecuco, K.J. McHugh, S. Rose, E.M. Rosenberg, Y. Zeng, R. Langer, A. Jaklenec, Thermostabilization of inactivated polio vaccine in PLGA-based microspheres for pulsatile release, J Control Release 233 (2016) 101-13.

[115] S. Ma, J. Thiele, X. Liu, Y. Bai, C. Abell, W.T. Huck, Fabrication of microgel particles with complex shape via selective polymerization of aqueous two-phase systems, Small 8(15) (2012) 2356-60.
[116] C.H. Choi, D.A. Weitz, C.S. Lee, One step formation of controllable complex emulsions: from functional particles to simultaneous encapsulation of hydrophilic and hydrophobic agents into desired position, Adv Mater 25(18) (2013) 2536-41.
[117] R.H. Schwartz, T cell anergy, Annu Rev Immunol 21 (2003) 305-34.
[118] J. Sun, B. Dirden-Kramer, K. Ito, P.B. Ernst, N. Van Houten, Antigen-specific T cell activation and proliferation during oral tolerance induction, J Immunol 162(10) (1999) 5868-75.
[119] T.M. Fahmy, P.M. Fong, J. Park, T. Constable, W.M. Saltzman, Nanosystems for simultaneous imaging and drug delivery to T cells, AAPS J 9(2) (2007) E171-80.
[120] J.A. Bluestone, A.W. Thomson, E.M. Shevach, H.L. Weiner, What does the future hold for cell-based tolerogenic therapy?, Nat Rev Immunol 7(8) (2007) 650-4.
[121] A. Moreau, E. Varey, G. Beriou, M. Hill, L. Bouchet-Delbos, M. Segovia, M.C. Cuturi, Tolerogenic dendritic cells and negative vaccination in transplantation: from rodents to clinical trials, Front Immunol 3 (2012) 218.
[122] P.H. Lambert, M. Liu, C.A. Siegrist, Can successful vaccines teach us how to induce efficient protective immune responses?, Nat Med 11(4 Suppl) (2005) S54-62.
[123] J. Lee, S. Arun Kumar, W.N. Souery, T. Hinsdale, K.C. Maitland, C.J. Bishop, An ultraviolet-curable, core-shell vaccine formed via phase separation, J Biomed Mater Res A 107(10) (2019) 2160-2173.
[124] S.Y. Tzeng, K.J. McHugh, A.M. Behrens, S. Rose, J.L. Sugarman, S. Ferber, R. Langer, A. Jaklenec, Stabilized single-injection inactivated polio vaccine elicits a strong neutralizing immune response, Proc Natl Acad Sci U S A 115(23) (2018) E5269-E5278.
[125] Z.Z. Li, L.X. Wen, L. Shao, J.F. Chen, Fabrication of porous hollow silica nanoparticles and their applications in drug release control, J Control Release 98(2) (2004) 245-54.
[126] M. Vallet-Regi, M. Colilla, I. Izquierdo-Barba, M. Manzano, Mesoporous Silica Nanoparticles for Drug Delivery: Current Insights, Molecules 23(1) (2017).
[127] M. Bouchoucha, M.-F. Côté, R. C.-Gaudreault, M.-A. Fortin, F. Kleitz, Size-Controlled Functionalized Mesoporous Silica Nanoparticles for Tunable Drug Release and Enhanced Anti-Tumoral Activity, Chemistry of Materials 28(12) (2016) 4243-4258.
[128] I.J. Joye, D.J. McClements, Biopolymer-Based Delivery Systems: Challenges and Opportunities, Curr Top Med Chem 16(9) (2016) 1026-39.
[129] D. Dutta, C. Fauer, K. Hickey, M. Salifu, S.E. Stabenfeldt, Tunable delayed controlled release profile from layered polymeric microparticles, J Mater Chem B 5(23) (2017) 4487-4498.
[130] X. Yu, A.H. Biedrzycki, A.S. Khalil, D. Hess, J.M. Umhoefer, M.D. Markel, W.L. Murphy, Nanostructured Mineral Coatings Stabilize Proteins for Therapeutic Delivery, Adv Mater 29(33) (2017).
[131] K. Fu, A.M. Klibanov, R. Langer, Protein stability in controlled-release systems, Nat Biotechnol 18(1) (2000) 24-5.

[132] S. Frokjaer, D.E. Otzen, Protein drug stability: a formulation challenge, Nat Rev Drug Discov 4(4) (2005) 298-306.
[133] R.T. Bartus, M.A. Tracy, D.F. Emerich, S.E. Zale, Sustained delivery of proteins for novel therapeutic agents, Science 281(5380) (1998) 1161-2.
[134] X. Huang, I.H. El-Sayed, W. Qian, M.A. El-Sayed, Cancer cell imaging and photothermal therapy in the near-infrared region by using gold nanorods, J Am Chem Soc 128(6) (2006) 2115-20.
[135] A. Wijaya, S.B. Schaffer, I.G. Pallares, K. Hamad-Schifferli, Selective release of multiple DNA oligonucleotides from gold nanorods, ACS Nano 3(1) (2009) 80-6.
[136] S. Manohar, C. Ungureanu, T.G. Van Leeuwen, Gold nanorods as molecular contrast agents in photoacoustic imaging: the promises and the caveats, Contrast Media Mol Imaging 6(5) (2011) 389-400.
[137] J.V. Jokerst, A.J. Cole, D. Van de Sompel, S.S. Gambhir, Gold nanorods for ovarian cancer detection with photoacoustic imaging and resection guidance via Raman imaging in living mice, ACS Nano 6(11) (2012) 10366-77.
[138] L. Cai, S. Wang, Poly(ε-caprolactone) acrylates synthesized using a facile method for fabricating networks to achieve controllable physicochemical properties and tunable cell responses, Polymer 51(1) (2010) 164-177.
[139] X.H. Yang, W.L. Zhu, Viscosity properties of sodium carboxymethylcellulose solutions, Cellulose 14(5) (2007) 409-417.
[140] S. Arun Kumar, J. Good, D. Hendrix, E. Yoo, D. Kim, K.A. Deo, Y.Y. Jhan, A.K. Gaharwar, C.J. Bishop, Nanoengineered Light-Activatable Polybubbles for On-Demand Therapeutic Delivery, Adv Funct Mater 30(31) (2020) 2003579.
[141] Y. Hu, L. Zhang, Y. Cao, H. Ge, X. Jiang, C. Yang, Degradation behavior of poly(epsilon-caprolactone)-b-poly(ethylene glycol)-b-poly(epsilon-caprolactone) micelles in aqueous solution, Biomacromolecules 5(5) (2004) 1756-62.
[142] H.J. Sung, C. Meredith, C. Johnson, Z.S. Galis, The effect of scaffold degradation rate on three-dimensional cell growth and angiogenesis, Biomaterials 25(26) (2004) 5735-42.
[143] S. Lyu, D. Untereker, Degradability of polymers for implantable biomedical devices, Int J Mol Sci 10(9) (2009) 4033-65.
[144] L. Wu, J. Ding, Effects of porosity and pore size on in vitro degradation of three-dimensional porous poly(D,L-lactide-co-glycolide) scaffolds for tissue engineering, J Biomed Mater Res A 75(4) (2005) 767-77.
[145] M.G. Soliman, B. Pelaz, W.J. Parak, P. del Pino, Phase Transfer and Polymer Coating Methods toward Improving the Stability of Metallic Nanoparticles for Biological Applications, Chemistry of Materials 27(3) (2015) 990-997.
[146] W. Albrecht, T.S. Deng, B. Goris, M.A. van Huis, S. Bals, A. van Blaaderen, Single Particle Deformation and Analysis of Silica-Coated Gold Nanorods before and after Femtosecond Laser Pulse Excitation, Nano Lett 16(3) (2016) 1818-25.
[147] S.-S. Chang, C.-W. Shih, C.-D. Chen, W.-C. Lai, C.R.C. Wang, The Shape Transition of Gold Nanorods, Langmuir 15(3) (1999) 701-709.

[148] S. Link, C. Burda, M.B. Mohamed, B. Nikoobakht, M.A. El-Sayed, Laser Photothermal Melting and Fragmentation of Gold Nanorods: Energy and Laser Pulse-Width Dependence, The Journal of Physical Chemistry A 103(9) (1999) 1165-1170.
[149] Polymer Analysis by NMR, Sigma-Aldrich, Milwaukee, WI, 2006.
[150] J. Lee, S. Arun Kumar, W.N. Souery, T. Hinsdale, K.C. Maitland, C.J. Bishop, An ultraviolet-curable, core-shell vaccine formed via phase separation, J Biomed Mater Res A (2019).
[151] M.S. Ibrahim, N.A. El-Wassefy, D.S. Farahat, 8 - Biocompatibility of dental biomaterials, in: L. Tayebi, K. Moharamzadeh (Eds.), Biomaterials for Oral and Dental Tissue Engineering, Woodhead Publishing2017, pp. 117-140.
[152] S. Kittler, S. Hickey, T. Wolff, A. Eychmüller, Easy and Fast Phase Transfer of CTAB Stabilised Gold Nanoparticles from Water to Organic Phase, 2015.
[153] R.D. Near, S.C. Hayden, R.E. Hunter, D. Thackston, M.A. El-Sayed, Rapid and Efficient Prediction of Optical Extinction Coefficients for Gold Nanospheres and Gold Nanorods, The Journal of Physical Chemistry C 117(45) (2013) 23950-23955.
[154] T.A. Henderson, L.D. Morries, Multi-Watt Near-Infrared Phototherapy for the Treatment of Comorbid Depression: An Open-Label Single-Arm Study, Front Psychiatry 8 (2017) 187.
[155] O. Erol, I. Uyan, M. Hatip, C. Yilmaz, A.B. Tekinay, M.O. Guler, Recent advances in bioactive 1D and 2D carbon nanomaterials for biomedical applications, Nanomedicine 14(7) (2018) 2433-2454.
[156] Y. Huang, P. Chen, Nanoelectronic biosensing of dynamic cellular activities based on nanostructured materials, Adv Mater 22(25) (2010) 2818-23.
[157] D. Chimene, D.L. Alge, A.K. Gaharwar, Two-Dimensional Nanomaterials for Biomedical Applications: Emerging Trends and Future Prospects, Adv Mater 27(45) (2015) 7261-84.
[158] K. Song, Q. Wu, Z. Zhang, S. Ren, T. Lei, Negulescu, II, Q. Zhang, Porous Carbon Nanofibers from Electrospun Biomass Tar/Polyacrylonitrile/Silver Hybrids as Antimicrobial Materials, ACS Appl Mater Interfaces 7(27) (2015) 15108-16.
[159] L. Zhang, A. Aboagye, A. Kelkar, C. Lai, H. Fong, A review: carbon nanofibers from electrospun polyacrylonitrile and their applications, Journal of Materials Science 49(2) (2014) 463-480.
[160] J. He, W. Wang, F. Sun, W. Shi, D. Qi, K. Wang, R. Shi, F. Cui, C. Wang, X. Chen, Highly Efficient Phosphate Scavenger Based on Well-Dispersed La(OH)3 Nanorods in Polyacrylonitrile Nanofibers for Nutrient-Starvation Antibacteria, ACS Nano 9(9) (2015) 9292-302.
[161] J. Hou, J. Yun, H. Byun, Fabrication and Characterization of Modified Graphene Oxide/PAN Hybrid Nanofiber Membrane, Membranes (Basel) 9(9) (2019).
[162] F. Mehrpouya, J. Foroughi, S. Naficy, J.M. Razal, M. Naebe, Nanostructured Electrospun Hybrid Graphene/Polyacrylonitrile Yarns, Nanomaterials (Basel) 7(10) (2017).
[163] J. Xu, A. Gulzar, Y. Liu, H. Bi, S. Gai, B. Liu, D. Yang, F. He, P. Yang, Integration of IR-808 Sensitized Upconversion Nanostructure and MoS2 Nanosheet for 808 nm NIR Light Triggered Phototherapy and Bioimaging, Small 13(36) (2017).

[164] S. Su, H. Sun, W. Cao, J. Chao, H. Peng, X. Zuo, L. Yuwen, C. Fan, L. Wang, Dual-Target Electrochemical Biosensing Based on DNA Structural Switching on Gold Nanoparticle-Decorated MoS2 Nanosheets, ACS Appl Mater Interfaces 8(11) (2016) 6826-33.
[165] D. Sarkar, W. Liu, X. Xie, A.C. Anselmo, S. Mitragotri, K. Banerjee, Correction to MoS2 Field-Effect Transistor for Next-Generation Label-Free Biosensors, ACS Nano 8(5) (2014) 5367-5367.
[166] W. Yin, L. Yan, J. Yu, G. Tian, L. Zhou, X. Zheng, X. Zhang, Y. Yong, J. Li, Z. Gu, Y. Zhao, High-throughput synthesis of single-layer MoS2 nanosheets as a near-infrared photothermal-triggered drug delivery for effective cancer therapy, ACS Nano 8(7) (2014) 6922-33.
[167] S. Wang, Y. Chen, X. Li, W. Gao, L. Zhang, J. Liu, Y. Zheng, H. Chen, J. Shi, Injectable 2D MoS2 -Integrated Drug Delivering Implant for Highly Efficient NIR-Triggered Synergistic Tumor Hyperthermia, Adv Mater 27(44) (2015) 7117-22.
[168] X. Li, H. Zhu, Two-dimensional MoS2: Properties, preparation, and applications, Journal of Materiomics 1(1) (2015) 33-44.
[169] W. Yin, J. Yu, F. Lv, L. Yan, L.R. Zheng, Z. Gu, Y. Zhao, Functionalized Nano-MoS2 with Peroxidase Catalytic and Near-Infrared Photothermal Activities for Safe and Synergetic Wound Antibacterial Applications, ACS Nano 10(12) (2016) 11000-11011.
[170] B. Liu, C. Li, G. Chen, B. Liu, X. Deng, Y. Wei, J. Xia, B. Xing, P. Ma, J. Lin, Synthesis and Optimization of MoS2@Fe3O4-ICG/Pt(IV) Nanoflowers for MR/IR/PA Bioimaging and Combined PTT/PDT/Chemotherapy Triggered by 808 nm Laser, Adv Sci (Weinh) 4(8) (2017) 1600540.
[171] T. Liu, Z. Liu, 2D MoS2 Nanostructures for Biomedical Applications, Advanced Healthcare Materials 7(8) (2018) 1701158.
[172] R. Kurapati, L. Muzi, A.P.R. de Garibay, J. Russier, D. Voiry, I.A. Vacchi, M. Chhowalla, A. Bianco, Enzymatic Biodegradability of Pristine and Functionalized Transition Metal Dichalcogenide MoS2 Nanosheets, Advanced Functional Materials 27(7) (2017) 1605176.
[173] M.K. Jaiswal, K.A. Singh, G. Lokhande, A.K. Gaharwar, Superhydrophobic states of 2D nanomaterials controlled by atomic defects can modulate cell adhesion, Chem Commun (Camb) 55(60) (2019) 8772-8775.
[174] M. Inagaki, Y. Yang, F. Kang, Carbon nanofibers prepared via electrospinning, Adv Mater 24(19) (2012) 2547-66.
[175] L.S. Lussier, C. Sandorfy, H. Le Thanh, D. Vocelle, Effect of acids on the infrared spectra of the Schiff base of trans-retinal, The Journal of Physical Chemistry 91(9) (1987) 2282-2287.
[176] E. Frackowiak, F. Béguin, Carbon materials for the electrochemical storage of energy in capacitors, Carbon 39(6) (2001) 937-950.
[177] B.E. Conway, V. Birss, J. Wojtowicz, The role and utilization of pseudocapacitance for energy storage by supercapacitors, Journal of Power Sources 66(1) (1997) 1-14.

[178] Cancer Facts & Figures 2021. https://www.cancer.org/content/dam/cancer-org/research/cancer-facts-and-statistics/annual-cancer-facts-and-figures/2021/cancer-facts-and-figures-2021.pdf. 2021).
[179] U.S. Breast Cancer Statistics. https://www.breastcancer.org/symptoms/understand_bc/statistics. 2021).
[180] R. Demicheli, M.W. Retsky, W.J. Hrushesky, M. Baum, I.D. Gukas, The effects of surgery on tumor growth: a century of investigations, Ann Oncol 19(11) (2008) 1821-8.
[181] W. Ceelen, P. Pattyn, M. Mareel, Surgery, wound healing, and metastasis: recent insights and clinical implications, Crit Rev Oncol Hematol 89(1) (2014) 16-26.
[182] D.A. Mahvi, R. Liu, M.W. Grinstaff, Y.L. Colson, C.P. Raut, Local Cancer Recurrence: The Realities, Challenges, and Opportunities for New Therapies, CA Cancer J Clin 68(6) (2018) 488-505.
[183] A. Arora, G. Aggarwal, J. Chander, P. Maman, M. Nagpal, Drug eluting sutures: A recent update, Journal of Applied Pharmaceutical Science 9(07) (2019) 111-123.
[184] B. Joseph, A. George, S. Gopi, N. Kalarikkal, S. Thomas, Polymer sutures for simultaneous wound healing and drug delivery – A review, International Journal of Pharmaceutics 524(1) (2017) 454-466.
[185] X. Deng, M. Qasim, A. Ali, Engineering and polymeric composition of drug-eluting suture: A review, J Biomed Mater Res A (2021).
[186] B. Zhuang, T. Chen, Z. Xiao, Y. Jin, Drug-loaded implantable surgical cavity-adaptive hydrogels for prevention of local tumor recurrence, Int J Pharm 577 (2020) 119048.
[187] P. Ghasemiyeh, S. Mohammadi-Samani, Hydrogels as Drug Delivery Systems; Pros and Cons, Trends in Pharmaceutical Sciences 5(1) (2019) 7-24.
[188] Q. Zhan, B. Shen, X. Deng, H. Chen, J. Jin, X. Zhang, C. Peng, H. Li, Drug-eluting scaffold to deliver chemotherapeutic medication for management of pancreatic cancer after surgery, Int J Nanomedicine 8 (2013) 2465-72.
[189] S. Kuramitsu, K. Motomura, A. Natsume, T. Wakabayashi, Double-edged Sword in the Placement of Carmustine (BCNU) Wafers along the Eloquent Area: A Case Report, NMC Case Rep J 2(1) (2015) 40-45.
[190] Recurrent Glioblastoma Multiforme. https://www.gliadel.com/hcp/recurrent-gbm.php. (Accessed May 8 2021).
[191] A.J. Boyle, T.L. Landsman, M.A. Wierzbicki, L.D. Nash, W. Hwang, M.W. Miller, E. Tuzun, S.M. Hasan, D.J. Maitland, In vitro and in vivo evaluation of a shape memory polymer foam-over-wire embolization device delivered in saccular aneurysm models, J Biomed Mater Res B Appl Biomater 104(7) (2016) 1407-15.
[192] Shape Memory Medical Receives FDA clearance for the IMPEDE FX EMbolization Plug, 2019. https://www.businesswire.com/news/home/20190528005080/en/Shape-Memory-Medical-Receives-FDA-Clearance-IMPEDE%C2%AE.
[193] P. Singhal, J.N. Rodriguez, W. Small, S. Eagleston, J. Van de Water, D.J. Maitland, T.S. Wilson, Ultra Low Density and Highly Crosslinked Biocompatible Shape Memory Polyurethane Foams, J Polym Sci B Polym Phys 50(10) (2012) 724-737.

[194] S.M. Hasan, L.D. Nash, D.J. Maitland, Porous shape memory polymers: Design and applications, Journal of Polymer Science Part B: Polymer Physics 54(14) (2016) 1300-1318.
[195] J.N. Rodriguez, M.W. Miller, A. Boyle, J. Horn, C.K. Yang, T.S. Wilson, J.M. Ortega, W. Small, L. Nash, H. Skoog, D.J. Maitland, Reticulation of low density shape memory polymer foam with an in vivo demonstration of vascular occlusion, J Mech Behav Biomed Mater 40 (2014) 102-114.
[196] G. Rivera-Hernandez, M. Antunes-Ricardo, P. Martinez-Morales, M.L. Sanchez, Polyvinyl alcohol based-drug delivery systems for cancer treatment, Int J Pharm 600 (2021) 120478.
[197] R. Shaikh, T.R. Raj Singh, M.J. Garland, A.D. Woolfson, R.F. Donnelly, Mucoadhesive drug delivery systems, J Pharm Bioallied Sci 3(1) (2011) 89-100.
[198] Acriflavine, 2017. https://go.drugbank.com/drugs/DB13373. 2021).
[199] S. Alrushaid, C.L. Sayre, J.A. Yáñez, M.L. Forrest, S.N. Senadheera, F.J. Burczynski, R. Löbenberg, N.M. Davies, Pharmacokinetic and Toxicodynamic Characterization of a Novel Doxorubicin Derivative, Pharmaceutics 9(3) (2017) 35.
[200] D.R. Perinelli, M. Cespi, G. Bonacucina, F. Rendina, G.F. Palmieri, Heating treatments affect the thermal behaviour of doxorubicin loaded in PEGylated liposomes, Int J Pharm 534(1-2) (2017) 81-88.
[201] A.G. Porter, R.U. Jänicke, Emerging roles of caspase-3 in apoptosis, Cell Death Differ 6(2) (1999) 99-104.

APPENDIX A

SUPPORTING INFORMATION FOR CHAPTER 2

A1.1 Introduction

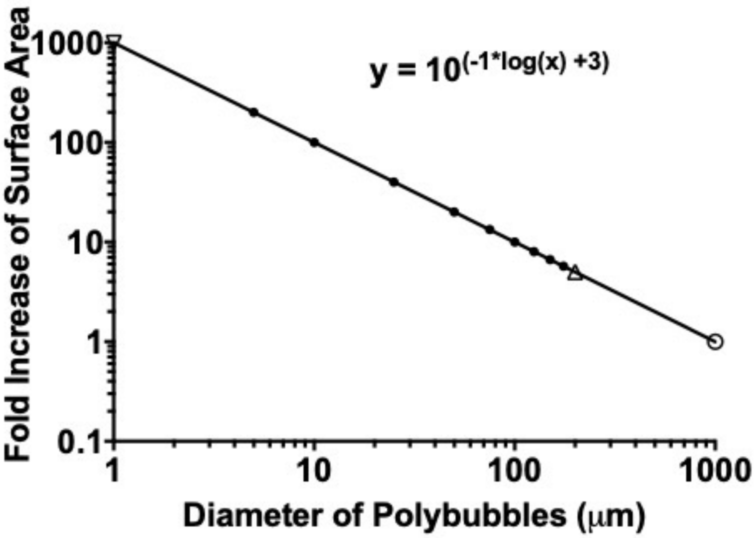

Figure S1: Ratio of surface area that is exposed to organic solvent as it relates to the diameter of polybubbles to deliver the same amount of cargo as the polybubble with a diameter of 1000 μm (O) that is produced using our platform. Polybubbles with diameters of 0.01 μm (▽) and 200 μm (△) are the lower and higher limit that can be produced using microfluidic system, respectively. Reprinted with permission from John Wiley and Sons from Lee *et al.*[123]

A1.2 MATERIALS

1-Step™ Ultra Tetramethylbezidine (TMB)-Enzyme-Linked Immunosorbent Assay (ELISA) Substrate Solution (Thermo scientific); 2-Hydroxy-2-methylpropiophenone (TCI AMERICA); 450 nm Stop Solution for TMB Substrate (ab171529); acryloyl chloride (Alfa Aesar); acriflavine (Chem-Impex International); anhydrous ethyl ether (Fisher Chemical); Anti-HIV1 gp120 antibody conjugated to horseradish peroxidase (HRP) (ab53840); Bovine serum albumin (BSA) (Fisher BioReagents); BSA-CF488 dye conjugates (Biotium); Carboxymethylcellulose (CMC; sodium salt, low viscosity) (Millipore Sigma); Chloroform (Fisher Chemical); Coating buffer (ab210899);

Dichloromethane (DCM) (ACROS Organics*);* doxorubicin hydrochloride (Fisher BioReagents); K_2CO_3 (ACROS Organics); Legato 100 Syringe Pump (KD Scientific); Nonfat dry milk (Andwin Scientific); poly(caprolactone)triol (PCL triol, average MW 300 Da) (ACROS Organics); poly(ε-caprolactone) (PCL, average Mn 14 kDa and 45kDa) (Sigma Aldrich); Recombinant HIV1 gp120 + gp41 protein (ab49054); Tin(II) 2-ethylhexanoate (96% SO) (Alfa Aesar); Trehalose (Acros Organics).

A1.3 Methods

Formation of PCL polybubbles (80 kDa) – 80 kDa PCL was dissolved in chloroform at the following concentrations: 100 mg/mL, 400 mg/mL, 600 mg/mL, 800 mg/mL, and 1000 mg/mL (not accounting for polymer volume; thus these concentrations would be 90.9, 286, 375, 444, and 500 mg/mL, respectively, when accounting for polymer volume). Each polymer was aspirated from a primary container into a 250 mL glass barrel using a 21 G needle. A nickel titanium alloy (Nitinol) tube was used for injecting the organic solvent phase containing the solvated polymer into the water phase. The Nitinol tubing and a Luer lock were glued together using epoxy glue and was allowed to dry overnight before use. The borosilicate glass vial was filled with deionized (DI) water, and polymer was then injected into the vial through the Nitinol tube via a syringe pump. The polymer injection rate of the syringe was controlled at a rate of 0.5 µL/sec. The resulting bubble was frozen in liquid nitrogen for 20 minutes and lyophilized overnight. The polybubble surface was then analyzed by scanning electron microscopy (SEM). The inner portions of the polybubbles made with the highest polymer concentration (1000 mg/mL) were imaged by breaking the polybubbles with forceps.

Poly(ε-caprolactone) triacrylate Synthesis – K_2CO_3, PCL triol, and acryloyl chloride were qualified in a 3:1:3 molar ratio. 4.1463 g of K_2CO_3 were dried in a 97.5 °C oven overnight. 3.2 mL of PCL triol stock were placed in a round bottom flask and also dried overnight under reduced pressure at 50 °C using a secondary mineral oil container. For the synthesis, a 2-fold volume excess of DCM was added to the PCL triol and continuously stirred at room temperature. The K_2CO_3 was then added to the PCL triol. 2.72 mL of acryloyl chloride was mixed with a 10-fold volume excess of DCM, and this mixture was then added to the mixture of K_2CO_3 and PCL triol in a dropwise fashion.

The reaction was allowed to proceed for 24 hours, after which the mixture was vacuum-filtered. To purify the product, the filtered mixture was added drop-by-drop in a 3-fold volume excess of diethyl ether, which was contained in a secondary container functioning as an ice bath. After overnight storage in a vacuum chamber, the purified poly(*ε*-caprolactone) triacrylate (PCLTA) product was collected.

NMR was used to confirm the acrylate peaks in the final PCLTA product. The synthesis of PCLTA is described in the synthesis scheme shown in **Figure S2**.

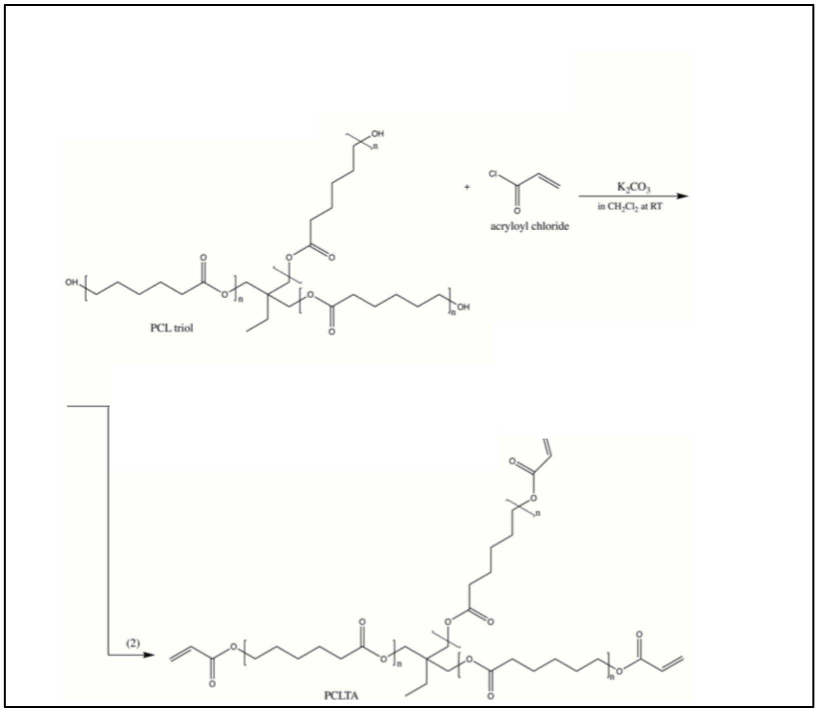

Figure S2. Synthesis of PCL triacrylate using K_2CO_3 in DCM at room temperature.

Curing PCL/PCLTA polybubbles. Reprinted with permission from John Wiley and Sons from Lee *et al.* [123]

PCL (Mn = 14 kDa) was dissolved in chloroform at a concentration of 600 mg/mL. This PCL solution was mixed with the previously synthesized PCLTA at the following volume ratios: PCL: PCLTA=1:0, 1:1, 1:3, 3:1, and 0:1. The photoinitiator was dissolved in chloroform at a concentration of 5 mg/mL (or 0.5%, assuming the density of water). The 50 μL photoinitiator solution was then added into each of the various mixtures of PCL/PCLTA.

Prior to curing, 150 μL of each mixture was added into the caps of 0.5 mL tubes. Each of the caps were also filled with acrylate-terminated and non-acrylate-terminated polymers at varying ratios, which were then cured under the ultraviolet (UV) lamp for 20 minutes in an inert argon atmosphere.

To determine the minimum time required for curing, PCL (14 kDa; 800 mg/mL) : PCLTA:photoinitiator (5 mg/mL) was mixed in a 1:2:1 volume ratio. 150 μL of the PCL/PCLTA and photoinitiator mixtures were added to each of the 0.5 mL tube caps. Each of the solutions were cured under the UV lamp for 5, 10, 15 and 20 minutes.

Quantification of the effect of UV curing time on the viscoelastic properties of the polybubbles- To determine the effect of UV curing time on the viscoelastic properties, polybubbles were cured using three different energy per area values (12.5, 40.5, 63.25 J/cm^2). Different energy per area values were obtained by differing the curing times (3,10, and 15 minutes) at a constant power density (70mW/cm^2). Cured polybubbles were then flash frozen and lyophilized overnight. Polybubbles were then analyzed using frequency sweep setting at 37°C in DMA (compression mode) to determine the storage and loss modulus of the polybubbles. One-way ANOVA was used to determine statistical significance.

HEMA/TEGDA/PEGMA hydrogels for polybubble localization – To determine the effectiveness of HEMA/triethylene glycol diacrylate (TEGDA)/polyethylene glycol methylacrylate (PEGMA) for maintaining polybubble location during the cargo injection process, three different hydrogels were synthesized and tested. Before initiating the synthesis, HEMA and TEGDA were passed through an inhibitor remover column, and the solutions were collected in glass vials. 5 mg of 2,2-dimethoxy-2-phenylacetophonone, 10 µL of TEGDMA, and 490 µL of HEMA were added together. 180 µL of ethylene glycol was added as a solvent and mixed. 100 µL, 200 µL, and 300 µL of water were added to render varying rigidities. The polymer was cured under UV light for 10 minutes. The PCL/PCLTA polybubbles were injected using a 25 G needle.

Use of HEMA hydrogel + 1.5% CMC solution for polybubble localization – CMC was dissolved in DI water as a 3% (w/v) solution. 3% CMC solution and HEMA hydrogel were mixed in a 1:1 volume ratio using the same HEMA gel formulation described previously. The mixture of HEMA and CMC was then cured under UV light for 15 minutes. The PCL/PCLTA polybubbles were injected through a syringe pump at a rate of 0.5 µL/sec.

Use of trehalose solution for polybubble localization – A 60% (w/v) trehalose solution was prepared by dissolving 6 mg of trehalose in 10 mL of DI water. Because ~68% (w/v) is the solubility limit of trehalose, using a 60% (w/v) solution allows for the solution to be highly viscous while completely solvating the trehalose. The PCL/PCLTA polybubbles were injected at a syringe pump rate of 0.5 µL/sec.

Use of 5% and 10% CMC solutions for polybubble localization – 5% and 10% (w/v) CMC solutions were prepared by dissolving CMC in DI water. The PCL/PCLTA polybubble was injected through the syringe pump at a rate of 0.5 µL/sec.

Quantifying polybubble diameter pre- and post-lyophilization and pre-and post-cargo injection – The PCL/PCLTA mixture was prepared in the manner previously described above. The polymer was then loaded into a 250 μL glass barrel. The glass vial was filled with 10% (w/v) CMC, and the polymer was dispensed from the syringe pump at a rate of 0.5 μL/sec. After the polybubbles were formed, they were cured under UV light for 10 minutes.

Photographs of the polybubbles within the glass vials were taken, and the polybubble diameters were quantified via ImageJ using an electronic micrometer for calibration. After lyophilization, the polybubble diameters were quantified via ImageJ using the same calibration method as before. It is important to note that it is not possible to quantify the diameters of the pre-cured polybubbles with the micrometer because they are in liquid form at that stage.

In regards to pre- and post-cargo injection, The PCL/PCLTA mixture was prepared in the manner previously described above. The polymer was then loaded into a 250 μL glass barrel. The glass vial was filled with 10% (w/v) CMC, and the polymer was dispensed from the syringe pump at a rate varying from 0.0005 μL/sec to 1 μL/sec. After the polybubbles were formed, 1% acriflavine in 5% CMC was injected into each of the polybubbles using a 34 G needle. Photos were taken of the polybubbles in the glass vial both before and after injection, and the polybubble diameters were quantified via ImageJ using the same calibration method as before.

Defining ELISA **protocols** - HIV1 gp120/41 antigen was diluted in a coating buffer at 1.25 μg/mL and loaded onto a 96-well plate. Serial dilution of half concentration was performed so that each well contained 50 μL of antigen solution. The plate was incubated for 2 hours at room temperature on a plate shaker at 400 RPM. After incubation, the plate was washed three times using 300 μL PBS for 5 minutes on a plate shaker at 400 RPM. 300 μL of 5% (w/v) nonfat dry milk solution was loaded and incubated overnight at 4 °C to prevent non-specific antibody binding. Blocking solution was washed twice with the same methods as antigen washing. Anti-HIV1 gp120/41 antibody-HRP conjugates were diluted at 1:800 and loaded at a volume of 100 μL. After 2 hours of incubation at room temperature, the plate was washed three times with the same methods as antigen washing. 100 µL of tetramethylbenzidine solution was loaded and incubated for 15 minutes at room temperature, and the plate was covered with foil. 100 µL of stop solution was added, and the absorbance was read 10 minutes later at 450 nm.

A1.4 Results

Optimization of PCL/PCLTA polybubble UV curing time - To determine which PCL/PLCTA ratio optimized polybubble curing, a qualitative rigidity test was developed and applied to the polybubbles. Pipette tips were used to probe the polybubble surface and judge the polymer's relative degree of rigidity. Based on this test, the polymer mixture with the lowest PCL:PCLTA ratio had the greatest degree of rigidity following curing, as indicated by the fact that polybubbles with a 0:1 PCL/PCLTA ratio could not be punctured using pipette tips. In contrast, polybubbles with a 1:0 PCL/PCLTA ratio were not cured at all, and the soft surface of the polybubbles could easily be deformed with a pipette tip.

To determine how long the PCL/PLCTA polybubbles should be cured, the qualitative rigidity test was applied again. After polybubbles were cured for 5 minutes, the qualitative rigidity assessment indicated that only the surface of the polymer was cured, and the polybubbles were easily broken as a result. After the polybubbles were cured for 10 minutes, the qualitative rigidity assessment indicated that all of the polymer had cured, and it was difficult to puncture the surface using pipette tips. Therefore, the UV curing process was used for 10 minutes on every polybubble to standardize polybubble rigidity.

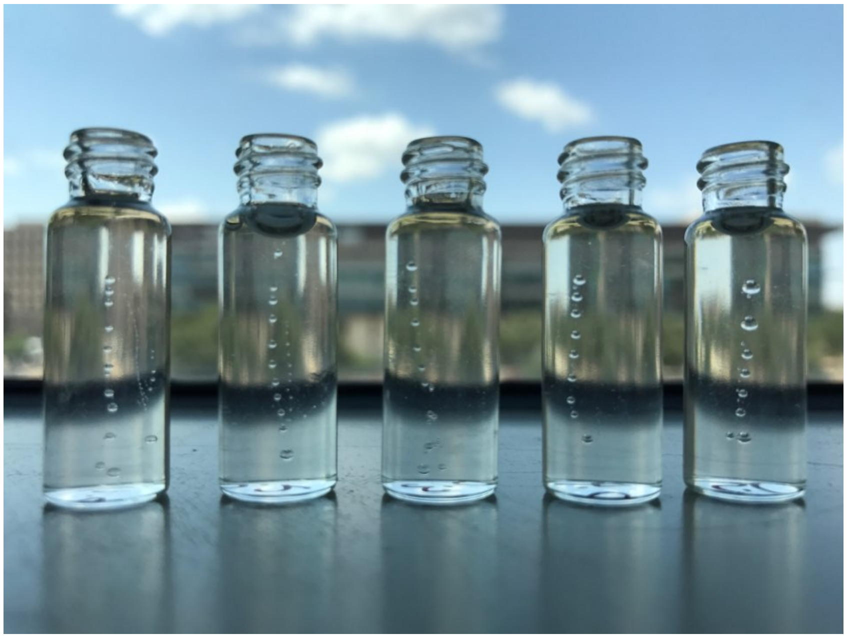

Figure S3. Polybubble diameter comparisons dictated by the syringe pump rate. Reprinted with permission from John Wiley and Sons from Lee *et al.* [123]

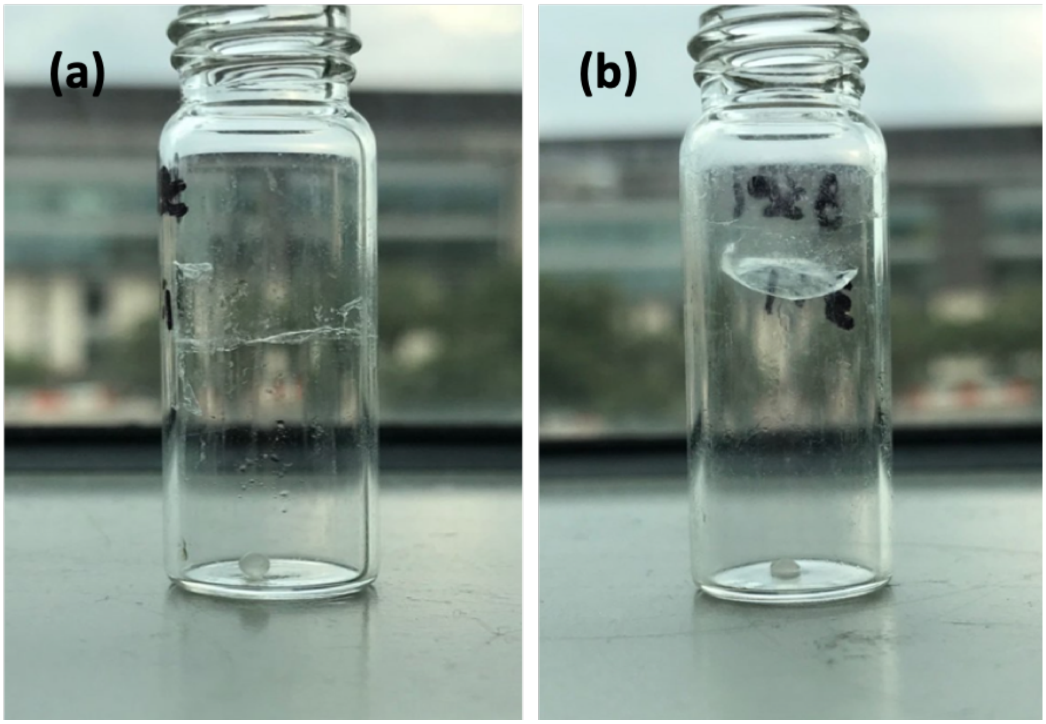

Figure S4. Shape of polybubbles formed in the water: (a) 80 kDa PCL polybubble after lyophilization (UV curing was previously done on this and did not cure as expected so was not done so in this particular experiment) and (b) 14 kDa PCL/PCLTA microbubble after UV curing and lyophilization. Reprinted with permission from John Wiley and Sons from Lee *et al.* [123]

Quantification of the effect of UV curing time on the viscoelastic properties of the polybubbles- Similar viscoelastic properties were observed for polybubbles cured at different energy per area values (Figure S5). There was no statistical significance between the three groups for storage modulus and loss modulus. Three different curing times were chosen to confirm that 10 minutes is sufficient to cure the polybubbles. Curing times (3,10, and 15 minutes) corresponding to 12.5, 40.5, and 63.25J/cm^2 are equivalent to 1/3, 1, and 3/2 times of the time point (10 minutes) that was used to cure the polybubbles used in all the studies. Because there is no statistical significance in the viscoelastic properties of the polybubbles in the three groups it can be concluded that the 10 minutes is sufficient to maintain the rigidity of the polybubbles.

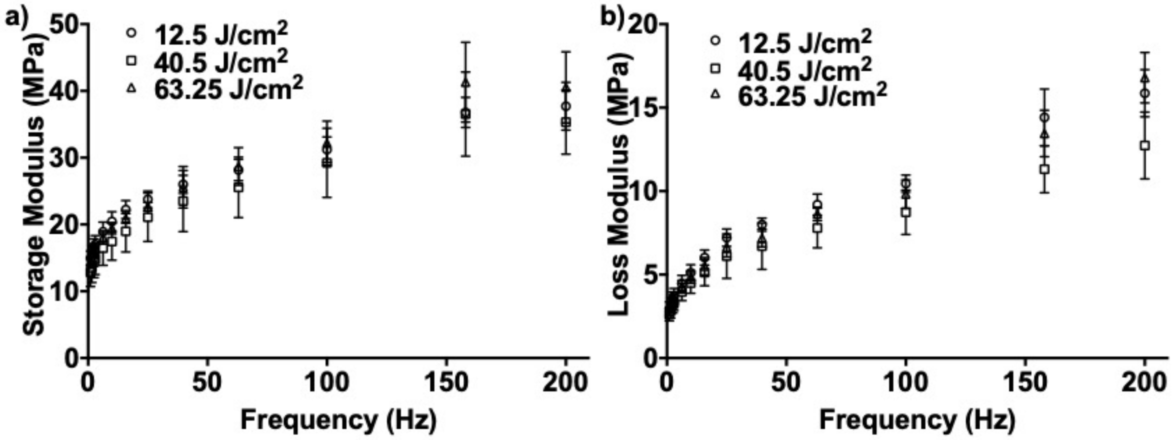

Figure S5. a) Storage modulus and **b)** loss modulus of polybubbles that were cured at different energy per area values. Reprinted with permission from John Wiley and Sons from Lee *et al.* [123]

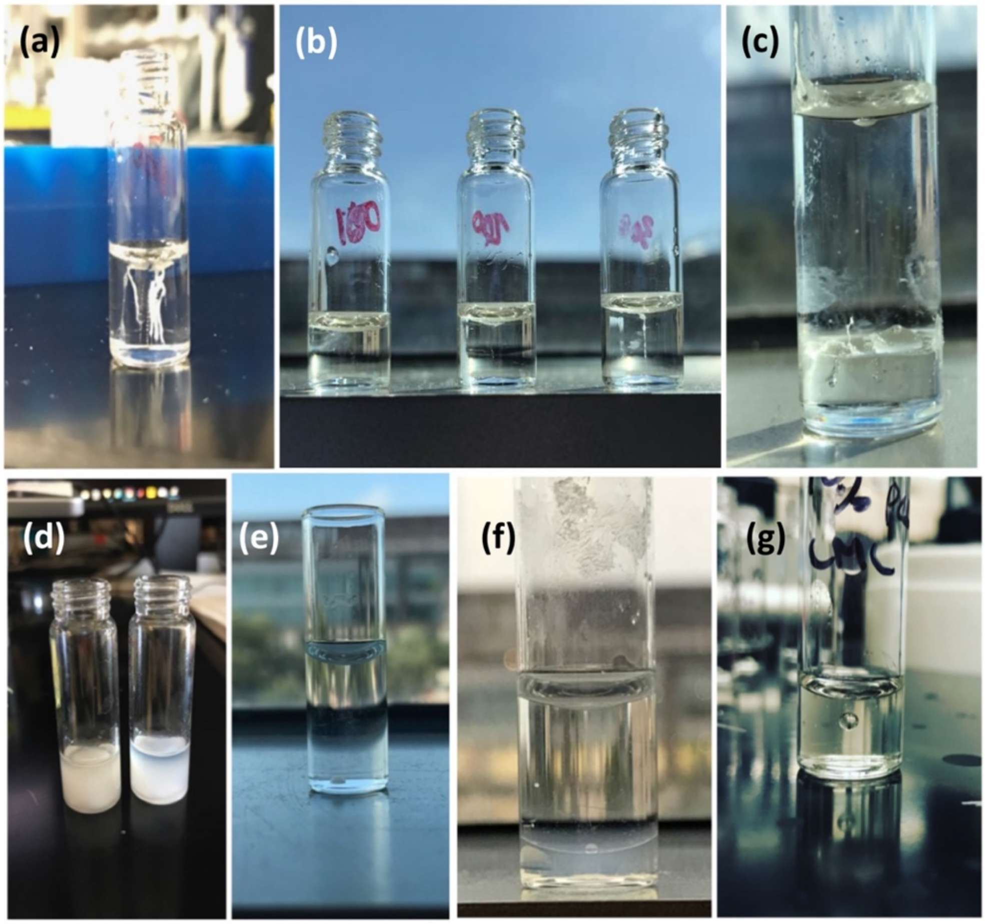

Figure S6. PCL/PCLTA polymer was injected in (a) PEG hydrogel and the polymer followed the path of the needle (b) a HEMA hydrogel with 13% (left), 23% (middle), and 31% (right) v/v water content; in (c) half-cured HEMA hydrogel (UV light directed from the top; the bottom portion likely cured first because it had less oxygen near the bottom of the vial; top contains uncured HEMA precursors) (d) HEMA+1.5% (final) CMC and subsequently cured (e) 60% (w/v) trehalose (f) agarose gel on the bottom with pure water atop (g) 10% CMC. Reprinted with permission from John Wiley and Sons from Lee *et al.* [123]

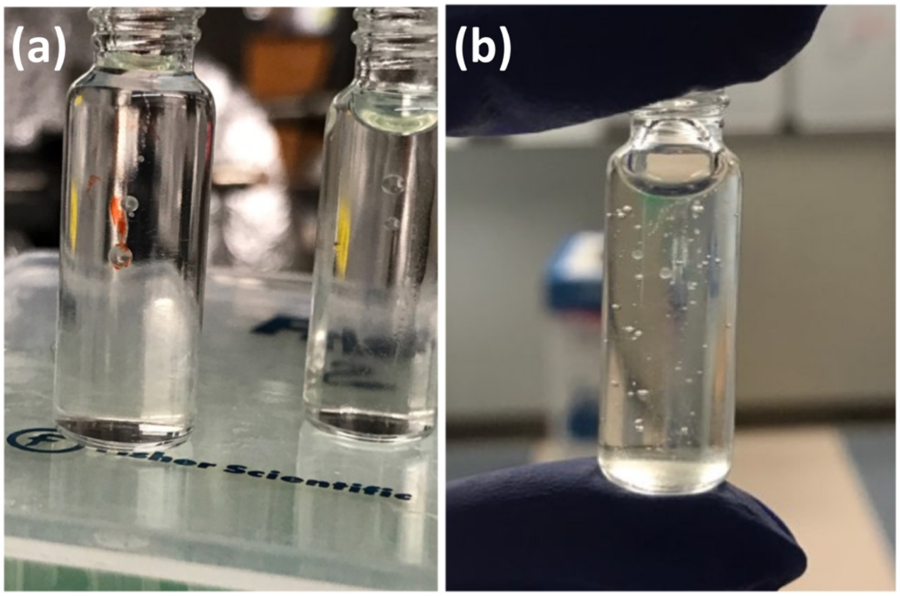

Figure S7. Cargos without CMC (a) 1% doxorubicin (b) BSA-CF680. Reprinted with permission from John Wiley and Sons from Lee *et al.* [123]

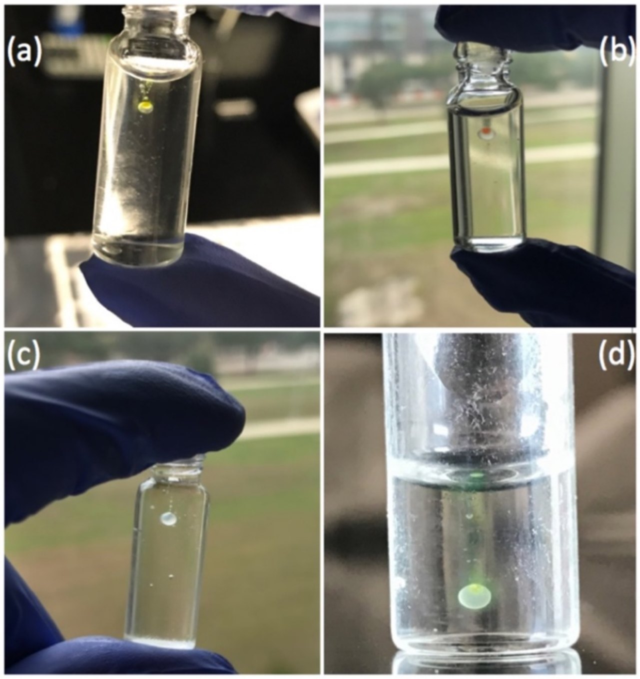

Figure S8. Inner cargo bubbles injected with 3% CMC within the microbubbles using (a) 1% (w/v) acriflavine (b) 1%(w/v) doxorubicin (c) BSA-CF680 (d) 1% (w/v) acriflavine after UV curing. Reprinted with permission from John Wiley and Sons from Lee *et al.* [123]

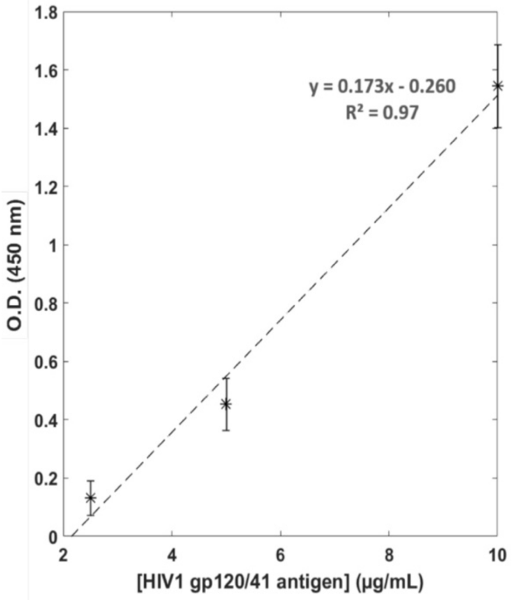

Figure S9. ELISA calibration curve of HIV-1 gp120/41. Reprinted with permission from John Wiley and Sons from Lee *et al.* [123]

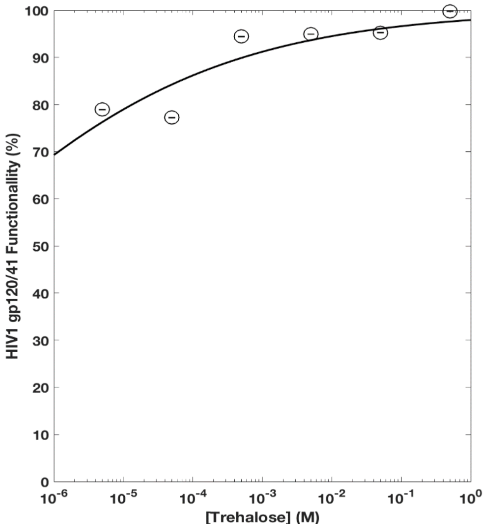

Figure S10. Correlation between HIV-1 gp120/41 antigen functionality and trehalose concentrations on day 4. Reprinted with permission from John Wiley and Sons from Lee *et al.* [123]

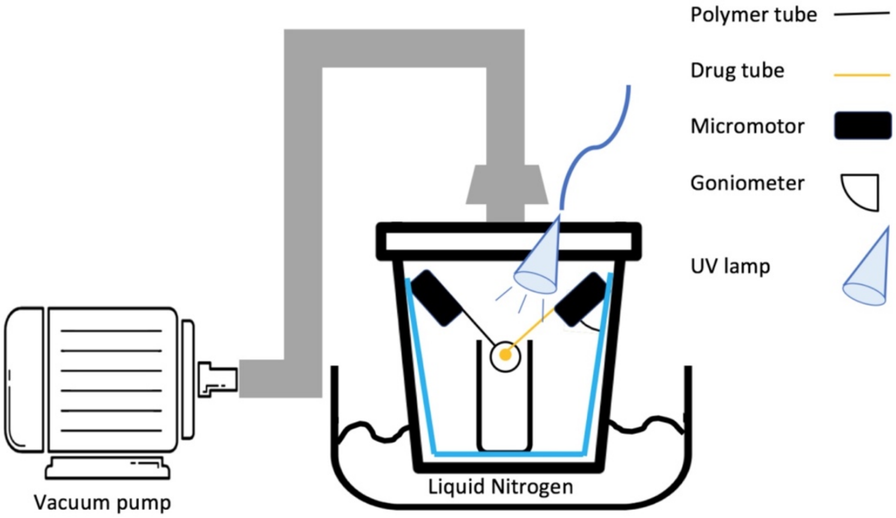

Figure S11. Automation: The design of the self-contained lyophilization system for polybubble formation. Reprinted with permission from John Wiley and Sons from Lee *et al.* [123]

APPENDIX B

SUPPORTING INFORMATION FOR CHAPTER 3

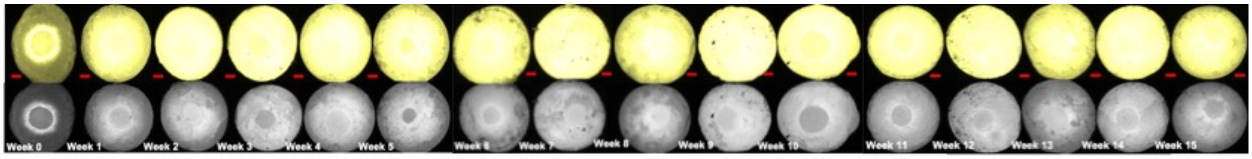

Figure S1. Fluorescence images used to study diffusion of small molecules from polybubbles with centered acriflavine that were incubated in PBS for weeks 1 to 15. Reprinted with permission from John Wiley and Sons from Arun Kumar *et al.* [140]

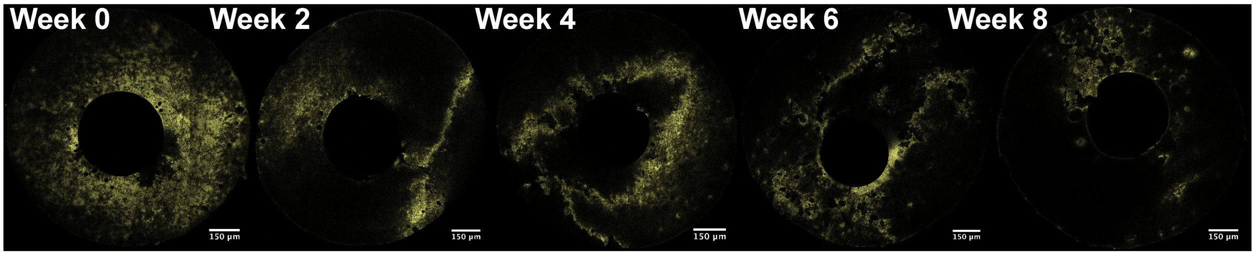

Figure S2. Fluorescence images of PCL polybubbles with acriflavine in the shell to visualize porosity of polybubbles in time. Reprinted with permission from John Wiley and Sons from Arun Kumar *et al.* [140]

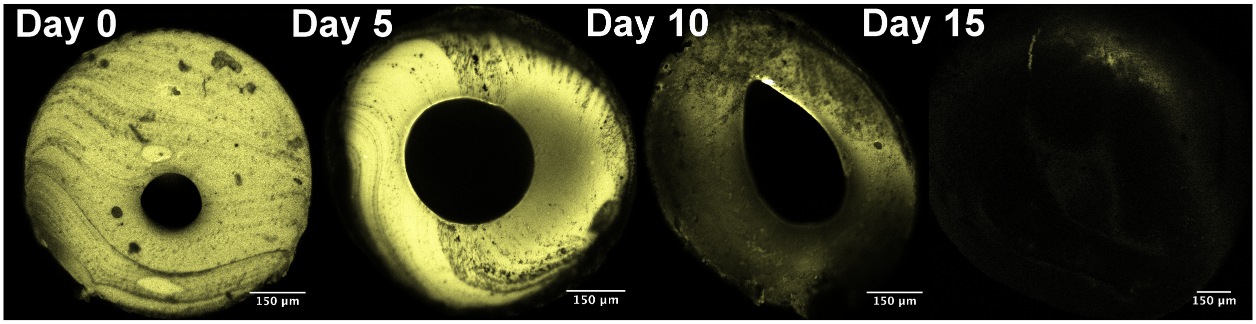

Figure S3. Fluorescence images of PLGA polybubbles with acriflavine in the shell to visualize porosity of polybubbles in time. Reprinted with permission from John Wiley and Sons from Arun Kumar *et al.* [140]

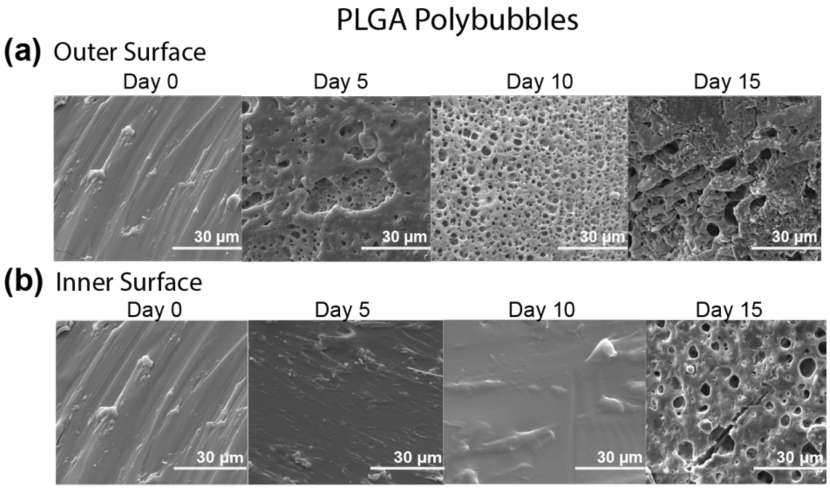

Figure S4. (a) Outer surface of cut PLGA polybubbles with gradually increasing pore size observed for 15 days. (b) Inner surface of cut PLGA polybubbles with increasing pore size observed on day 15 in contrast to pore size increase observed in (a). Reprinted with permission from John Wiley and Sons from Arun Kumar *et al.* [140]

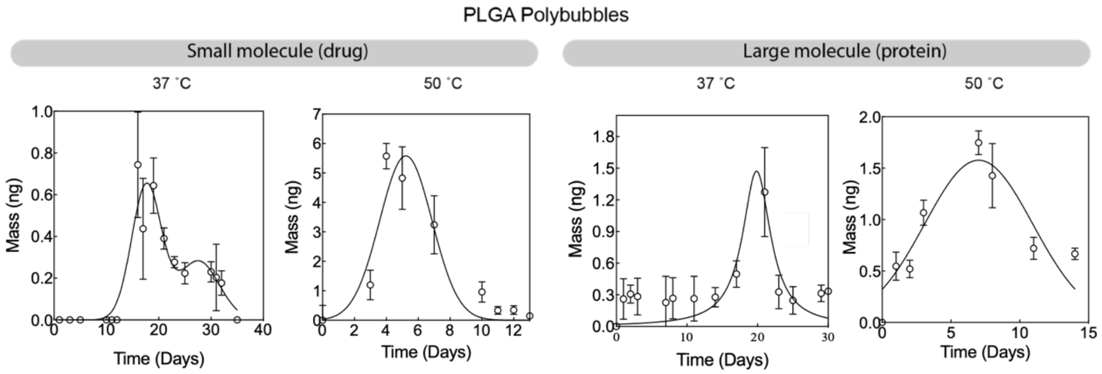

Figure S5. Non-cumulative release profiles of PLGA polybubbles showing delayed burst release of cargo (small molecule and large molecule) at physiological conditions (37 °C) and accelerated conditions (50 °C).

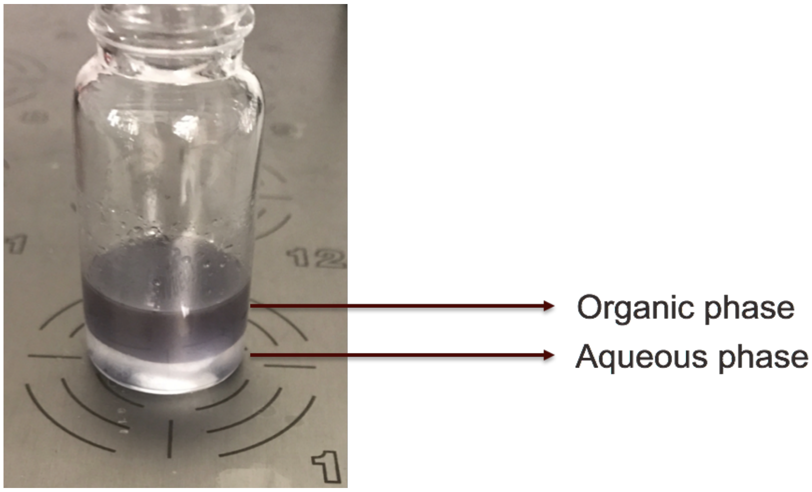

Figure S6. Hydrophobicization of AuNRs enabled phase transfer of CTAB-stabilized AuNRs from aqueous phase (water) to organic phase (toluene). Reprinted with permission from John Wiley and Sons from Arun Kumar *et al.* [140]

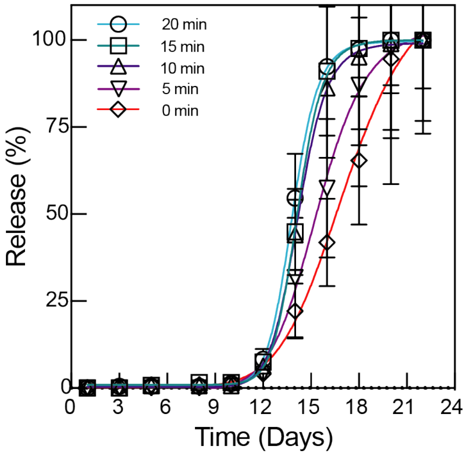

Figure S7. Differential delayed burst release profiles of acriflavine from PLGA polybubbles that were activated for 0, 5, 10, 15, and 20 minutes

APPENDIX C

SUPPORTING INFORMATION FOR CHAPTER 5

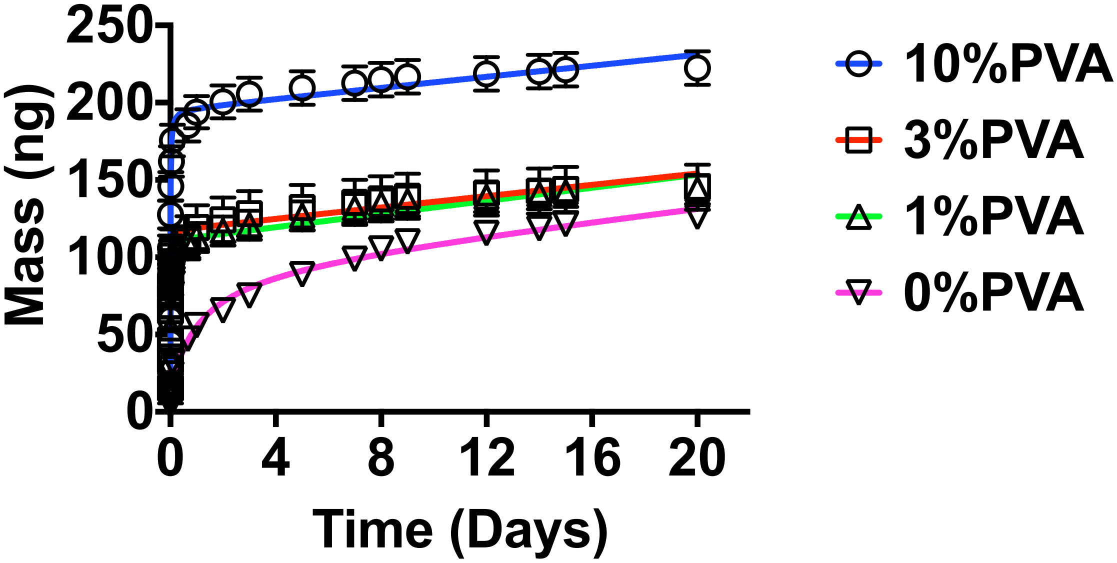

Figure S1. Cumulative release curves indicate that acriflavine release from HDI shape memory foams increased with increasing PVA concentration.

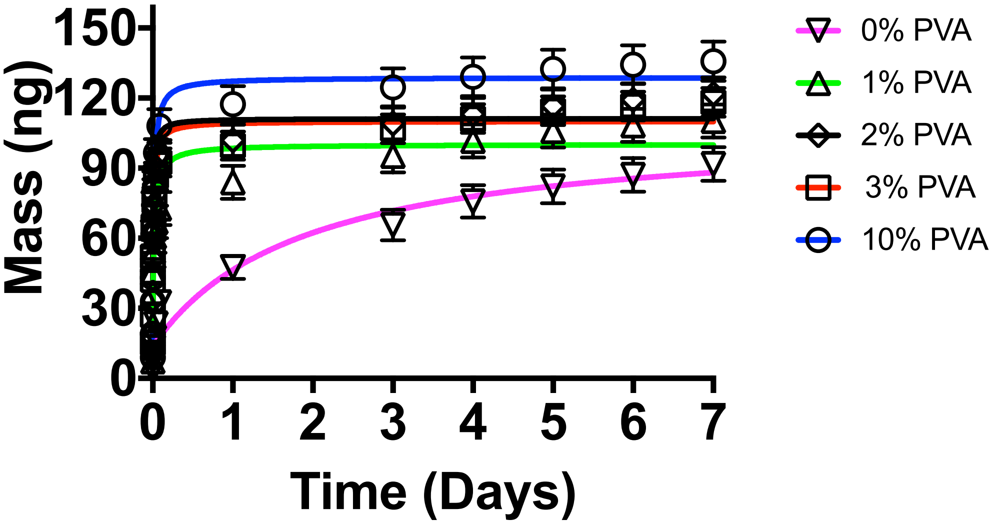

Figure S2. Cumulative release curves indicate that acriflavine release from reticulated HDI shape memory foams increased with increasing PVA concentration.

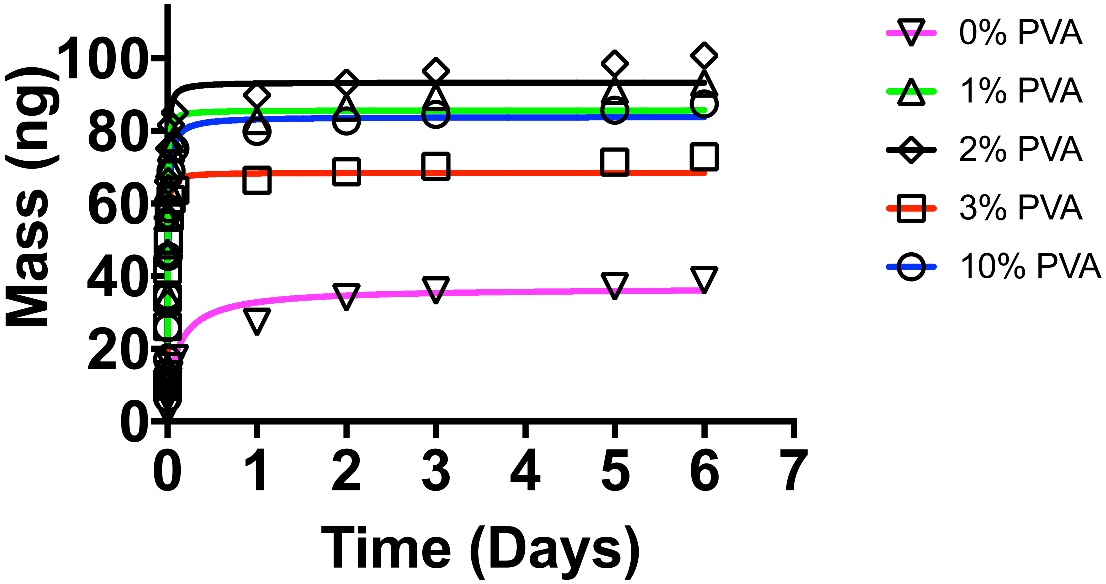

Figure S3. Cumulative release curves indicate that acriflavine release from reticulated TMHDI shape memory foams increased with increasing PVA concentration.